공학박사학위논문

# Fluid-Structure Interaction Analysis of Anisotropic Cambered Wing of Flapping-Wing Micro Air Vehicles

## 날갯짓 초소형 비행체의 비등방성 캠버날개에 대한 유체-구조 연성해석 연구

2023 년 2 월


서울대학교 대학원

기계항공공학부

윤 상 훈

# Fluid-Structure Interaction Analysis of Anisotropic Cambered Wing of Flapping-Wing Micro Air Vehicles

## 날갯짓 초소형 비행체의 비등방성 캠버날개에 대한 유체-구조 연성해석 연구

지도교수 김 종 암

이 논문을 공학박사 학위논문으로 제출함

**2022년 11월**

서울대학교 대학원

기계항공공학부

윤 상 훈

윤상훈의 공학박사 학위논문을 인준함

**2022년 12월**

**위 원 장** ________________________

**부위원장** ________________________

**위 원** ________________________

**위 원** ________________________

**위 원** ________________________

# Abstract

Flapping-wing micro air vehicle (FW-MAV) mimics birds or insects and has received considerable attention due to its agility and hovering abilities, making it an ideal micro unmanned aerial vehicle for the next generation.

Flight and aerodynamic performance of FW-MAVs is largely determined by their flexible wings. Hence, the purpose of this study is to develop a fluid-structure interaction analysis framework that can accurately analyze anisotropic flexible wings composed of various materials and complex shapes by simulating them realistically. In addition, a strategy for designing flexible wings to improve the aerodynamic performance of flapping aircraft is presented based on the analysis of various aeroelastic design parameters.

An analysis program for fluid-structure interaction of cambered wings is developed that can simulate the fluid and structural characteristics of cambered wings realistically. FW-MAV's cambered wing is composed of thick veins and thin membranes of different materials, which are installed in a form with a camber angle to maximize flexibility. As the wing shows large deformations and displacements, numerical methods that are capable of accurately simulating fluid-structure phenomena are applied. As part of the development process, flow analysis, structural analysis, coupling analysis, data transmission module, and the final integrated module are compared and validated to ensure accuracy and efficiency. Cross-validation is also carried out against experimental results obtained in the present study to ensure an accurate analysis of cambered wings of FW-MAV (thrust, experimental error: about 1%). The solver can therefore be used to analyze a broad range of flexible wings including flapping vehicles, due to its ability to realistically reflect fluid, structural, and physical properties.

A fluid-structure interaction analysis of the camber wing's passive trajectory and its unsteady aerodynamic mechanism is presented, along with aeroelastic trajectory characteristics promoting thrust generation. To determine the thrust and propulsive efficiency of the aircraft, aeroelastic design parameters are analyzed (camber angle, operating frequency, material properties of veins, pivot distance) as well as the relationship between structural dynamics (natural frequencies, mode functions) and unsteady flow characteristics. Design guidelines for anisotropic flexible wings are presented, which are advantageous for generating thrust and efficiency. The aerodynamic performance of the wing designed for hovering flight was significantly improved by applying the parameter selection direction suggested in this study. As a result of this study, the results of greatly improved aerodynamic performance were also confirmed in forward flight conditions. The proposed design direction should lead to excellent aerodynamic performance under various operating conditions in the future.

An approach to enhancing the performance of flexible wings is presented in this study by extending experimental or empirical flapping flight vehicle research into numerical analysis. It can be used to develop flapping aircraft with improved performance by analyzing fluid-structural phenomena for various aeroelastic design parameters.

**Keywords**: Fluid–structure interaction (FSI), Aeroelastic, Computational fluid dynamics (CFD), Flapping-wing micro air vehicles (FW-MAV), Insect-like, Biomimetics, Cambered wing

**Student Number**: 2014-21890

# Contents

# List of Figures

# List of Tables

# Chapter 1

# Introduction

## 1.1 Research Background

There are nearly a million different species of flapping insects, and 10,000 species of flapping birds and bats. The flight mechanism of insects has captured the attention of scientists and engineers in numerous scientific fields, including biology, ecology, morphology, engineering, and so on. The efficient flight mechanism of living things has attracted scientists and engineers because flapping flight has the potential for generating higher efficiency in a smaller size than rotor flight (Fig. 1.1). Particularly, insects' flapping flight has been considered a fascinating research topic in the field of unsteady aeronautics because of its potential application to propulsive devices or next-generation flying vehicles [15].

Flapping-wing micro air vehicles (FW-MAVs) typically have dimensions around 15 cm, mimicking the flight mechanisms of birds or insects. Due to their efficient and maneuverable bio-inspired flight mechanisms, FW-MAVs can improve remote sensing and information gathering capabilities for both military

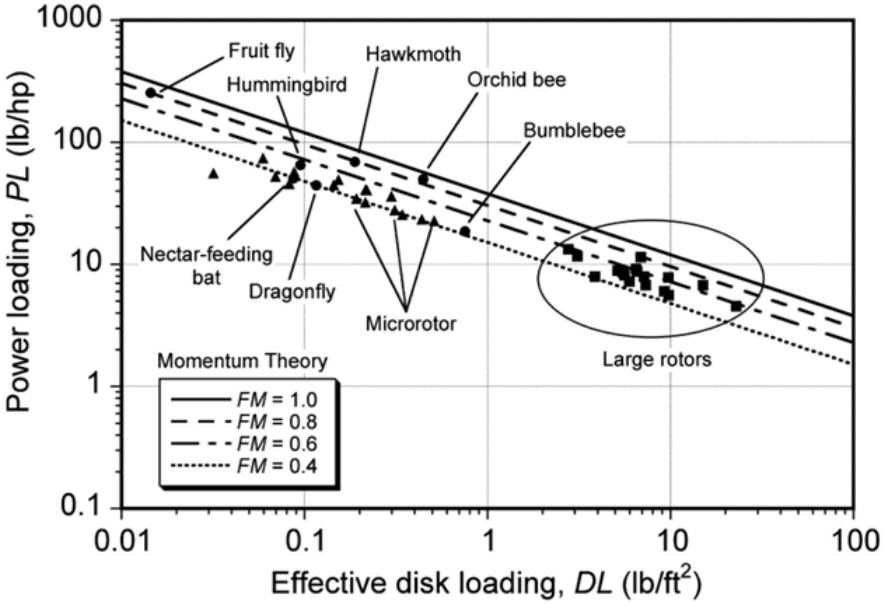


Figure 1.1: Power loading versus effective disk loading for biological andmechanical systems [1].

and civilian applications [16]. As the FW-MAV has a very small battery capacity, the issue of flight endurance has emerged recently. By analyzing birds or insects' flight mechanisms, various studies have been conducted to derive an ideal flight efficiency that is equivalent or more efficient than that of living things. It appears that FW-MAV can be made more efficient through research based on unsteady aerodynamic characteristics and structural characteristics, which could lead to an approach to FM=1 (Fig. 1.1). For this reason, various experimental and computational analyses have been conducted to investigate unconventional and unsteady aerodynamic characteristics.

Experimental studies have been conducted on insect wing motions. A leading-edge vortex (LEV) was observed by Ellington et al. [17] using smoke visualization around a 3-D model and a real moth at the Reynolds number of O(103). While downstroke motion was occurring, they observed a strong vortex attached to the leading-edge. Dickinson et al. [18] studied unsteady aerodynamic forces in oil tanks, focusing on the visualization of flow patterns according to dynamically scaled mechanical models. According to their findings, 'rotational circulation' and 'wake capture' are the two key mechanisms enhancing lift. Nagai and Isogai [19] used dynamically scaled mechanical models in a water tunnel to measure time-varying aerodynamic forces applied to flapping wings in hovering and forward flight, and examined how the aerodynamic characteristics of a flapping insect's wing were influenced by its wing kinematics. It is useful to use experimental studies to understand global flow phenomena, but it has difficulty describing the detailed flow field.

Several researchers have therefore conducted computational research in order to analyze physical phenomena in detail. Based on three-dimensional computations, Liu and Kawachi [20] confirmed the LEV of a moth (Manduca sexta) wing under hovering flight. An insect clap-fling motion was numerically simulated by Sun and Yu [21] using a Navier-Stokes solver and a considerable amount of lift could be generated. Hence, these key unsteady aerodynamic mechanisms can be numerically analyzed, and these mechanisms can be used to study aerodynamic phenomena of various living organisms. To understand three-dimensional flow fields, Ramamurti [22] computed a three-dimensional study of a flapping fruit fly wing. Based on the understanding of the role of leading-edge and trailing-edge vortices, Lee et al. [23] developed an optimal flapping airfoil that can maintain both a high propulsive efficiency and thrust coefficient. Additionally, they examined a two-dimensional vortical flow field to explain an insect's forward flight's impulsive thrust generation mechanism [24]. Kim et al. [25] simulated a blowfly's forward flight three-dimensionally and

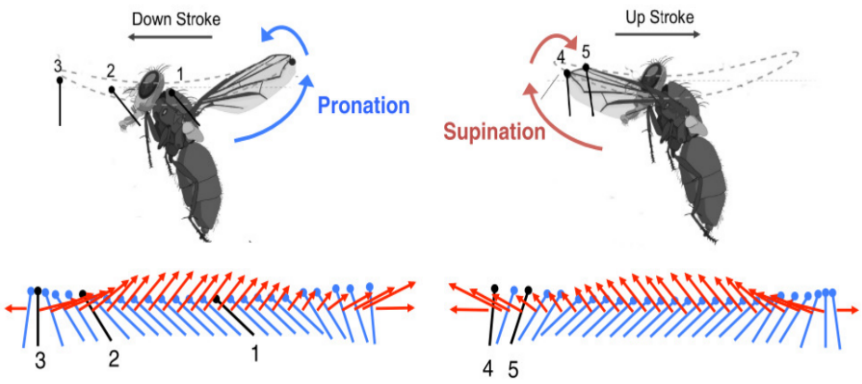


Figure 1.2: A flying creature's wing trajectory - pronation and supination [2].

identified the role of three-dimensional vortices in unsteady aerodynamics. A dragonfly's flapping wing in forward flight was numerically simulated by Wang and Sun [21], and unsteady aerodynamic characteristics and forewing-hindwing interactions were analysed. The study of planform and camber effects on the unsteady aerodynamics of three-dimensional wings at various angles of attack and low Reynolds numbers was conducted by Swanson and Isaac [26]. Bomphrey et al. [27] examine leading-edge vortices and trailing edge vortices produced by mosquito free-flight, studying rapid changes in pitch angle (wing rotations) at the end of each half-stroke using Navier-Stokes solvers. In this way, the flow fields around the wings of a variety of insects have been numerically investigated to understand their aerodynamic characteristics and vortex structures. As a result of camber-induced or muscle-induced flapping, the insect's wings perform pronation or supination according to its circumstances (Fig.1.2). The timing of the wing's rotation makes it very important to precisely analyze these trajectories since they contribute to unsteady aerodynamic mechanisms (Fig. 1.3, 1.4). It is also noteworthy that biological flyers have highly flexible wings, which tend to deform significantly during flapping flight. Due to the fact that

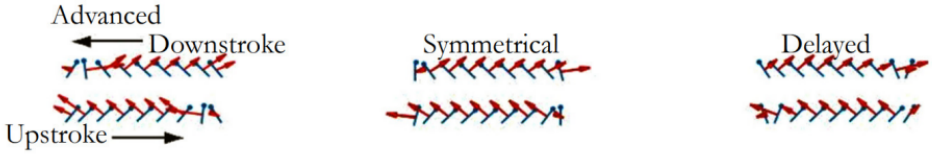


Figure 1.3: insects rotational mechanism [3].

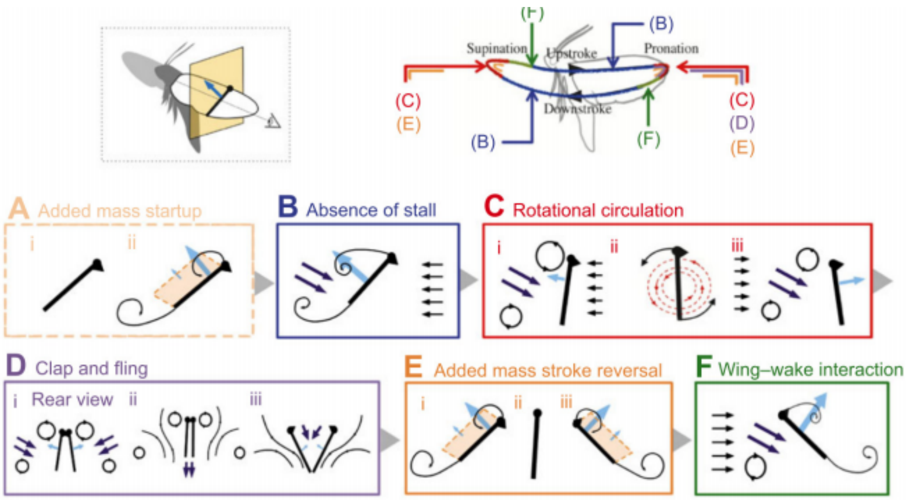


Figure 1.4: insect's unsteady aerodynamic flapping mechanism [4].

these trajectories are designed to generate aerodynamic force, studies have been conducted to determine what effects structural flexibility has on the generation of these trajectories. Heathcote and Gursul conducted experimental studies on flexible flapping airfoils [28]. They measured thrust and propellant efficiency around chordwise flexible 2-D airfoils oscillating in heave at low Reynolds numbers. By observing the optimal thickness of the airfoil and plunging frequency, the researchers observed maximum thrust and propulsive efficiency. Aside from experimental works, computational studies have been conducted on flexible flapping airfoils. According to Pederzani and Haj-Hariri [29], chordwise flexibility affects heaving airfoils by means of a FSI numerical model for 2-D unsteady viscous flows around a flexible airfoil. According to their findings, the flexible airfoil proved more efficient at different plunging frequencies as a result of altering the flow fields. An elastic plate behind a bluff body was simulated through a vortex-excited elastic plate by Olivier et al. [30], and preliminary results were presented about flexible flapping wings. Lee et al. [31] confirmed that the aerodynamic performance of insect wings was improved through the two-dimensional FSI analysis. A two-dimensional FMAV model and FSI analysis were also performed by Jeong [11]. Using numerical simulation, Shyy et al. [32] investigated the flow field around a flexible plunging airfoil in incoming flow and observed dynamic fluid characteristics as well as thrust generation mechanisms. It was possible to study the effect of flexibility on airfoils by coupling a finite element structural solver with a fluid solver based on the Navier-Stokes equations. A FSI simulation of a FW-MAV wing was used by Tay et al. [33] in order to investigate the effects of spanwise and chordwise flexibility on aerodynamic performance. Also, it was observed that flexibility-induced wing rotation and bending motion can enhance aerodynamic force using FSI analysis by Kang et al. [34]. As above, previous studies conducted on single-material wings have yielded meaningful results.

However, actual living organisms have veins and thin membranes of different materials on their wings (Figs. 1.5, 1.6). There is a very large difference between the trajectory of anisotropic wings and the trajectory of isotropic wings. As a result, isotropic modeling could not accurately simulate the trajectory of a flexible wing composed of veins and membranes with different material properties.

An anisotropic wing structure made up of a variety of materials was studied in order to apply its characteristics. Nakata et al. [35] observed that wing flexibility improves aerodynamic performance in insects using shell element-based

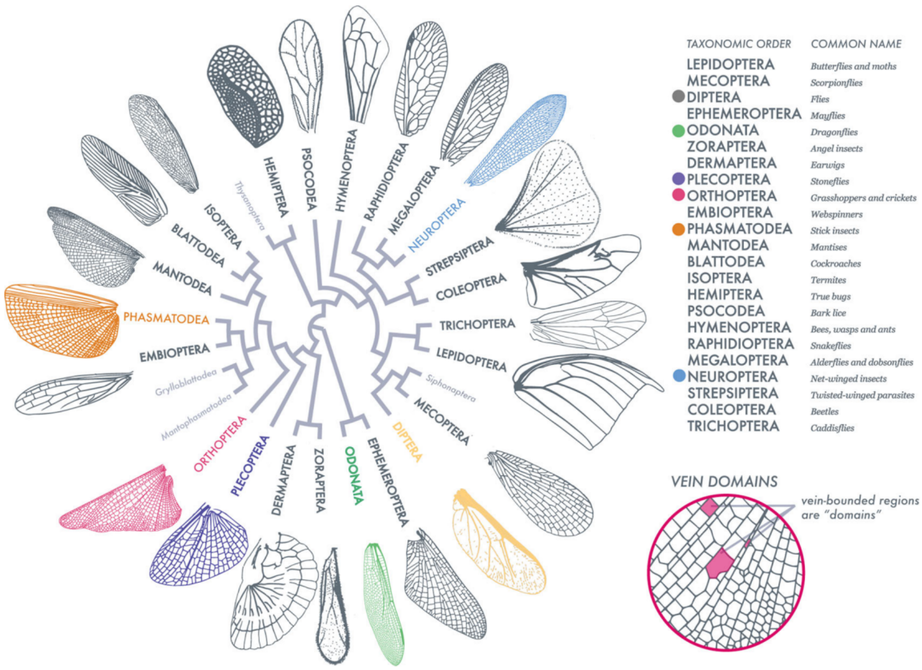


Figure 1.5: Various configuration of vein of the insect wing [5].

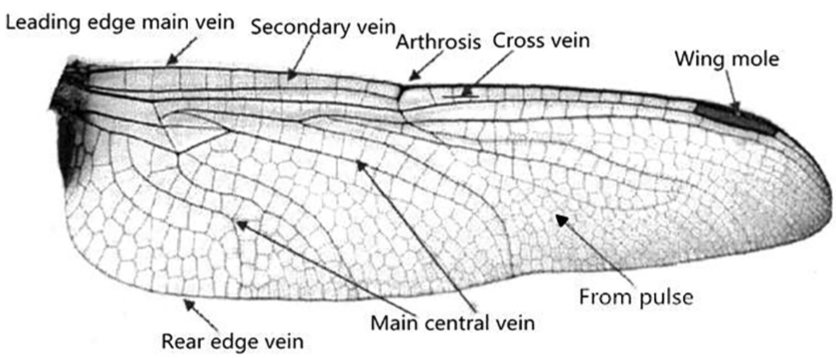


Figure 1.6: Dragonfly wing structure [6].

anisotropic modeling. As well, Nguyen and Han [36] studied the effect of wing flexibility on flight stability by applying aeroelastic analysis to the anisotropic wings of the insect mimicking FMAV. According to Wu et al. [7] an experiment was conducted to determine the relationship between multi-component flapping wing structures and the production of aerodynamic force (Fig. 1.7). In a multi-component Zimmerman wing, they observed variations in thrust based on vein thickness. Meanwhile, researchers have developed FSI solvers to analyze wings made of various materials using detailed structure modeling, such as veins and membranes. A structural solver developed by Cho et al. [37, 38] can efficiently simulate detailed wing configurations with beam and shell elements in a co-rotational (CR) frame. It was demonstrated that precise analysis is possible by combining anisotropic modeling with fluid analysis for the Zimmerman wing [13, 39, 40, 41].

The understanding of flexible wings composed of veins and membranes has progressed significantly in recent years. The FW-MAV's wings, however, contain additional complex components, such as wing camber (Fig. 1.8). A cambered wing imitating an insect's wing has been adopted to maximize the rotation effect (Fig.1.9). In a cambered wing, the camber angle (also known as slack angle or wing margin) is applied so that the wing is twisted around the rotation axis. It is composed of different materials for the leading-edge vein, the central vein, and the membrane. As well, the membrane rotates freely at the leading-edge and axis of rotation of the wing, and the central vein is strongly attached to it.

## 1.2 Research Strategy

Cambered wings are used in many FW-MAVs as an efficient driving mechanism because they can implement insect-like flapping trajectories without an addi-

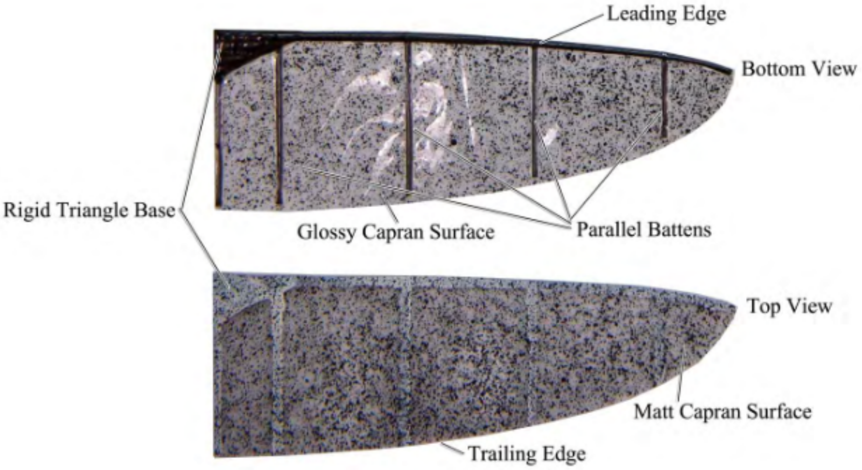


Figure 1.7: Zimmerman wing - batten parallel reinforced wing [7].

tional driving unit. Because existing FSI studies have limitations in accurately modeling cambered wings, the development of FW-MAVs with cambered wings has relied on experimental methods or simple aerodynamic theories to determine the ideal camber angle [48, 49, 50, 47, 14, 51]. A particularly critical issue is the flight time of the FW-MAV, because of its small size and limited battery capacity. Hence, the aerodynamic performance of the cambered wing must be improved. As the effects caused by flexible cambered wings are essentially aeroelastic phenomena, it is necessary to conduct detailed computational investigations with a robust and accurate FSI solver to understand the unsteady aerodynamic mechanism and the associated vortex structure around anisotropic cambered wings with realistic modeling [52].

For the purpose of analyzing the FW-MAV's cambered wing [53, 54, 55, 14, 51], an FSI solver is developed that simulates realistic wing geometry with details of anisotropic structural components. FW-MAV wings are modeled using numerical methods that accurately represent fluid and structural characteristics such as complex shapes and anisotropic materials, and the present FSI solver

(a) Nano hummingbird [42].

(b) DelFly [43].

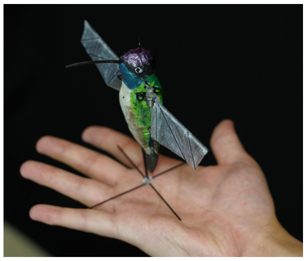

(c) Purdue hummingbird [44].

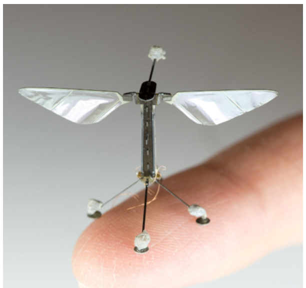

(d) Robobee [43].

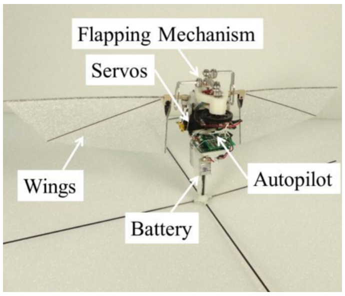



(e) Robotic hummingbird [45].

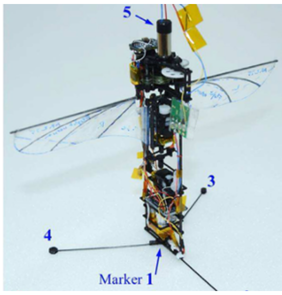



(f) KUBeetle [46].

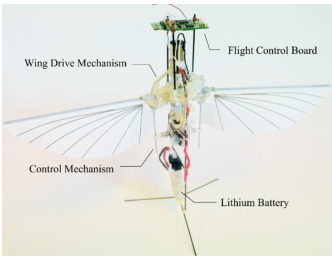



(g) Colibri robot [47].

Figure 1.8: Previously reported bioinspired FW-MAVs.

Figure 1.9: Cambered wing shape.

is validated with experiments and numerical analysis of previous studies. In order to cross-validate the FSI analysis of the FW-MAV flexible cambered wings, which feature complex geometry and structures, an experiment is conducted. Following that, a detailed investigation is carried out of the unsteady vortex structures around the wings to better understand their aerodynamic performance. Finally, the design parameters that affect the aerodynamic performance of the FW-MAV are analyzed within the operating frequencies of the flapping vehicle. For the purpose of presenting a design for parameters that improve thrust and propulsive efficiency, a flow field analysis based on an aeroelastic trajectory is performed. This is followed by structural dynamic characteristics analysis to analyze patterns that are conducive to aerodynamic performance.

## 1.3 Outline of Thesis

The present thesis is organized as follows. Chapter 2 deals with the numerical methodology that can accurately analyze the anisotropic cambered wing with realistic modeling. Methodologies and governing equations of fluid-structure coupling analysis are organized, and techniques that can be analyzed precisely and efficiently are introduced for each analysis module.

Chapter 3 deals with the validation of the present fluid-structure interaction analysis program. Each analysis module is validated, and validation with previous studies on anisotropic flexible wings is performed.

Chapter 4 deals with the two-dimensional fluid-structure interaction analysis of the FW-MAV's wing. The two-dimensional modeling technique and the effect of passive rotation of wings on aerodynamic performance are analyzed.

Chapter 5 deals with the three-dimensional fluid-structure interaction analysis of the FW-MAV's cambered wing. Cross-validation between experimental and numerical analysis is used to evaluate the three-dimensional accuracy of the anisotropic cambered wing. Additionally, key aeroelastic design parameters of the cambered wing are analyzed, along with unsteady vortex structures, aeroelastic trajectory and structural dynamic characteristics. Consequently, a direction for designing parameters for improved aerodynamic performance is suggested, and the result of an improved wing is demonstrated.

Chapter 6 summarizes this study.

# Chapter 2

# Numerical Approach

## 2.1 Fluid Solver

An in-house flow analysis program that can be applied selectively in 2-D and 3-D is developed. By extending the 2-D flow analysis solver developed with Jeong [11], the 3-D flow analysis solver is developed.

### 2.1.1 Governing Equations

The unsteady three-dimensional Navier-Stokes equations are employed as the governing equations for the fluid solver. The arbitrary Lagrangian-Eulerian equations of mass and momentum conservation are used to describe an arbitrarily moving and deforming control volume $V(t)$ with a boundary $S(t)$ [56].

$$\frac{d}{dt}\int_{V(t)} \rho dV + \int_{S(t)} \rho\left(\mathbf{V} - \dot{\mathbf{x}}\right)\cdot \mathbf{n} dS = 0, \tag{2.1}$$

$$\frac{d}{dt}\int_{V(t)} \rho \mathbf{V} dV + \int_{S(t)} \rho \mathbf{V}\left(\mathbf{V} - \dot{\mathbf{x}}\right)\cdot \mathbf{n} dS = \int_{S(t)} \sigma \cdot \mathbf{n} dS, \tag{2.2}$$

where $\rho$ is the flow density, $\mathbf{V}$ is the flow velocity, and $\mathbf{x}$ is the boundary position. Using $\mathbf{n}$ as the face normal velocity is calculated so that it satisfies the geometric conservation law (GCL) [57] . By satisfying the momentum equation, the time-accurate artificial compressibility method [58] is employed to iteratively update the velocity and pressure fields.

An arbitrary Lagrangian-Eulerian (ALE) description describes a situation between two extreme cases, such as that of an arbitrarily moving and deforming control volume with $\boldsymbol{V} = \dot{x}$ and $\dot{x} = 0$. The normal vector of the control volume is $\boldsymbol{n}$. Using the Arbitrary Lagrangian-Eulerian formulation, the nondimensionalized incompressible Navier-Stokes equations read as follows:

$$\frac{d}{dt}\int_{V(t)} \mathbf{Q}dV + \int_{S(t)} \left(\boldsymbol{E}_I\hat{i} + \boldsymbol{F}_I\hat{j} + \boldsymbol{G}_I\hat{k}\right)\cdot\mathbf{n}dS = \int_{S(t)} \left(\boldsymbol{E}_V\hat{i} + \boldsymbol{F}_V\hat{j} + \boldsymbol{G}_V\hat{k}\right)\cdot\mathbf{n}dS \tag{2.3}$$

where $\mathbf{Q}$ is a vector of conservative variables, $\boldsymbol{E}_I\hat{i} + \boldsymbol{F}_I\hat{j} + \boldsymbol{G}_I\hat{k}$ are inviscid fluxes, and $\boldsymbol{E}_V\hat{i} + \boldsymbol{F}_V\hat{j} + \boldsymbol{G}_V\hat{k}$ are viscous fluxes. The equation 2.3 can be rewritten as follows:

$$\mathbf{P}\frac{d}{d\tau}\int_{V(t)} \mathbf{Q}_P dV = -\frac{d(\mathbf{Q}V)}{dt} - \boldsymbol{\mathcal{R}}\left(\mathbf{Q}_P, \mathbf{x}, \dot{\mathbf{x}}\right), \tag{2.4}$$

where $\mathbf{x}$ and $\dot{\mathbf{x}}$ are time-varying position and velocity vectors of the mesh points. In the system of equations, $\mathbf{Q}_P$ represents the primitive variables and $\boldsymbol{\mathcal{R}}\left(\mathbf{Q}_P, \mathbf{x}, \dot{\mathbf{x}}\right)$ represents the residual:

$$\boldsymbol{\mathcal{R}}\left(\mathbf{Q}_P, \mathbf{x}, \dot{\mathbf{x}}\right) = \int_{S(t)} \left(\boldsymbol{E}_I\hat{i} + \boldsymbol{F}_I\hat{j} + \boldsymbol{G}_I\hat{k}\right)\cdot\mathbf{n}dS - \int_{S(t)} \left(\boldsymbol{E}_V\hat{i} + \boldsymbol{F}_V\hat{j} + \boldsymbol{G}_V\hat{k}\right)\cdot\mathbf{n}dS \tag{2.5}$$

The control volume-averaged variables are defined as follows:

$$\bar{\mathbf{Q}} = \frac{1}{V(t)}\int_{V(t)} \mathbf{Q}dV \tag{2.6}$$

The equation 2.6 can be rewritten as follows:

$$\frac{d(\bar{\mathbf{Q}}V)}{dt} + \boldsymbol{\mathcal{R}}\left(\bar{\mathbf{Q}}_P, \mathbf{x}, \dot{\mathbf{x}}\right) = 0, \tag{2.7}$$

The bar will be dropped for the remainder of the chapter.

### 2.1.2 Time-Accurate Artificial Compressibility Methods

A time-accurate artificial compressibility method is used to solve incompressible Navier-Stokes equations [58, 59]. In the continuity equation, a pseudo-time derivative of pressure is added, while in the momentum equation, a pseudo-time derivative of velocity is added. As a result, the system of conservation laws with a pseudo-term can be expressed as follows:

$$\mathbf{P}\frac{d}{d\tau}\int_{V(t)}\mathbf{Q}_P dV = -\frac{d(\mathbf{Q}V)}{dt} - \boldsymbol{\mathcal{R}}\left(\mathbf{Q}_P, \mathbf{x}, \dot{\mathbf{x}}\right), \tag{2.8}$$

Pseudo-time is $\tau$ and a diagonal matrix P includes an artificial compressibility parameter $\beta$, which acts as a preconditioner for continuous equations.

$$\mathbf{P} = \begin{bmatrix} 1/\beta & 0 & 0 & 0 \\ 0 & 1 & 0 & 0 \\ 0 & 0 & 1 & 0 \\ 0 & 0 & 0 & 1 \end{bmatrix} \tag{2.9}$$

Using the 2$^{\text{nd}}$-order backward difference formulation, the unsteady source term is discretized as follows:

$$\mathbf{S}^{n+1} = \frac{d(\mathbf{Q}V)}{dt} = \frac{3(\mathbf{Q}V)^{n+1} - 4(\mathbf{Q}V)^{n+1} + (\mathbf{Q}V)^{n+1}}{2\Delta t}, \tag{2.10}$$

Pseudo-time is $\tau$, and real-time is $t$, with $V(t)$ representing a moving control volume. A pseudo-time derivative can also be inserted inside a volume integral. In this case, the equation is as follows:

$$\frac{d{\mathbf{Q}_P}^{n+1}}{d\tau} = -\mathbf{P}^{-1}({\mathbf{S}_P}^{n+1} - {\boldsymbol{\mathcal{R}}_P}^{n+1}) = -({\mathbf{S}_P}^{n+1,k} - {\boldsymbol{\mathcal{R}}_P}^{n+1,k}), \tag{2.11}$$

In pseudo-time, the index $k$ represents the number of iterations. Dual-time stepping is required for time advancement, which involves solving a steady-state problem in pseudo-time for each step in real time.

### 2.1.3 Spatial Discretization

Incompressible Navier-Stokes equations are solved using the finite-volume method. Taking one particular cell, the residual can be expressed as follows:

$$\begin{aligned}\mathbf{R}_{P_{I,J,K}} &= \mathbf{P}^{-1}\left[\int_{S_{I,J}}(\mathbf{E}_I\hat{\imath}+\mathbf{F}_I\hat{\jmath}+\mathbf{G}_I\hat{k})\cdot\boldsymbol{n}dS - \int_{S_{I,J}}(\mathbf{E}_V\hat{\imath}+\mathbf{F}_V\hat{\jmath}+\mathbf{G}_V\hat{k})\cdot\boldsymbol{n}dS\right] \\ &= \sum_{m=1}^{N_F}\mathcal{F}_{I_m}\Delta S_m - \sum_{m=1}^{N_F}\mathcal{F}_{V_m}\Delta S_m,\end{aligned} \tag{2.12}$$

$\mathcal{F}_{I_m}$ is the inviscid flux and $\mathcal{F}_{V_m}$ is the viscous flux for face $m$.

#### Differencing of Inviscid Flux

Based on the numerical flux of inviscid flux,

$$\mathcal{F}_{I_m} = \frac{1}{2}(\mathcal{F}_{I_L}+\mathcal{F}_{I_R}) - \mathcal{D}_m \tag{2.13}$$

$\mathcal{D}_m$ is the numerical dissipation. A numerical dissipation model can be used for central differentiation or upwind differentiation for spatial differentiation. A dissipation model with discontinuities may approach first order accuracy, but a model with incompressible flows, where there is no discontinuity, should have higher accuracy than first order. Inviscid fluxes are upwind-differencing using Roe's approximate Riemann solver for flux-differencing [60].

### Caculation of Face Normal Velocity

Normal grid velocity $\dot{n}$ is calculated to satisfy both design temporal accuracy and Geometric Conservation Law (GCL). [57]. When using a backward difference formulation with $2^{\text{nd}}$ order, grid coordinates and face-averaged normal velocities need to be evaluated at $n+1$. At this time, the normal grid velocity is calculated as follows:

$$\dot{n}_m^{n+1} = \frac{1}{\Delta t}(-\frac{1}{2}\Delta V_m^1 + \frac{3}{2}\Delta V_m^2), \tag{2.14}$$

### Higher Order Spatial accuracy

Higher-order spatial accuracy is achieved using $3^{\text{rd}}$-order linear variable reconstruction. Monotone Upsteam-centered Schemes for Conservation Laws (MUSCL) [61] interpolation is adopted as follows:

$$\begin{aligned} q_{i+1/2}^{-} &= q_i + \frac{1}{4}[(1-\kappa)(q_i - q_{i-1}) + (1+\kappa)(q_{i+1} - q_i)], \\ q_{i+1/2}^{+} &= q_i - \frac{1}{4}[(1+\kappa)(q_{i+2} - qi) + (1-\kappa)(q_{i+2} - qi + 1)], \end{aligned} \tag{2.15}$$

Where $q$ represents the primitive variables. With constant $k = 1/3$, the spatial accuracy is $3^{\text{rd}}$ order, and for $k = -1, 0, 1$, it is $2^{\text{nd}}$ order. For $k = 1$, it becomes a central-difference scheme of $2^{\text{nd}}$ order.

### Differencing of Viscous Flux

The viscous flux terms are centrally differenced by a $2^{\text{nd}}$-order spatial accuracy.

### 2.1.4 Time Integration

Implicit time integration can be used to solve pseudo-time equations. Pseudo-time derivatives are computed with the $1^{\text{st}}$-order implicit Euler formula for better convergence characteristics:

$$V^{n+1}\frac{\mathbf{Q}_P{}^{n+1,\ k+1}-\mathbf{Q}_P{}^{n+1,\ k}}{\Delta\tau}=-\mathbf{S}_P{}^{n+1,\ k+1}-\boldsymbol{\mathcal{R}}_P{}^{n+1,\ k+1}, \tag{2.16}$$

Where $k$ denotes the pseudo-time iteration level. In accordance with the physical time integration method, the dual time stepping method adopted here has a time accuracy of $2^{\text{nd}}$-order. A Taylor series expansion is then used to discretize the final governing equations as follows [62]:

$$\left[\frac{V^{n+1}}{\Delta\tau}+\left(\frac{\partial\boldsymbol{\mathcal{R}}_P}{\partial\mathbf{Q}_P}+\frac{\partial\mathbf{S}_P}{\partial\mathbf{Q}_P}\right)^{n+1,\ k}\right]\boldsymbol{\Delta}\mathbf{Q}_P{}^{n+1,\ k}=-\mathbf{S}_P{}^{n+1,\ k}-\boldsymbol{\mathcal{R}}_P{}^{n+1,\ k}. \tag{2.17}$$

With the dual time stepping method, the lower/upper symmetric Gauss-Seidel scheme is used for time integration [63]. At each physical time step, a steady state solution is obtained by a residual lower than $\mathcal{O}(10^{-4})$. The far boundary condition for the inflow and outflow regions is derived from the method of characteristics and is explicitly derived. The far boundary rotates with the movement of the wall boundary in large-deforming grids or large flapping angles. The computational flow field is assumed to be laminar because, for the Reynolds number of current interest ($Re$=$\mathcal{O}(10^3\sim10^4)$), computations with the laminar flow assumption are known to agree well with experiments [64]. Parallel computing techniques have been implemented using message-passing interfaces.

## 2.2 Structural Solver

The development of the structural analysis solver was carried out by Prof. Shin and Prof. Cho. [65, 66, 8]. Nonlinear finite elements based on the CR formulation are adopted to consider the wing configurations in a precise manner. The CR beam is employed for the veins and the CR shell elements for the wing membrane. Globalized Lagrange multipliers are then employed to interconnect the finite elements.

### 2.2.1 Elemental Kinematics and Unified CR Formulation

A CR formulation is determined by tracking an elemental motion based on coordinates. An element's coordinates include its fixed, undeformed, CR, and deformed coordinates. Between an undeformed and a deformed frame there is an intermediate configuration known as the CR coordinate [67].

Adapting this concept to rigid body motion, this study considers the motion of moving structures with rigid bodies. As a result, an additional coordinate is created in the inertial frame. This extension requires the simultaneous prescription of motion and the application of the governing equations. Local and global quantities are denoted by the subscripts $L$ and $G$, respectively. By using global rotation, the rotational operator $\mathbf{R}_G$ is defined. This will result in the orientation of the deformed frame being determined by the product $\mathbf{R}_r\mathbf{R}_L$.. In addition, the orientation can be obtained by the product $\mathbf{R}_r\mathbf{R}_L$. Based on the orthogonality of the operators, the local rotational operator falls under the relation, $\mathbf{R}_L = {\mathbf{R}_r}^T\mathbf{R}_G\mathbf{R}_o$. The local rotation is then evaluated using the matrix logarithm of the local operator, $\log\mathbf{R}_L$ . As a result, the offdiagonal components of $\log\mathbf{R}_L$ are expressed in terms of the local rotation. Geometric and rigid body rotations are defined with respect to the elemental reference frame by $\mathbf{R}_o$ and $\mathbf{R}_r$ and $[[[R]]]_r$. By equating the local/global internal load vectors $\mathbf{f}$ and the variation of the nodal displacement vectors $\mathbf{q}$, the virtual energy $\Phi$ can be expressed.

$$\Phi = \delta{\mathbf{q}_G}^T\mathbf{f}_G = \delta{\mathbf{q}_L}^T\mathbf{f}_L = \mathbf{B}\delta{\mathbf{q}_G}^T\mathbf{f}_G, \tag{2.18}$$

The transformation matrix $\mathbf{B}$, regulating the relationship between local and

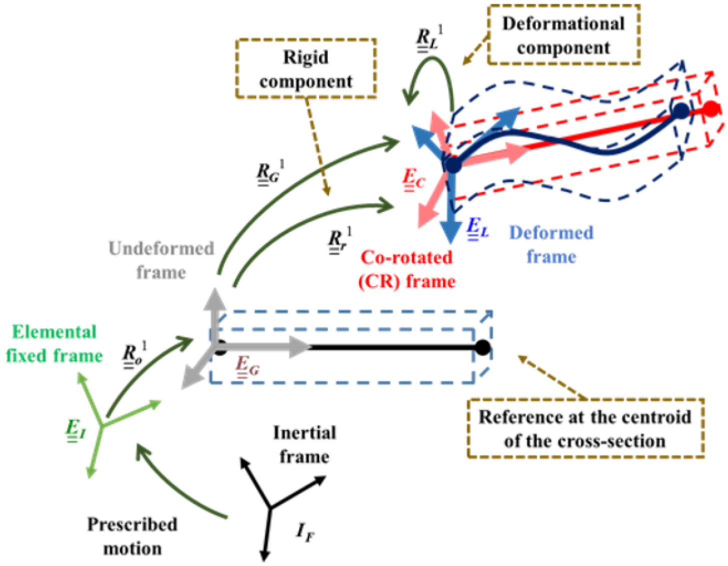


(a) Coordinates for 3D beam element.

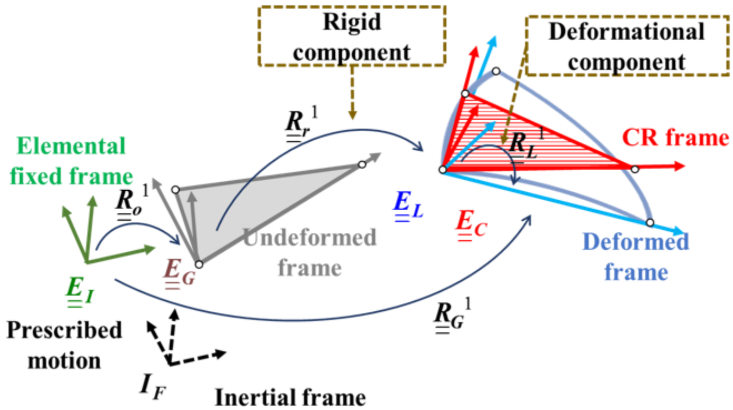


(b) Coordinates for triangular shell element.

Figure 2.1: Coordinates in the CR formulation [8].

global quantities, is derived from the rigid body and deformational components [68]. Internal local load vector $\mathbf{f}_G = \mathbf{B}^T\mathbf{f}_L$. is calculated by equating the local and global internal load vectors. As a result, the global tangent stiffness matrix is defined as a function of $\mathbf{f}_G$. The following is the global tangent stiffness matrix:

$$\mathbf{K}_G = \mathbf{B}^T\mathbf{K}_L\mathbf{B} + \frac{\delta\left(\mathbf{B}^T\mathbf{f}_L\right)}{\delta\mathbf{q}_G}. \tag{2.19}$$

From Eq. (2.19), the internal quantities of both beam and shell can be obtained. It is possible that the choice of the relevant local element may affect the accuracy of the beam and shell analyses in this procedure. A local beam element as suggested by Battini et al. [69] and an OPT–DKT facet shell element [70] are employed in this study.

### 2.2.2 Governing Equations for Beam–Shell Assemblage

To solve the resulting nonlinear equation, the generalized $\alpha$ method is applied. The algorithm used to solve the nonlinear equation is a prediction/correction algorithm, similar to those in previous studies [71, 72]. In the corrector step, a linearized equation of motion leads to incremental displacements: $\mathbf{q}_{G,l+1}^{n+1} = \mathbf{q}_{G,l}^{n+1} + \Delta\mathbf{q}$. Here, the superscript $n$ and the subscript $l$ indicate the time step and the sub-iteration, respectively. A globalized Lagrange multiplier method is used to enforce the kinematic constraints between the beam and the shell [73]. This method yields a straightforward formulation, in which the total virtual work of the entire body is obtained by adding the virtual work of individual components. By using the Lagrange multiplier, the kinematic constraints between any two bodies or adjacent nodes can be taken into account. As a result of kinematic constraints, the variational formulation of the total energy for the beam-shell

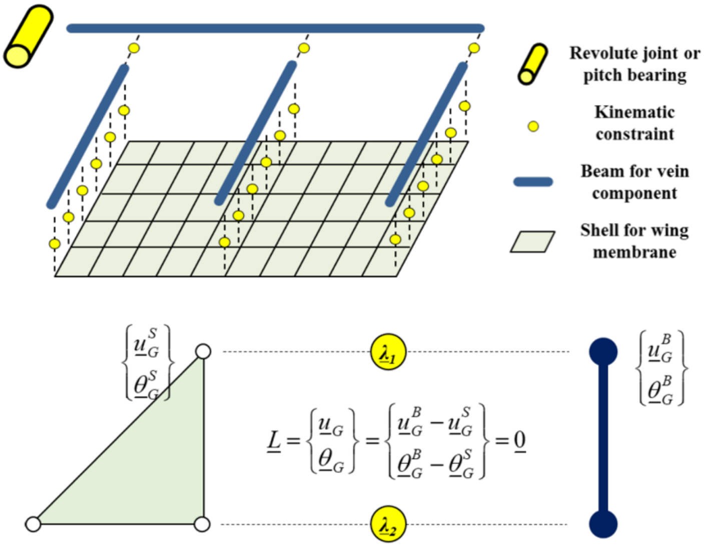


Figure 2.2: Lagrange multiplier with constraints between the beam and shell elements [8].

assemblage can be expressed as follows:

$$\delta\Pi = \delta\Pi_B + \delta\Pi_S + \int \boldsymbol{\lambda}^T \delta\mathbf{L} + \int \delta\boldsymbol{\lambda}^T \mathbf{L} = 0, \tag{2.20}$$

The subscripts $B$ and $S$ indicate quantities related to the beam and shell components, respectively. $\boldsymbol{\lambda}$ represents the Lagrange multiplier for the constraints between the components, and $\mathbf{L}$ is the corresponding constraint equation. The compact form for the governing equations for the beam-shell assemblage can be written as follows starting from the force equilibrium at a given time step:

$$\begin{bmatrix} diag(\boldsymbol{D}_{G,B}, \boldsymbol{D}_{G,S}) & s\boldsymbol{L} \\ s\boldsymbol{L}^T & \underline{\underline{\mathbf{0}}} \end{bmatrix} \begin{Bmatrix} \boldsymbol{\Delta\ddot{q}} \\ \boldsymbol{\Delta\lambda} \end{Bmatrix} = \begin{Bmatrix} \boldsymbol{f}_e - \boldsymbol{f}_k - \boldsymbol{f}_i \\ \mathbf{0} \end{Bmatrix} \tag{2.21}$$

$$\text{with} \quad \mathbf{D}_G = \mathbf{M}_G + c_1\mathbf{C}_G + c_2\mathbf{K}_G,$$

In this case, $c_1$, $c_2$ and $s$ are the coefficients of the generalized-$\alpha$ method and the scaling coefficient, respectively. Mass and gyroscopic matrices referred to the global frame are denoted as $\mathbf{M}_G$ and $\mathbf{C}_G$, respectively. By combining the underlying elemental kinematics of CR with Lagrange's equation of motion, the mass and gyroscopic matrices are derived. Detailed formulation of the mass and gyroscopic matrices can be found in Refs. [8, 37, 38, 40, 66, 74].

## 2.3 FSI Coupling Methodology

### 2.3.1 Coupling Strategy

FSI problems can be solved in several ways. The following two approaches can be considered [9, 75]:

- Monolithic strategy: In this method, fluid and structure equations are discretized and solved simultaneously. It is mathematically reformulated to obtain one combined set of equations and integrated in time. It ensures stability and convergence and is efficient. Due to the size of the system obtained, this approach requires large storage, and it is difficult to invert the Jacobian of a system.

- Partitioned strategy: Fluid and structure governing equations are solved independently using boundary information shared between the solvers. For each discipline, different numerical techniques and time steps can be used, which is appropriate and efficient. In this study, a partitioned coupling strategy is used for the efficient and stable numerical analysis of flexible structures.

#### Implicit Coupling Strategy

The interface between flow and solid disciplines exchanges boundary information such as displacement and pressure to solve FSI problems in a partitioned

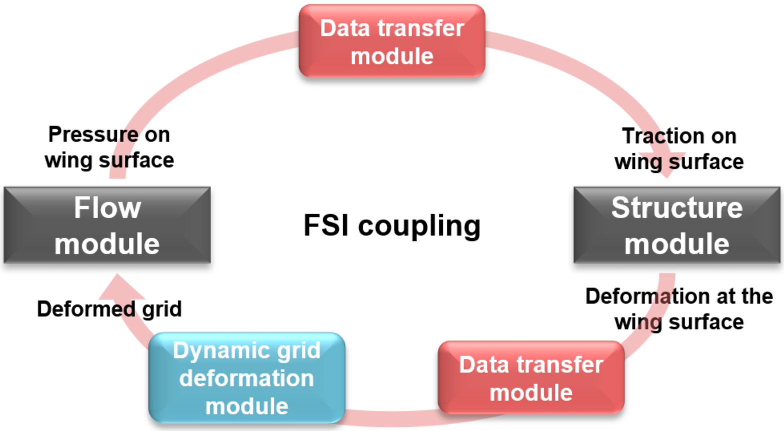


Figure 2.3: Partitioned coupling methodology.

manner. The partitioned strategy can be divided into two large categories by an exchanging manner [9, 75]:

- Explicit coupling strategy: Both the fluid and structure solvers exchange data at the interface once per coupled time step. Although this method is computationally efficient and simple to implement, it may cause numerical instability when used with large deformable and large displacement structures in incompressible viscous flow.

- Implicit coupling strategy: In each coupled time step, both solvers exchange data more than once until they satisfy given convergence criteria. Although this approach has a higher computational cost than explicit coupling, it is more stable than explicit coupling. The flow and structural solvers are coupled with an implicit coupling strategy [76] in this study. Numerical instability may occur due to the thin and enlarging wings, which entail large deformations. Here is a diagram illustrating the implicit coupling strategy shown in 2.4. Flow analysis solver $P_F$ and structural analysis solver $P_S$ obtain results with independent time steps until

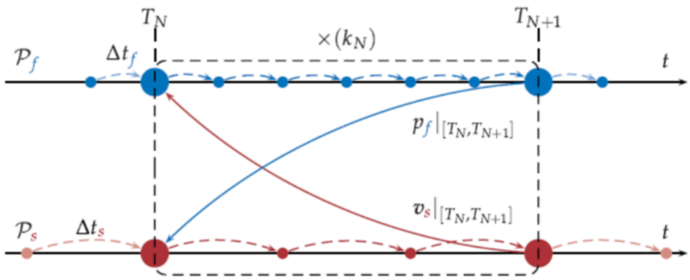


Figure 2.4: Implicit coupling methodology [9].

$t = T_N + 1$, and exchange the data (pressure and displacement). The procedure is applied iteratively until convergence has been achieved.

### 2.3.2 Data Transfer at Nonmatching Interface

As the flow and structure analysis module solves the problem with different grid densities, the fluid-solid boundary doesn't match. A suitable interpolation method is therefore required along the non-matching interface to transfer the data accurately and efficiently.

- Inverse distance weighting [77]: Inverse distance weighting functions are considered only as weighted averages of distance. A lack of consideration of directions leads to inaccurate transmission of data.

- Radial basis function [78]: It is well known that radial basis functions can be used in both scattered and griddled data interpolation. It is possible to obtain accurate approximation behavior using some classical radial basis functions. (Compactly supported functions, thin plate spline function, multiquadric biharmonics, etc.)

- Common refinement [10, 79, 80]: In the common-refinement method, data is transferred between nonmatching fluid-solid interfaces. The method uses a 'common-interface' that satisfies both the fluid grid and the structural grid geometric information. In order to generate a common grid system, edge intersection and point projection algorithms are used. During common refinement, physical variables are integrated. Not only is this method numerically accurate, but it is also physically conservative. To minimize least squares, L2 and Sovolev minimizations are used. If there is no discontinuous transfer of information, L2 minimization can be used for efficient processing. Figure 2.5 shows the generation process of the common surface, and Fig. 2.6 shows validation with previous studies.

### 2.3.3 Dynamic Grid Deformation

In each coupled time step, the body moves and/or deforms, leading to geometric and dynamic deformation of flow grids.

- Delaunay graph mapping [81]: In 2-D analysis, a grid deformation method based on Delaunay graph mapping is applied. In order to generate a Delaunay graph of the domain, some reference points are connected to geometric boundary points on the outer boundary of the computational domain. As the Delaunay graph moves, the computational grid maintains a one-to-one mapping. As a result, the new computational grid can be generated after dynamic movement. Due to its non-iterative nature, this method is efficient. In addition, it can maintain the primary qualities of the grid even under large deformations.

- Transfinit interpolation [82]: In 3-D analysis, transfinite interpolation is used to perturb the interior grid points after a surface boundary is deformed. A multi-block, three-dimensional moving grid method is developed for a fluid main grid system around a flexible body with deforma-

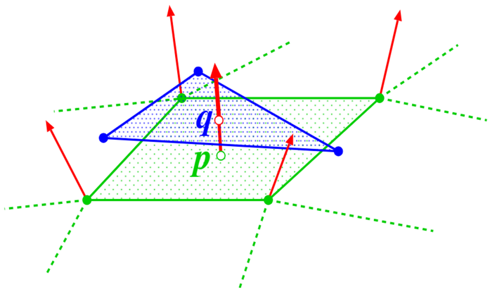


(a) Point projection [80].

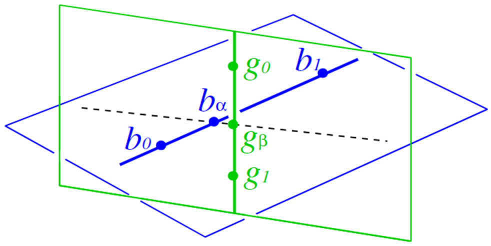


(b) Edge intersection [80].

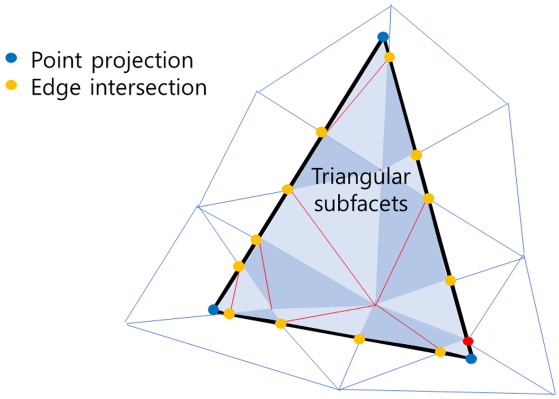


(c) Subfacets for creating new common grids.

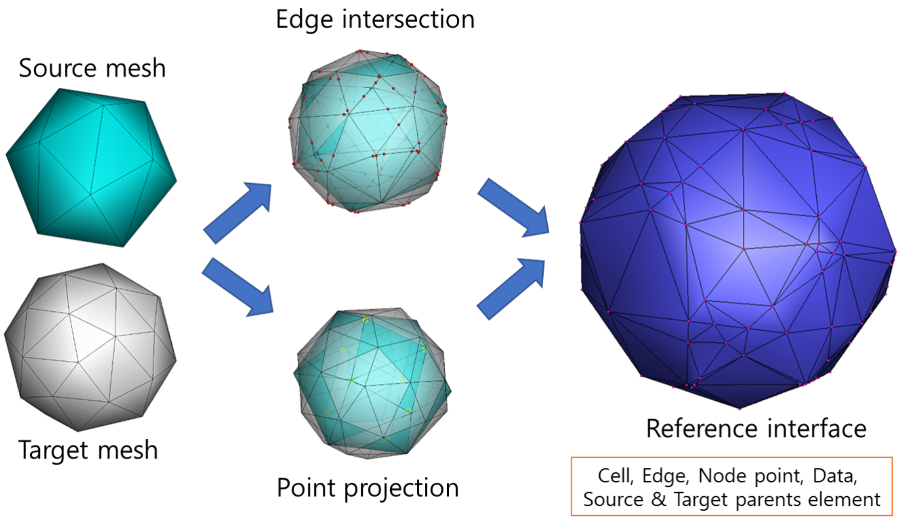


(d) An intersection of edges and a point projection process of a common grid.

Figure 2.5: Common refinement for non-matching interface in 3-D FSI analysis.

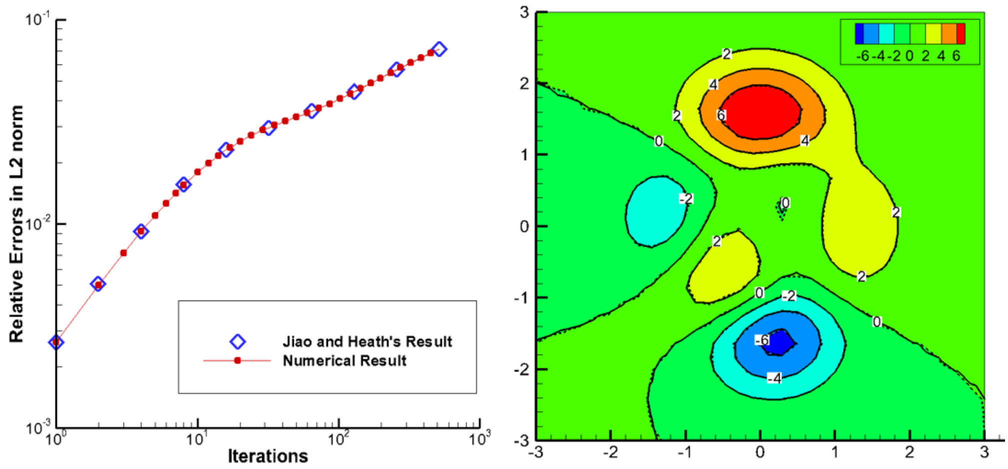


(a) Relative errors in L2 norm. (b) Contour of transfered data.

Figure 2.6: Validation with results from [10].

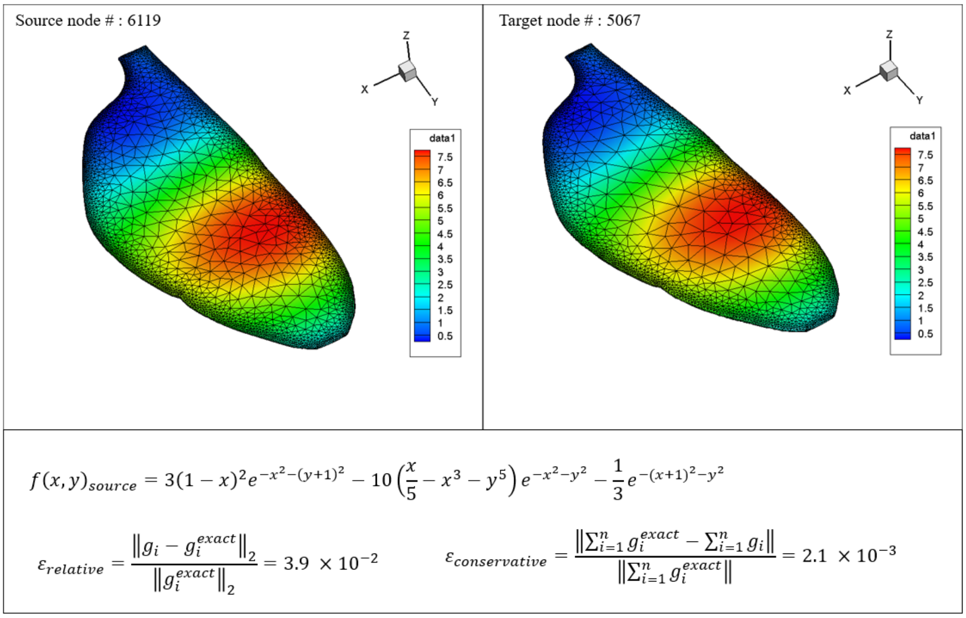


Figure 2.7: Common-refinement results on an arbitrary insect wing shape.

tion. An application of this technique has been found to be highly efficient when analyzing 3-D structured grid systems.

### 2.3.4 Diagram of the Present 3-D Fluid-Structure Coupling.

As shown in Fig. 2.8, implicit coupling is used for FSI analysis. Solutions are determined by exchanging data at every coupled time step until both fluid and structure solutions satisfy convergence criteria. In the gravitational field, the pre-structure solver determines a shape with a twisted shape for the flow solver. The parameter nfsi controls the number of exchanges in order to ensure efficient computations. In the case of nfsi=1, data exchange occurs during every sub-iteration. Interpolation is necessary to transfer data across a non-matching fluid-solid interface. The 3-D FSI analysis uses the radial basis function and the 2-D FSI analysis uses the common refinement method for computational efficiency and accuracy. Furthermore, bodies move and deform as a result of structural deformation, causing grid deformation in computational fluids. A transfinite interpolation method is applied to efficiently in 3-D FSI analysis. And a delaunay graph mapping is used in 2-D FSI analysis. The Overset search algorithm is selectively performed within the physical time step only when grid blocks overlap.

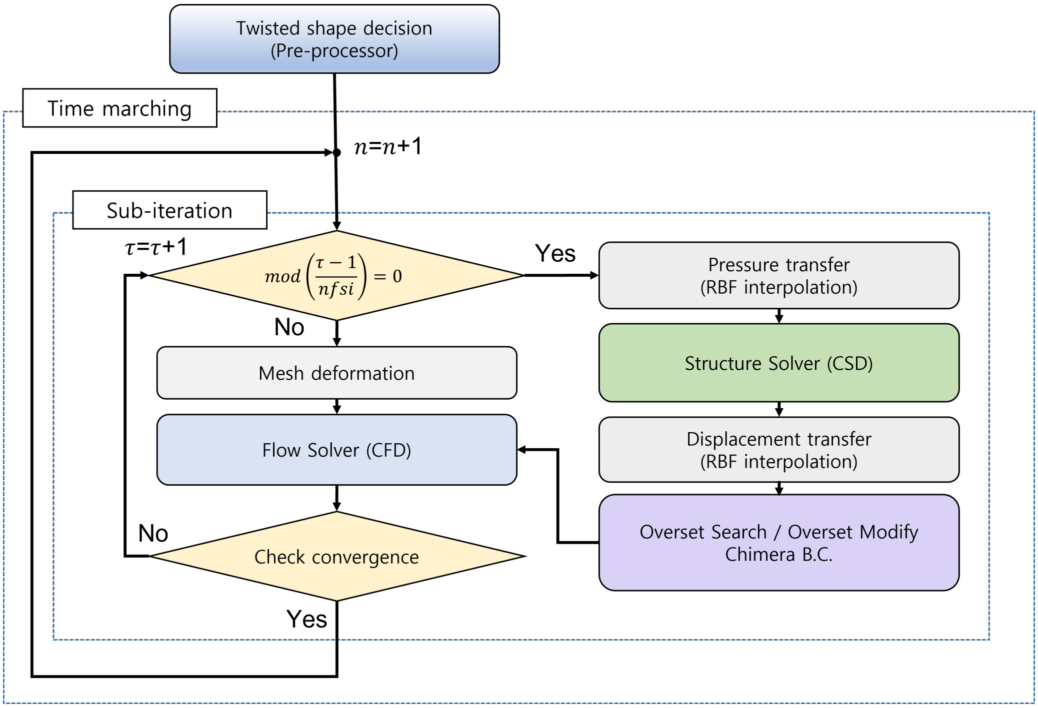


Figure 2.8: Diagram of the present fluid-structure coupling methodology.

# Chapter 3

# Solver Validation

## 3.1 Validation of Flow Analysis Module

Flow analysis solver was validated with Jeong, and the relevant contents are included [11]. To validate the flow analysis module, a rigid NACA0012 airfoil plunging with an amplitude of $h_0 = 0.175$ is chosen. Heathcote et al. conducted water tunnel experiments [28], and Young and Lai performed numerical simulations [83]. The plunging motion can be described by a sinusoidal function, $h(t) = h0sin(2\pi kt^*)$. The dimensionless plunging amplitude $h_0$ is normalized by the chord length $c$, and $t^*$ is the dimensionless time. In this case, $k = f_c/U_\infty$ is the reduced frequency. The plunging frequency is $f$, and the freestream velocity is $U_\infty$. An outer boundary of 20 chords is chosen for grid ($417 \times 145$ O-type grid) with a first wall spacing of $3 \times 10^{-4}$ chords. Time steps are chosen for a plunging period of 1000 steps. The computation is performed for the Reynolds number of 10,000, the plunging amplitude of $h0 = 0.175$, and the reduced frequency of $0.6 < k < 3.0$. The computed propulsive efficiency is shown in Fig.

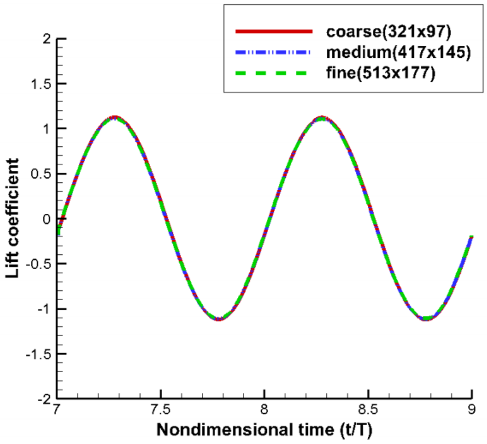


(a) Lift coefficient.

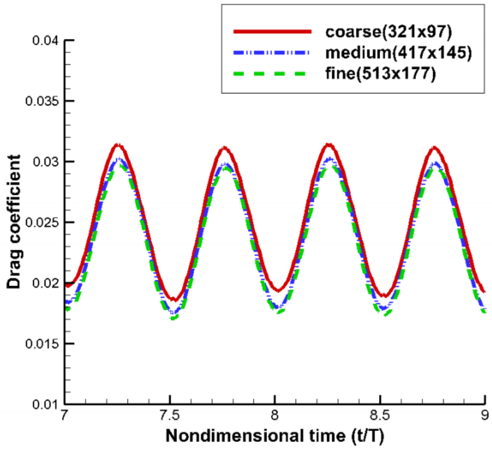


(b) Drag coefficient.

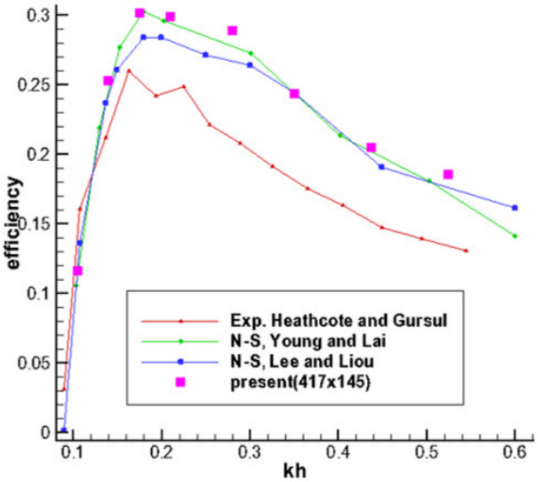


(c) Validation of propulsive efficiency.

Figure 3.1: Validation of plunging airfoil [11].

3.1, which is compared to the experiment and previous computational results. The present results are in reasonable agreement with experimental results, and they are comparable with other computational results. There is a 3-D effect of experiments that seems to explain the difference between the present results and the experimental results.

## 3.2 Validation of Structure Analysis Module

The structural analysis solver was validated through analysis of the cantilevered plate in tip load condition by Cho [8]. In the validation process, static and time-transient analysis results are considered. Validation of the beam-shell assembly will be discussed through the vacuum analysis of the anisotropic Zimmermann wing in Section 3.3.2.

### 3.2.1 Cantilevered Plate in Static Load Conditions

A cantilevered beam loaded with a torque at its free end is considered for geometrical nonlinearity validation. Analyzed conditions are illustrated in Fig. 3.2a and comparisons of tip displacements are shown in Fig. 3.2b. There is a maximum difference of 0.62% between the results and the existing analytical solution. Based on the load factor, Fig. 3.2c shows the relevant deformed configurations [8].

### 3.2.2 Cantilevered Plate in Dynamic Load Conditions

A cantilevered thin plate is subjected to time-varying loads described as expressed by the harmonic function as shown in Fig 3.3a. The displacement of the plate is computed and compared with the results of Abaqus, a commercial software program. ABAQUS and the present analyses are compared in terms

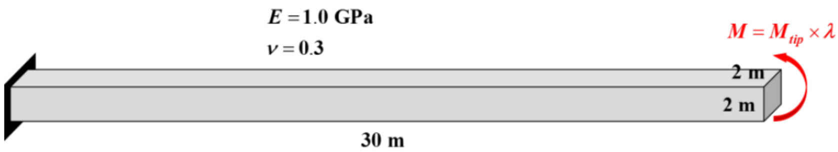


(a) Cantilevered beam under a tip torque

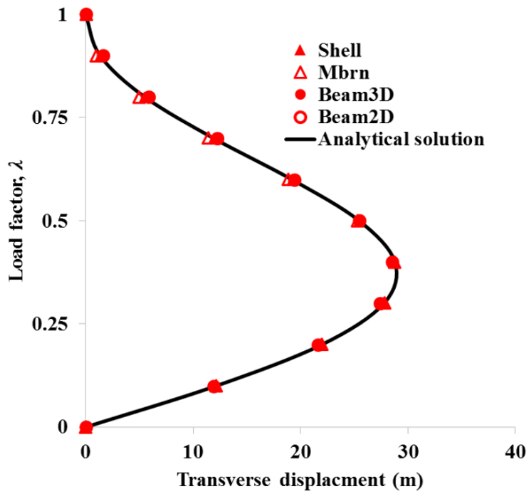


(b) Validation of the load factor-displacement curve.

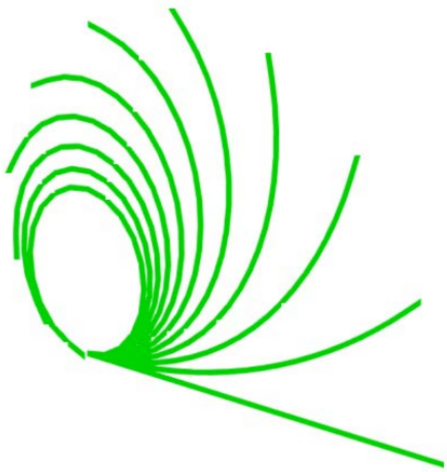

(c) Deformed configuration of cantilevered beam.

Figure 3.2: Validation for caltilevered plate in static load condition [8].

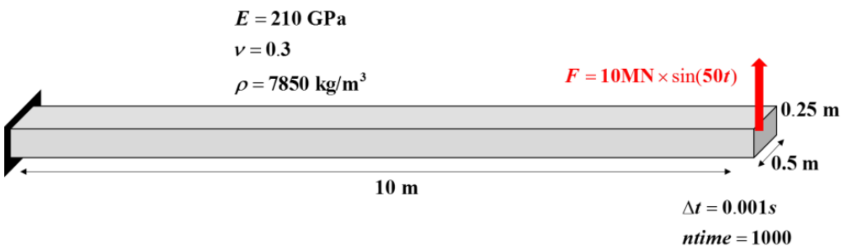


(a) Cantilevered beam under harmonic tip load.

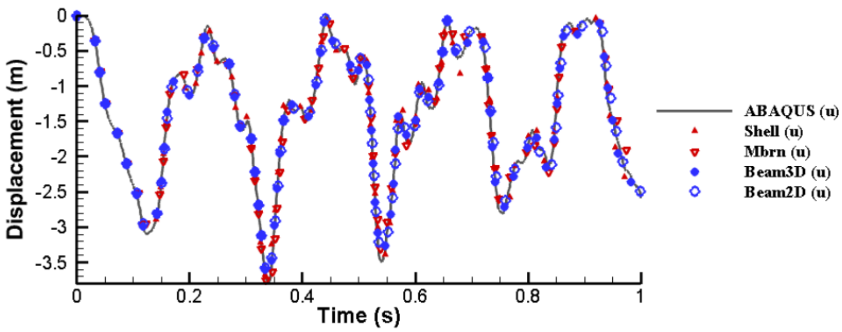


(b) Validation of tip displacement (Axial).

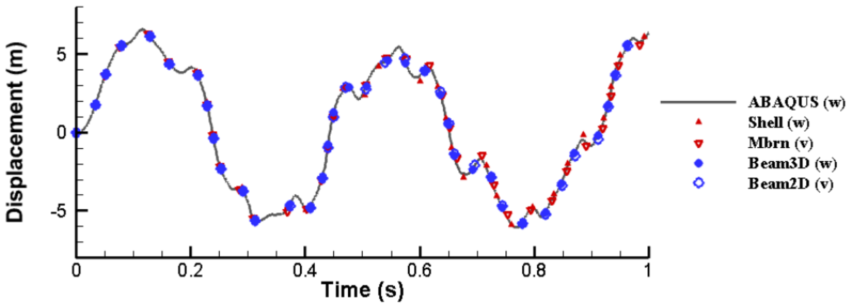


(c) Validation of tip displacement (Transverse).

Figure 3.3: Validation for caltilevered plate in dynamic load condition [8].

of tip axial and transverse displacement response. Figures 3.3b, 3.3c shows a good correlation between the present solver and ABAQUS predictions [8].

## 3.3 Validation of Integrated FSI Program

### 3.3.1 2-Dimensional Plunging Airfoil

The two-dimensional FSI program is validated with Jeong [11] using plunging a flexible airfoil problem with an amplitude of $a_0 = 0.0175$. Heathcote and Gursul conducted water-tunnel experiments [28]. As shown in Fig. 3.4a, the airfoil is composed of a rigid teardrop and a flexible flat plate. The plate is a sheet of uniform thickness with a modulus of elasticity $2.05 \times 1011 N/m^2$, Poisson ratio 0.3, density $7850 kg/m^3$, and length $60 mm$. This teardrop element has a chord length of 30mm and is made. There are two plate thicknesses, $b/c = 1.41 \times 10^{-3}$, where b/c is the plate thickness normalized by chord length c. This plunging motion is the same as in Section 3.1. A flow condition consists of $Re = 9000$, $h_0 = 0.194$, $Str = 0.1\ 0.6$, and Str is defined by $Str = 2fa_0/U_\infty$. Based on the time step sensitivity test, $dt = 4000$ is chosen, and $321 \times 153$ O-type grid is chosen based on the grid refinement test. There are 50 elements used in structural analysis. A comparison of present computational results with experimental results for $b/c = 1.41 \times 10\grave{}3$ and other computations is shown in Fig. 3.4 and Fig. 3.4b shows a normalized wing tip history. Figure 3.4c shows a timeaveraged thrust coefficient for each Str. Both results are in reasonable agreement with experimental data and other computational results.

### 3.3.2 3-Dimnesional Anisotropic Zimmerman Wing in Vacuum

Figure 3.5 shows the sketches of the veins/wing membranes and the schemes for varying their components. As shown in Fig. 3.5b, the layup eading-edge layers

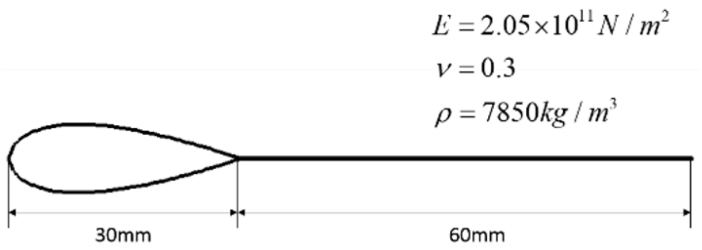


(a) Tip displacement.

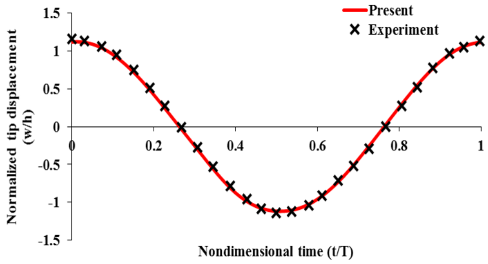


(b) Twist angle.

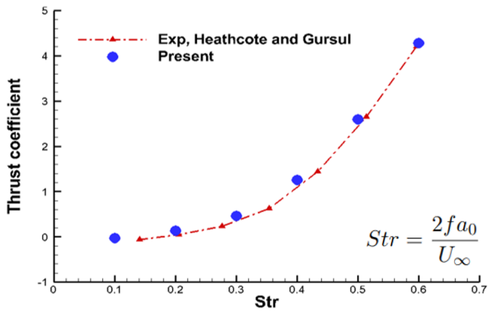


(c) Twist angle.

Figure 3.4: Comparison of the displacement and thrust [11].

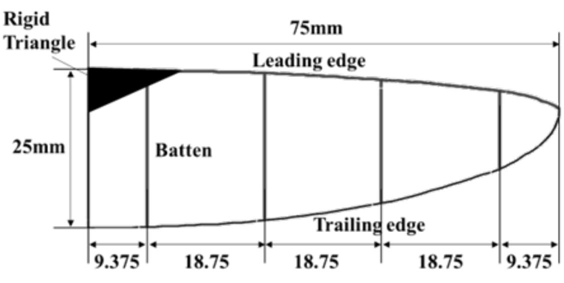


(a) Tip displacement.

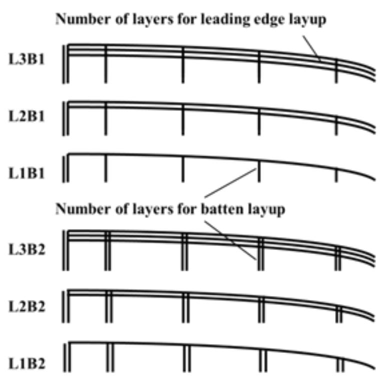


(b) Twist angle.

Figure 3.5: Geometry of Zimmerman wing [7].

Table 3.1: Properties of the batten and membrane in the present structural analysis.

| Beam | | | Shell | | | |
|---|---|---|---|---|---|---|
| $E$ | $G$ | $\rho$ | $E$ | $v$ | $\rho$ | $t$ |
| 233 GPa | 3 GPa | 1740 kg/m$^3$ | 3.0 GPa | 0.44 | 1160 kg/m$^3$ | 20 μm |

vary from 3 to 1 layers of unidirectional carbon fiber, and the batten layers vary from 1 to 2. The carbon layers are 0.8 mm wide and 0.1 mm thick. LiBj describes the resulting wings, where L stands for leading-edge, i for number of carbon fiber layups in the leading-edge, B for amount of carbon fiber laid up in the batten, and j for amount of carbon fiber laid up in the batten. Validation is conducted by comparing the natural frequencies and mode shapes measured in vacuum with those measured by Wu in his experiment [7]. With the flexible beam/shell and the Lagrange multipliers, there are a total of 6,882 degrees of freedom in this analysis. A description of the mechanical properties of these wings can be found in [13]. The present analysis assumes that the material properties are isotropic based on the data in. Information relevant to the property is summarized in Table 3.1. Modal analysis of the wings is conducted with the rigid triangular base as the fixed boundary condition.

The natural frequencies of the present results are well correlated, and the relevant results are shown in Fig. 3.8. In addition, a qualitative comparison of the mode shapes is shown in Fig. 3.9. The discrepancy between the natural frequencies is less than 15%. Moreover, the bending modes are found to be significantly coupled to the torsion modes. The leading-edge batten's stiffness will be more influential when it is higher than the chordwise batten's.

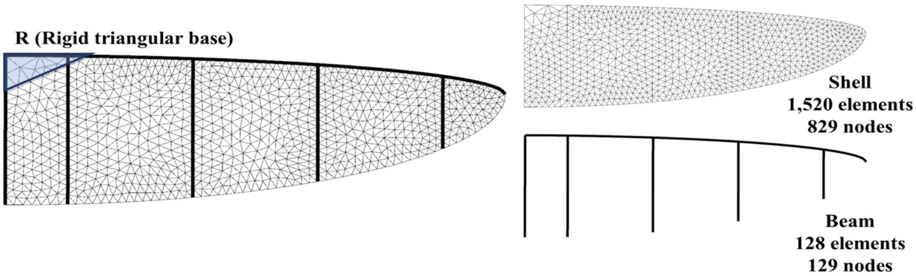


Figure 3.6: Numerical modeling of Zimmerman wing structures.

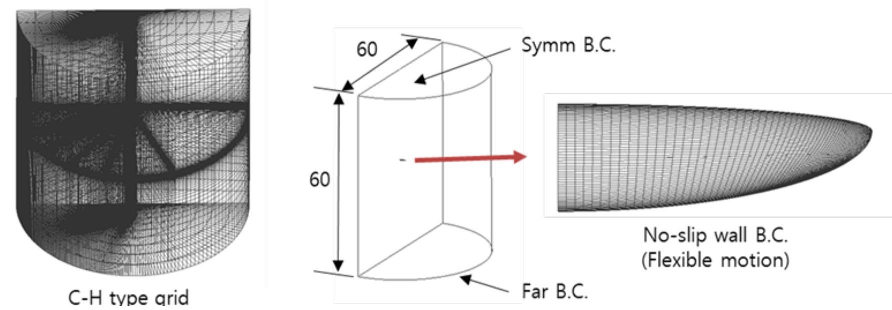


Figure 3.7: Comparison of the mode shapes and natural frequencies.

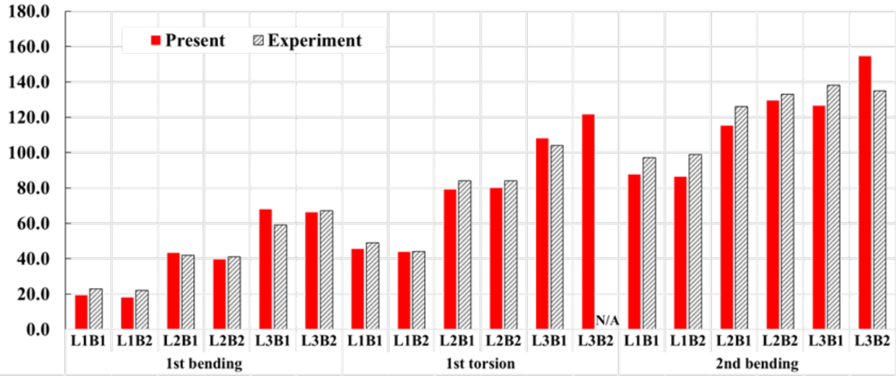


| | L1B1 | L1B2 | L2B1 | L2B2 | L3B1 | L3B2 | L1B1 | L1B2 | L2B1 | L2B2 | L3B1 | L3B2 | L1B1 | L1B2 | L2B1 | L2B2 | L3B1 | L3B2 |
|---|---|---|---|---|---|---|---|---|---|---|---|---|---|---|---|---|---|---|
| | 1st bending | | | | | | 1st torsion | | | | | | 2nd bending | | | | | |
| Present | 19.4 | 18.15 | 43.1 | 39.6 | 67.9 | 66.3 | 45.58 | 43.8 | 79.1 | 79.9 | 108.1 | 121.5 | 87.67 | 86.26 | 115.2 | 129.3 | 126.4 | 154.7 |
| Experiment | 23 | 22 | 42 | 41 | 59 | 67 | 49 | 44 | 84 | 84 | 104 | 0 | 97 | 99 | 126 | 133 | 138 | 135 |

Figure 3.8: Comparison of the mode shapes and natural frequencies.

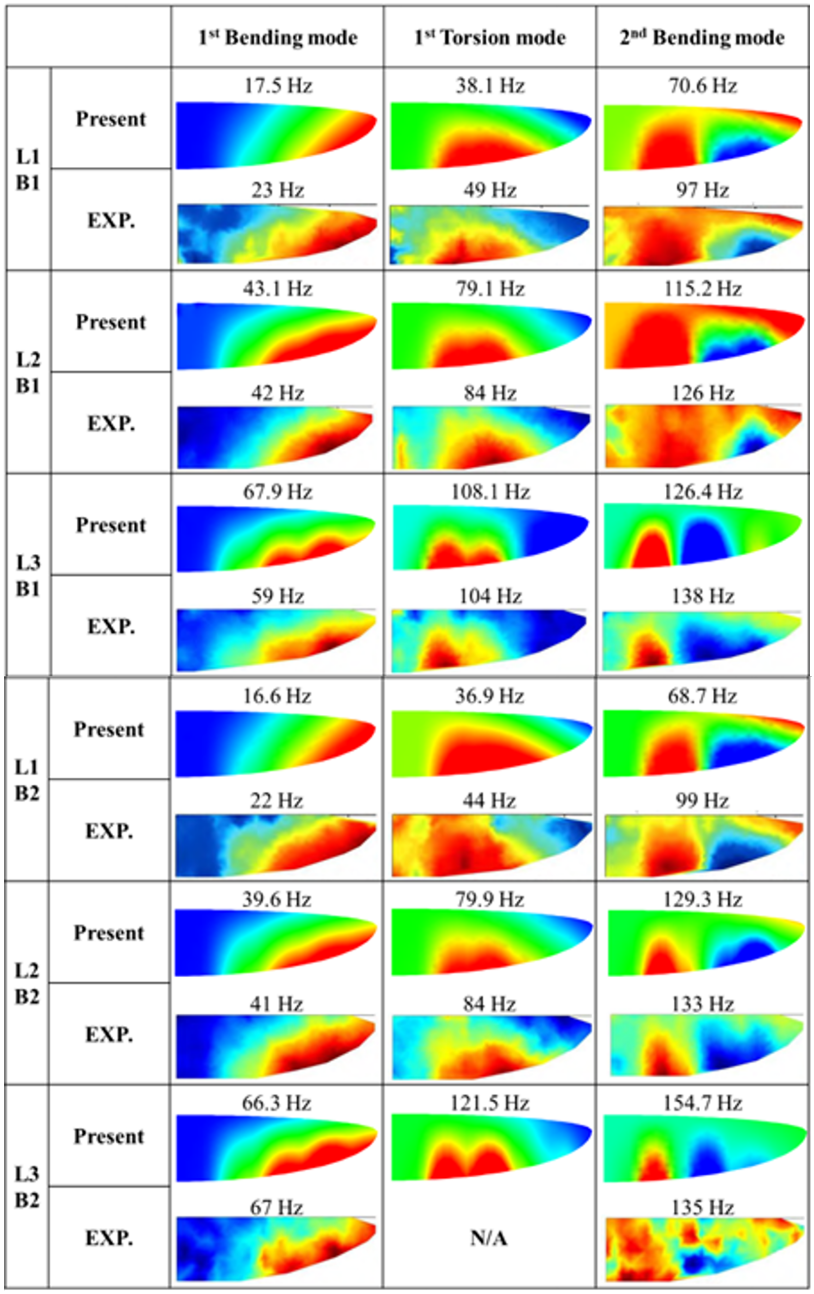


Figure 3.9: Comparison of the mode shapes and natural frequencies.

### 3.3.3 3-Dimnesional Anisotropic Zimmerman Wing in Air

There is validation for flapping tests in air for L2B1 and L3B1 wings, which are anisotropic Zimmerman wings that have been structurally validated in vacuum. This includes the contents published in [52, 84]. Validational cases L2B1 and L3B1 wings are selected, and the mechanical properties are available in [7]. With 128 beam elements, 1,520 shell elements, and the Lagrange multipliers, there are 6,882 degrees of freedom. Based on a comparison of the natural frequencies in Fig. 3.9, it is evident that the computed results appear to be in reasonable agreement with the experimental results. One can see that the bending modes are strongly coupled to the torsional modes based on the mode shapes. Additionally, the stiffness of the leading-edge batten influences wing rigidity more than the stiffness of the chordwise batten. Validation of FSI analysis is accomplished by comparing the displacement and thrust of the two wings in hovering condition. As shown in Fig. 3.7, the fluid solver uses a multiblock C-H type grid with 0.85 million grid points (3,500 cells on the wing surface) from a grid convergence test. According to a time step sensitivity test, one flapping cycle consists of 2,000 time steps. The structure solver uses the same grid as the vacuum test case. The computed tip displacement, twist angle, and thrust are then compared with experimental data [7] and other computational results [13, 39]. Computed results are obtained after three cycles where the thrust has sufficiently converged. After convergence, three to five cycles are averaged to obtain the thrust. Figures 3.10, 3.11 compares the histories of the tip displacement and twist angle at a flapping frequency of 25 Hz and the thrust in terms of the flapping frequency (Fig. 3.12). In each comparison, the present results and previous research are found to be very well correlated.

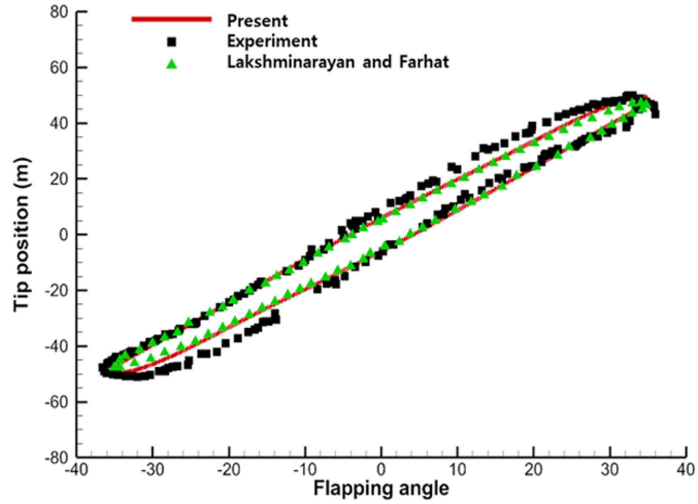


(a) L3B1.

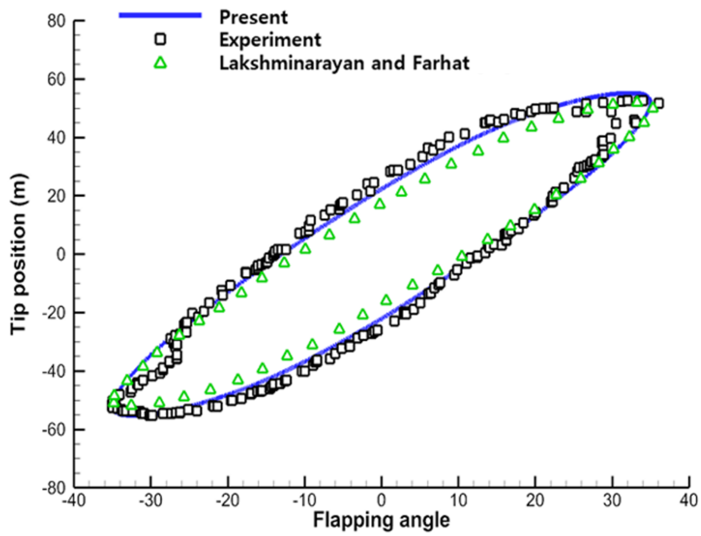


(b) L2B1.

Figure 3.10: Validation of the tip displacement (Comparison with [7] and [12]).

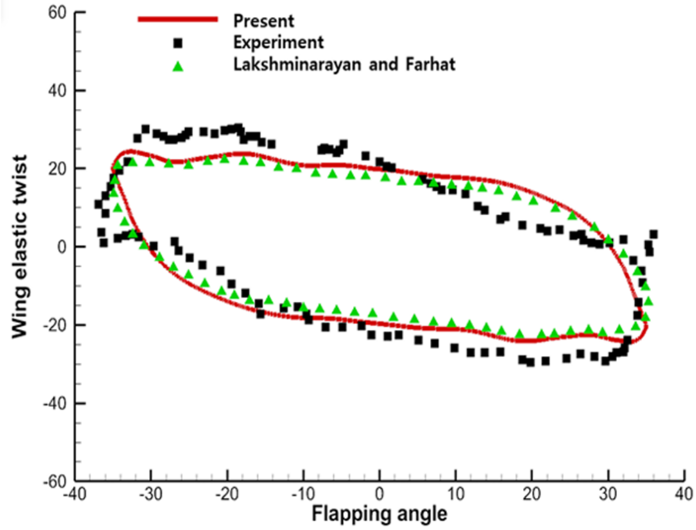


(a) L2B1.

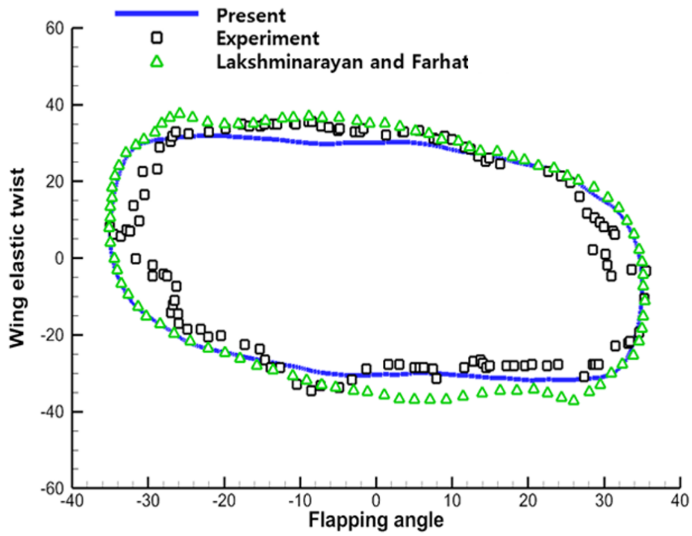


(b) L3B1.

Figure 3.11: Validation of the twist angle (Comparison with [7] and [12]).

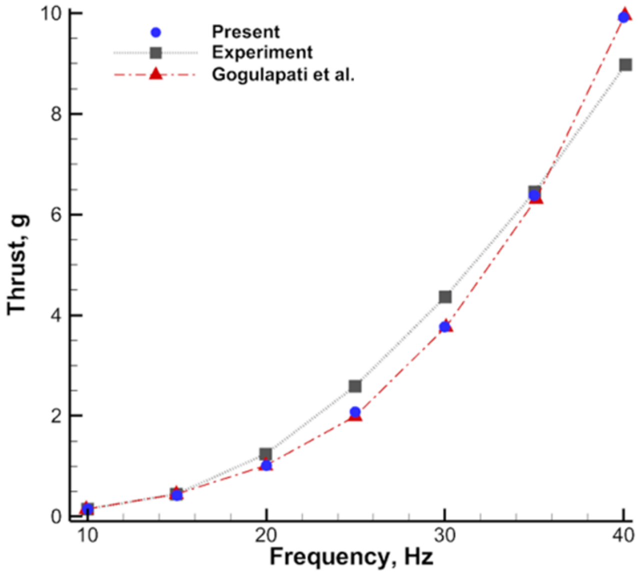


(a) L3B1.

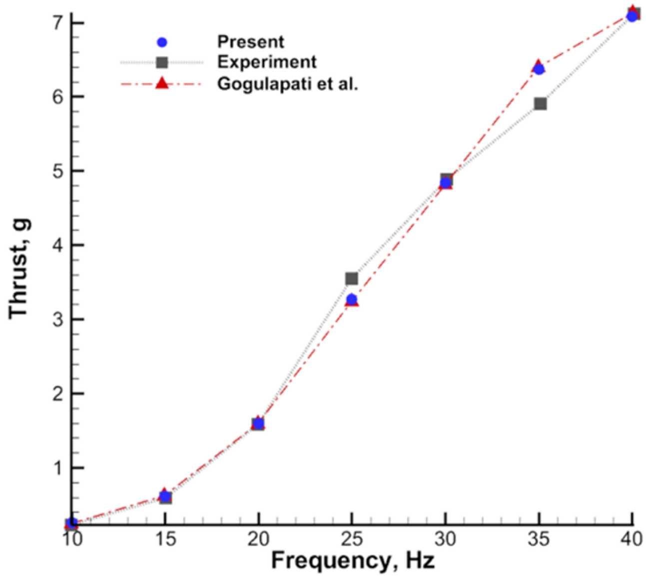


(b) L2B1.

Figure 3.12: Validation of the thrust at different frequencies (Comparison with [7] and [13]).

# Chapter 4

# 2-D FSI Analysis of FW-MAV

## 4.1 Numerical Modeling of FW-MAV's Wing

The FW-MAV developed in this study is analyzed using 2-D FSI (Fig. 4.1). Cambered wings of FW-MAVs move not only as a result of their flexible deformation, but also as a result of their rotation as well. Therefore, rotational springs are added to simulate passive rotation movements. Then, analyze how wing rotation affects aerodynamic performance. In order to conduct the analysis of FW-MAV, the following flow and structure conditions are used. According to Fig. 4.1c, the thrust is the chordwise direction force, while the side force is the vertical direction force of thrust.

## 4.2 Effect of Torsional Spring Coefficient

Figure 4.2 shows the vorticity contour around the FW-MAV's airfoil. The rigid airfoil case is shown in Fig. 4.2a, the flexible airfoil case is shown in Fig. 4.2b, and the flexible airfoil with rotation case is shown in Fig. 4.2c. Looking at the

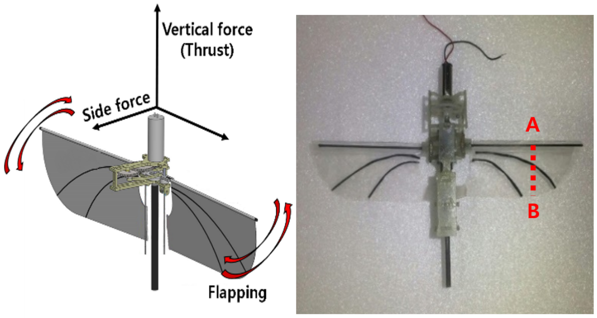


(a) FW-MAV's wing shape.

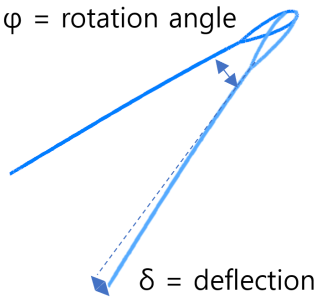


(b) Rotation and deflection angle of the wing.

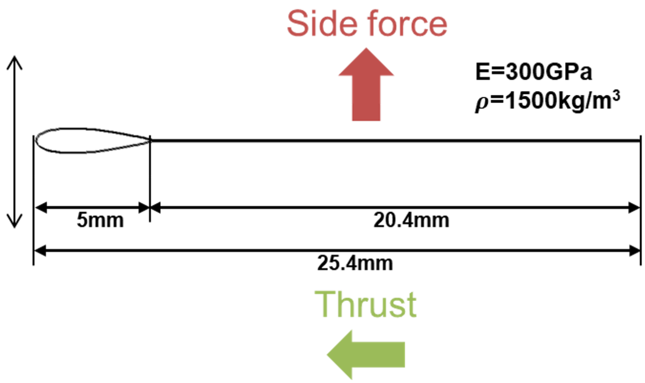


(c) Twist angle.

Figure 4.1: 2-D FSI modeling of the present FW-MAV's wing.

Table 4.1: Results of aerodynamic coefficients for changes in k

| $k$ | 0.005 | 0.007 | 0.009 | 0.01 | 0.011 | 0.013 | 0.015 | 0.017 | 0.019 |
|---|---|---|---|---|---|---|---|---|---|
| $\phi_{amp}$ [°] | 65.74 | 58.66 | 54.76 | 51.62 | 50.01 | 47.77 | 45.91 | 43.77 | 41.63 |
| $c_d$ | 1.02 | 1.48 | 2.07 | 2.31 | 2.62 | 2.91 | 3.04 | 3.45 | 3.65 |
| $c_T$ | 0.37 | 0.93 | 1.22 | 1.30 | 1.39 | 1.54 | 1.68 | 1.81 | 1.64 |

vorticity contour of the airfoil rotated at the leading-edge, downwash flow is formed as the induced vortex is formed. Contrary to rigid airfoil (Fig. 4.2a) and flexible airfoil without rotation (Fig. 4.2b), a rotating flexible airfoil creates a stable flow field (Fig. 4.2c). Fig. 4.3 shows thrust and side force graphs that confirm this observation. In rotation, there is the smallest magnitude of side forces, and the pattern of side forces is regular. In contrast, the magnitude of thrust is larger when rotation is applied. Rotation causes a large change in aerodynamic performance, so to analyze this phenomenon, a parametric analysis is performed by changing the torsional spring coefficient ($k$) to modulate the passive rotation angle ($\phi_{amp}$) of the airfoil (Table 4.1). Maximum thrust occurs at a specific coefficient ($k = 0.017$), and minimum side force occurs at the lowest coefficient ($k = 0.005$).

As a result, it is confirmed that the passive rotation of the airfoil modeling the cambered wing has a significant effect not only on thrust performance and drag reduction, but also on flight stability. However, the torsional spring coefficient, which 2-dimensionally models the passive rotation of cambered wings, is very difficult to apply directly to FW-MAV analysis. To develop practical aircraft with improved performance, 3-dimensional modeling of cambered wings is necessary.

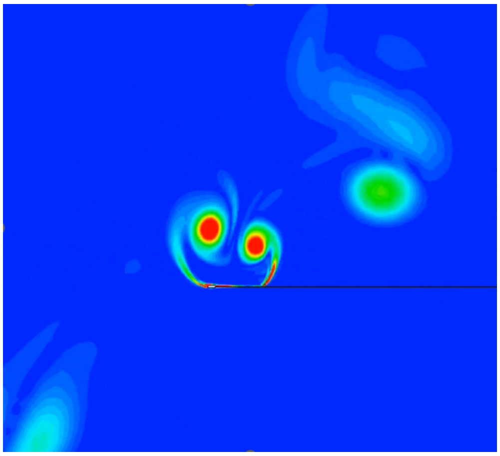

(a) Rigid airfoil.

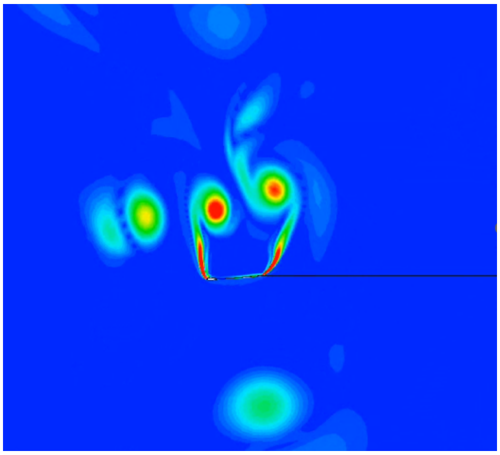

(b) Flexible airfoil without rotation.

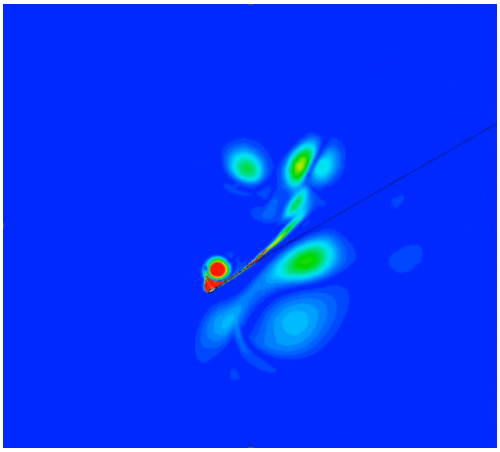

(c) Flexible airfoil with torsional spring ($k = 0.01$).

Figure 4.2: Comparison of the vorticity contour.

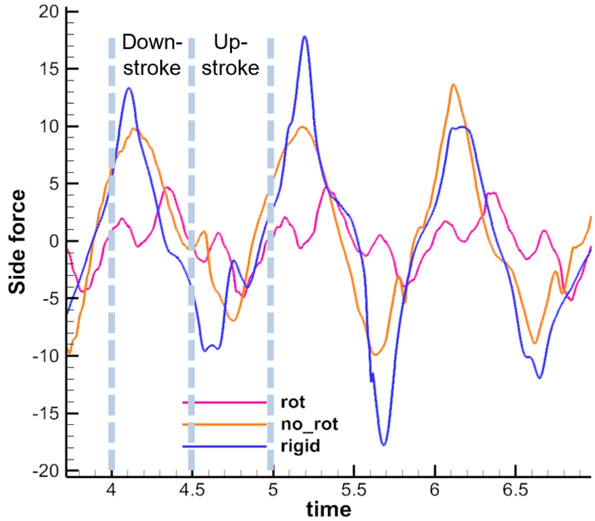


(a) Side force.

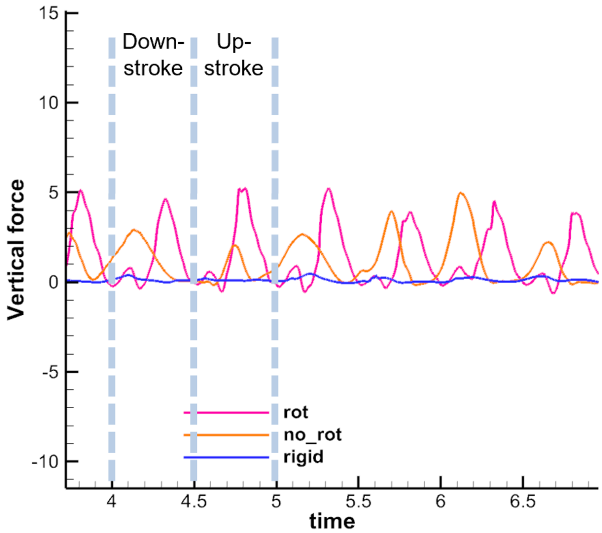


(b) Thrust.

Figure 4.3: Comparison of the side force and the thrust.

# Chapter 5

# 3-D FSI Analysis of FW-MAV

Chapter 5 discusses the 3-D fluid-structure interaction on anisotropic cambered wings with multiple materials of FW-MAVs, including the contents published in [52, 84, 85, 51]. The present FW-MAV has characteristics very similar to the nature hummingbird in terms of flapping frequency, wing length, and mass of the vehicle.

## 5.1 Experimental Setup

For cross-validation, the basic flapping wing shape [55] has been optimized through an experimental study. In Figure 5.2a, the flapping mechanism used in this study is conceptually designed. In the flapping mechanism, the Scotch-yoke linkage and rack–pinion gear are driven by a brushed motor (BLH2402, Blade Co., USA). The mechanism rotates in an alternating manner in order to produce a cosine trajectory. Flapping angles have a maximum amplitude of 82 °. It is modelled using CAD software (Inventor2017, Autodesk Inc., USA) and cut using CNC (TinyCNC-S, Tinyrobo, Korea) which is precise to 0.01 mm. Carbon plate (Carbonmake Co., Korea) is used to enhance the stiffness of the flapping mechanism.

The thrust and power consumption are measured with a load cell (Nano 17, ATI Inc., USA) with a resolution of 1/320 N, and a digital multimeter (8846A, Fluke Co., Ltd., USA). In Figs. 5.3a and 5.3b, one type of wing is tested with a designed camber angle ($\theta$) of 0 ° and one with a designed camber angle of 10 ° respectively. Area (S) of the wings is 1400 $mm^2$, non-dimensional radius ($\widehat{r_2}$) is 0.58, and aspect ratio (AR) is 8. For each wing, thrust and power are collected ten times for 3 seconds and averaged. The high-frequency noise is attenuated with a $2^{\text{nd}}$-order low-pass filter with a cut-off frequency of 200 Hz. Fig. 5.3b shows the experiments are conducted using one wing mechanism. To measure the tip displacement and twist angle, two high-speed cameras are used to track the position of white-colored markers on the wing using the DLTdv digitizing tool developed by Hedrick, T.L. [86].

## 5.2 Numerical Modeling of FW-MAV's Wing

The coordinates of the flapping wing are defined as in Fig. 5.5a. The upward force (positive $y$-direction) is defined as thrust, and the force generated in the $z$-direction is defined as side force. The flapping angle, $\phi$, activated at the root of leading-edge is prescribed as Eq. (5.1) under normal operating condition, where the flapping amplitude $\phi_{amp} = 82$ ° and the flapping frequency $f = 24\ Hz$.

$$\phi \ = \ \phi_{amp}\ (1 - \cos(2\pi f t)\ ), \tag{5.1}$$

As mentioned previously, the initial shape of the cambered wing is obtained from a preprocessor module, in which the inclined camber axis is shifted to the $y$-axis under the gravity field. As a result, the twist angle is initially introduced

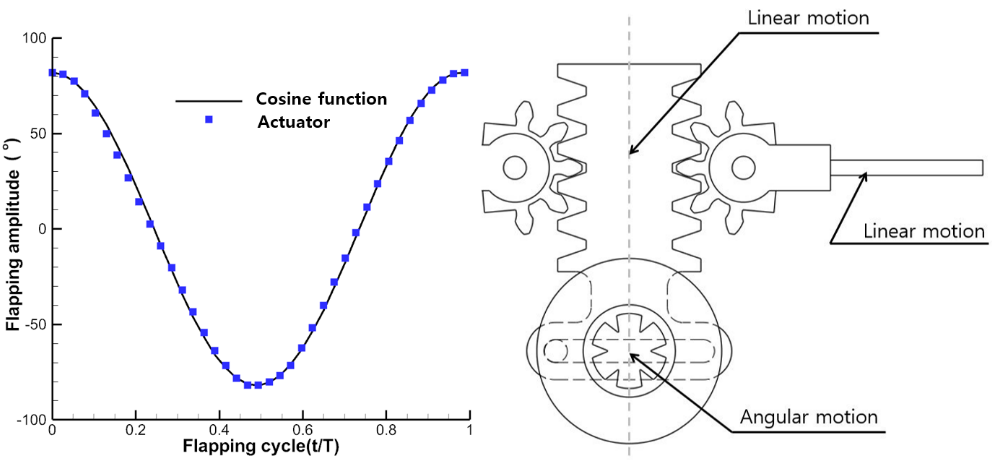


(a) Flapping mechanism of FW-MAV.

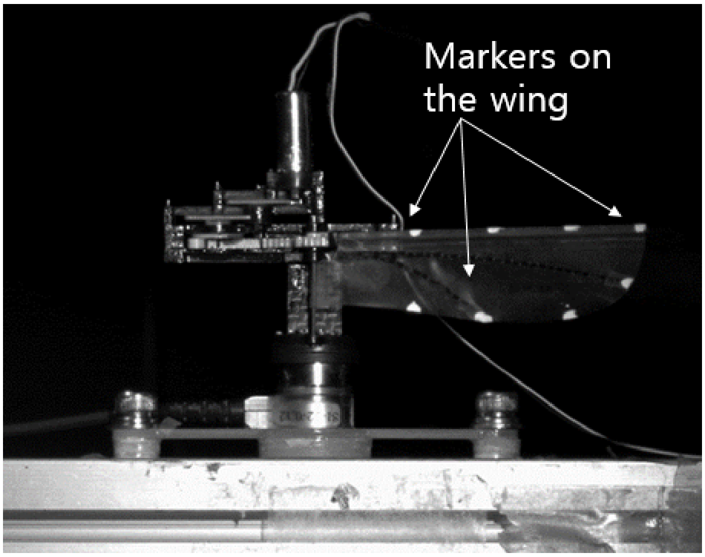


(b) Mounted experimental wing.

Figure 5.1: Experimental system and flapping mechanism.

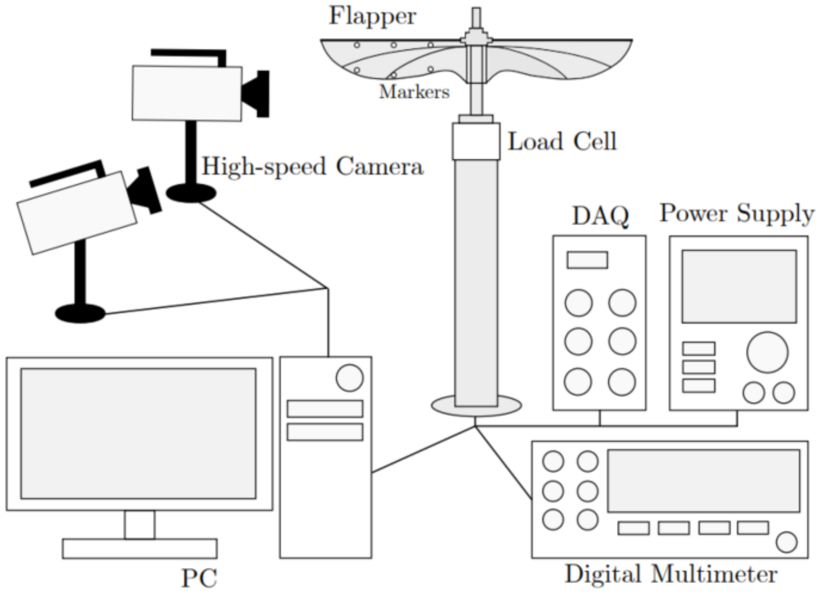


(a) Experimental system and flapping mechanism.

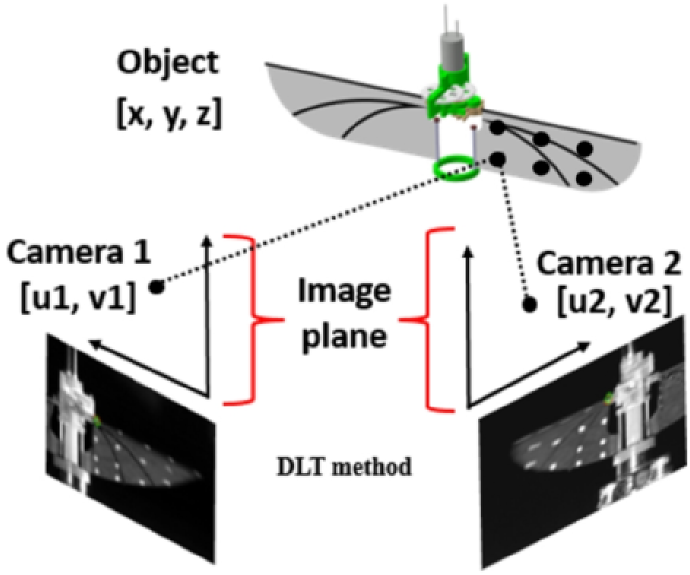


(b) DLT method. The DLT method tracks makers on wing.

Figure 5.2: Experimental setup [14].

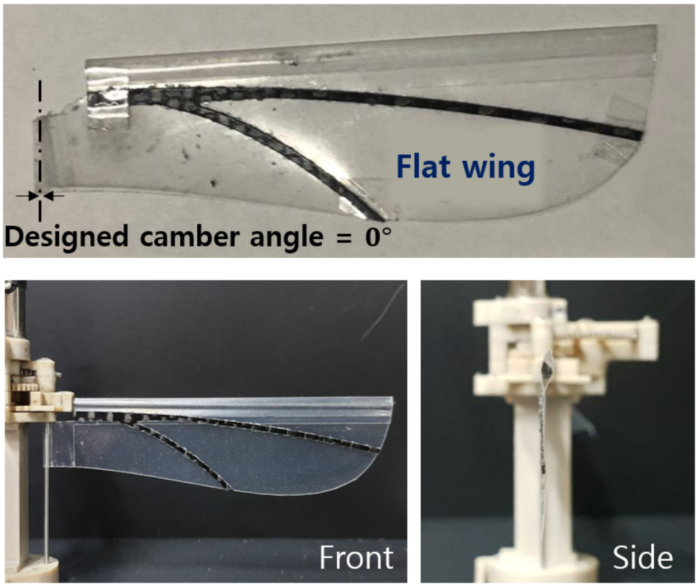


(a) Flat wing shapes.

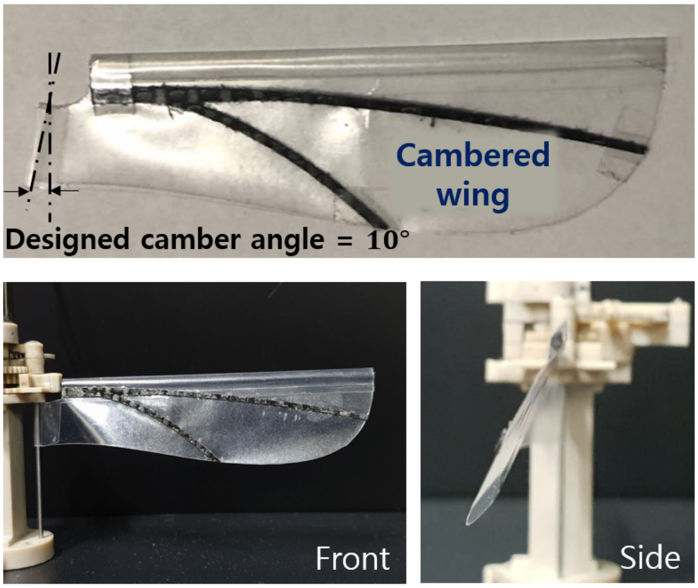


(b) Cambered wing shapes.

Figure 5.3: Experimental system and flapping mechanism.

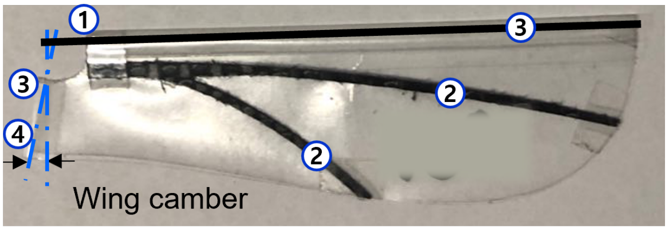


Figure 5.4: Comparison of the mode shapes and natural frequencies.

Table 5.1: Fluid and solid properties of FW-MAV wing.

| FW-MAV wing | | | | |
|---|---|---|---|---|
| **Fluid property** | Flapping frequency [Hz] | Flow speed $[m/s]$ | Flapping angle [°] | Reynolds number |
| | 24 | 10.3 | 164 | 12748 |
| **Solid property** | | Elastic modulus | Density $[kg/m^3]$ | Thickness $[m]$ |
| | Beam (Carbon/Epoxy rod) | $110 \times 10^9$ | 1740 | $\phi = 0.00095$ |
| | Shell 1 (Carbon composite) | $266 \times 10^9$ | 1740 | 0.00025 |
| | Shell 2 (Mylar) | $3.5 \times 10^9$ | 1160 | 0.00004 |

(Fig. 5.5b) and the initial grids for the fluid and structure solvers are generated accordingly. Figure 5.7 shows two types of flapping wings numerically modeled with detailed material characteristics. In order to minimize the skewness of the fluid grid, grid motion for FSI analysis is established by decomposing the whole grid motion into the rigid body motion (grid-moving) and the structural deformation (grid-deformation). Figure 5.8 shows the snapshots of flow grid deformation of the cambered wing due to pronation and supination during the half cycle. As shown in Fig. 5.6b, beam elements are used for the leading-edge vein (carbon/epoxy rod), and shell elements for the wing membrane (Mylar) and the viens (carbon composite plate). In Table 5.1, Shell 1 and Shell 2 denote the shell elements used for carbon composite plate and Mylar, respectively.

From a grid convergence test in vacuum condition, 56 beam elements, 191 shell elements (Shell 1), and 1,132 shell elements (Shell 2) are chosen for the wing structure modelling. In addition, a grid refinement test for the fluid grid system is carried out using coarse (1.5 million) to very fine (3.3 million) grid points with an interval of 0.45 million grid points. A multi-block grid with 2.85 million grid points (7,800 grid points on the wing surface, Fig. 5.6a) is then chosen to satisfy an error less than 1 % of the average thrust. A time step sensitivity analysis is also carried out with a time step of 1/3,000 $t/T$ to 1/7,000 $t/T$, where $t/T$ is the non-dimensionalized flapping time step. The physical time step of 1/5,000 $t/T$ is chosen to avoid numerical instability due to structural vibration.

To secure a free rotation as much as possible, the vertical carbon rod is contained by a circular cylinder made of Mylar (Fig. 5.7b) in the experimental setting. The diameter of the Mylar cylinder has a margin of 0.2 $d_{\mathrm{rod}}$ ($d_{\mathrm{rod}}$; diameter of the carbon rod). As a result, an extra camber angle of 5 $^{\circ}$ is introduced and the actual camber angle is thus increased by this amount. This

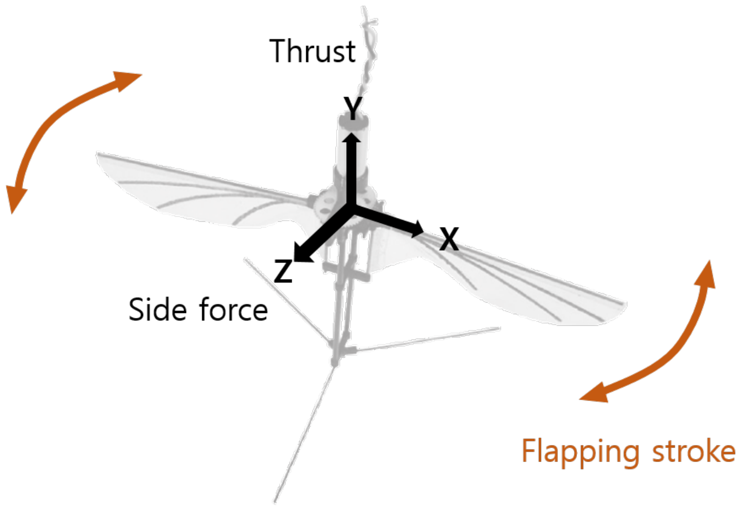


(a) Coordinate for the flapping wing.

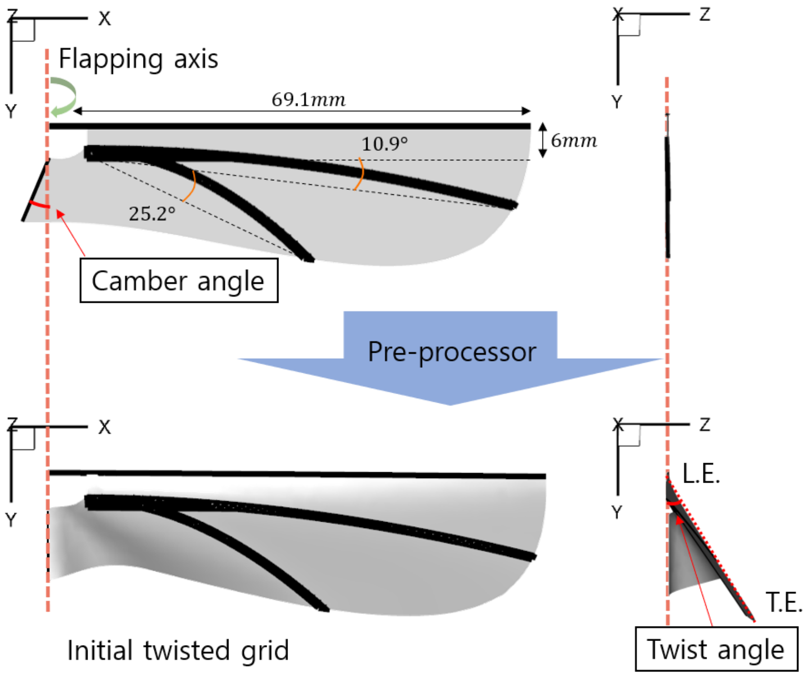


(b) Configuration of the FW-MAV wing.

Figure 5.5: Geometry of FW-MAV wing.

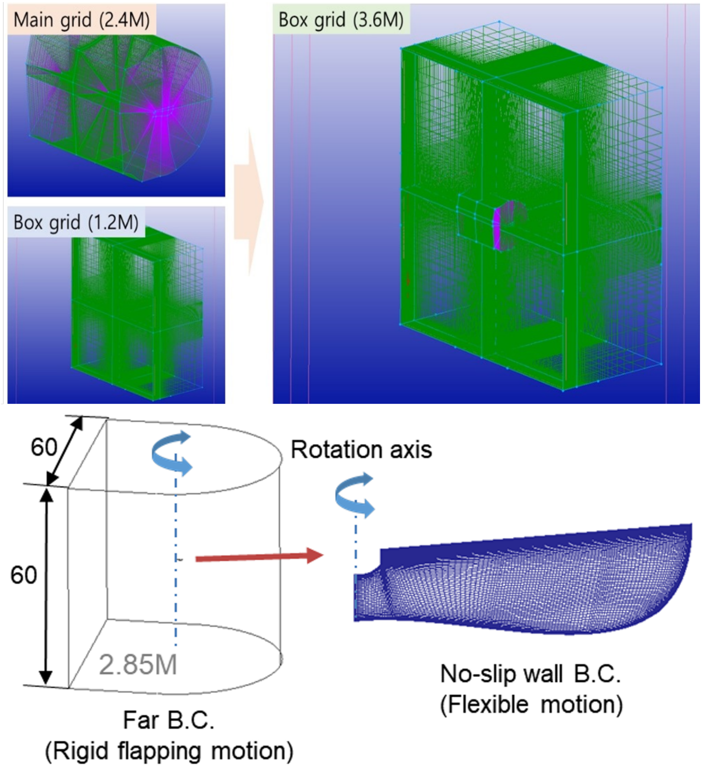


(a) Fluid analysis.

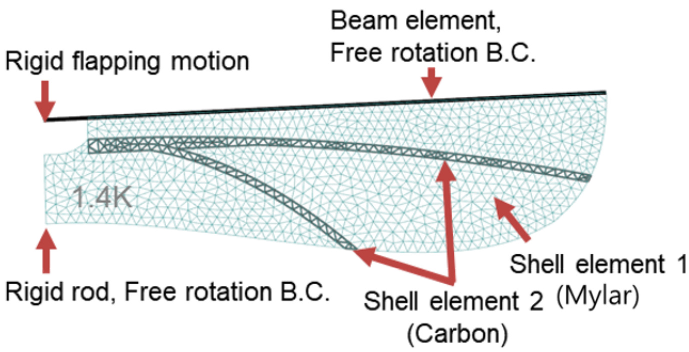


(b) Structure analysis.

Figure 5.6: Numerical modeling of the cambered wing.

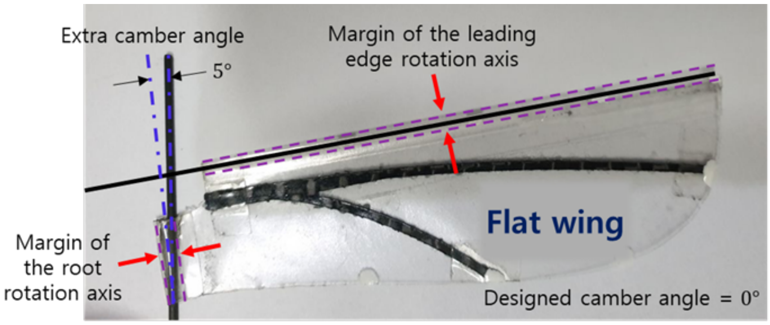


(a) Manufacturing tolerance of the experimental wing.

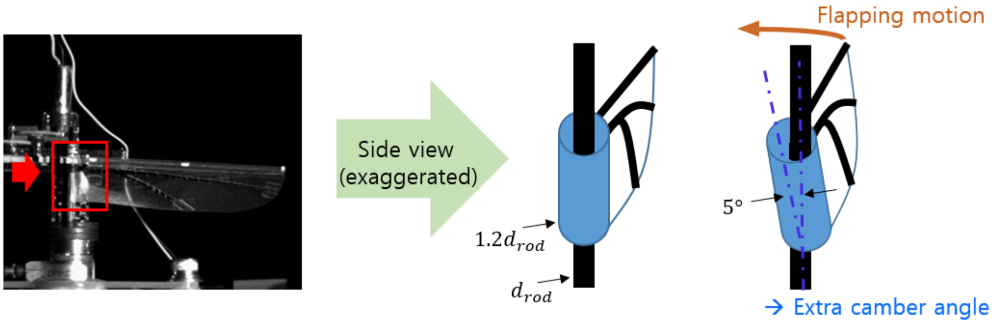


(b) Numerical correction of manufacturing tolerance.

Figure 5.7: Definition of the camber angle.

effect is taken into account in FSI computations.

## 5.3 Cross-Validation of FW-MAV Wing

In this section, cross-validation is conducted against the experimental results obtained in the present study to establish more accurate analyses of cambered wings. Utilizing the validated FSI solver, we compare the aerodynamic characteristics of aeroelastic flat and cambered wings by analyzing the vortex structure. The effects of camber angle are then examined under normal operating condition ($\phi_{amp} = 82$ ° and $f = 24$ $Hz$) in terms of vortex generation, thrust and propulsive efficiency. Finally, by sweeping the operating frequency of the

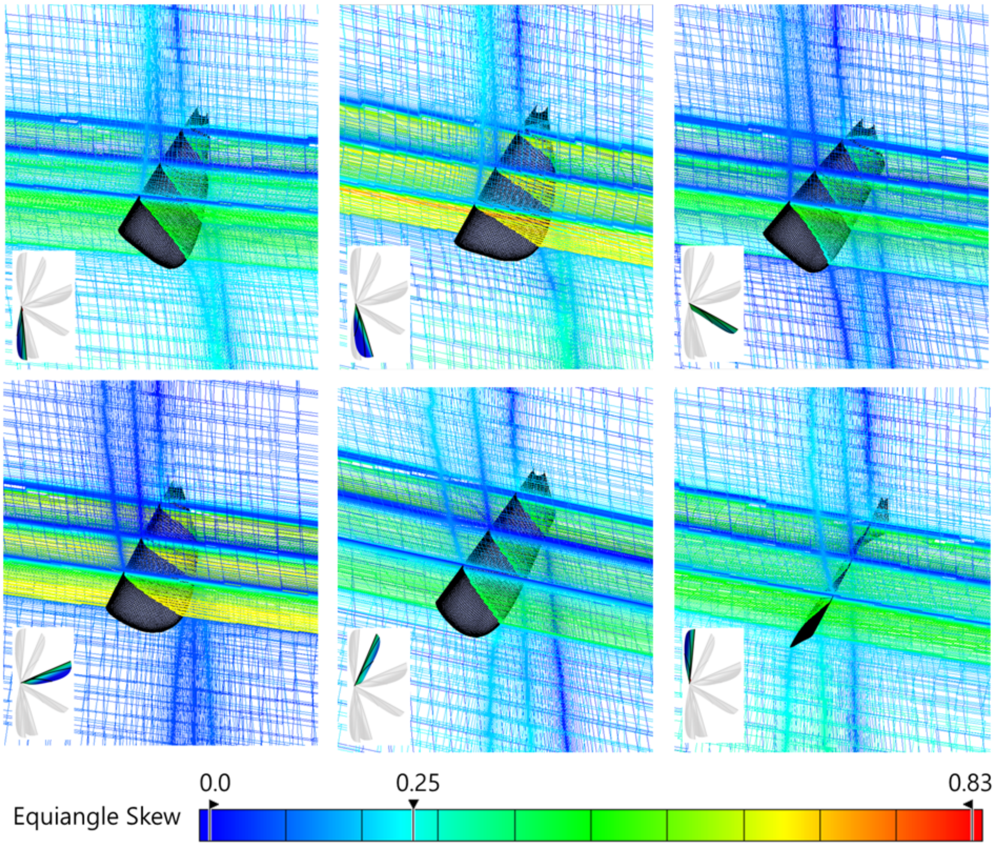


Figure 5.8: Grid deformation of cambered wing for the half cycle.

Table 5.2: Comparison of aerodynamic force.

| **Averaged thrust** | | | |
|---|---|---|---|
| Flat wing | | Cambered wing | |
| FSI analysis | Experiment | FSI analysis | Experiment |
| 6.195 | 6.021 | 6.679 | 6.611 |

FW-MAV, the cambered wing generating the largest thrust and the highest propulsive efficiency at each frequency is identified and the corresponding vortex structure is analyzed.

Since the trajectories of the downstroke and upstroke show symmetric behavior in hovering flight, the upstroke trajectories of the flat wing and cambered wing are compared. Figure 5.10 shows the histories of the wing tip positions (Figs. 5.9a, 5.9b) and the twist angles measured at the 25, 50, and 75 % spanwise location (Figs. 5.10a, 5.10b) for each wing, and the twist angle is measured as defined in Fig. 5.5b. Each comparison confirms a very satisfactory correlation between the experimental measurements and computed results. Table 5.2 compares the averaged thrust of each wing, and the computed thrust is obtained by averaging the values of five to seven cycles where the thrust is sufficiently converged. These results are also in good agreement with the experimental results, with a slight difference of 3 % for the flat wing and 1 % for the cambered wing, respectively. This validates again that the developed FSI solver can accurately capture the flow physics around a FW-MAV's wing.

## 5.4 Comparison of Flat and Cambered wing

Figure 5.11 shows the difference between the vortex pattern on a flat wing and a cambered wing during one cycle. For the flat and cambered wings, flow fields with respect to the twist angle trajectory are examined during the half cycle. As seen in Figs 5.10a, 5.10b, the wing twist angle fluctuates twice during the upstroke, which is magnified in Fig. 5.12. The upanddownness in the twist angle is represented by pronation (P) and supination (S), respectively. These two movements, repeated twice during the upstroke, significantly affects vortex structure.

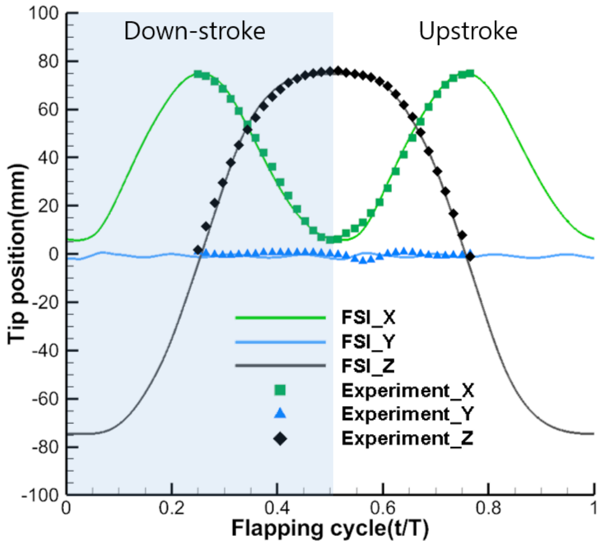


(a) Wing tip position (flat wing).

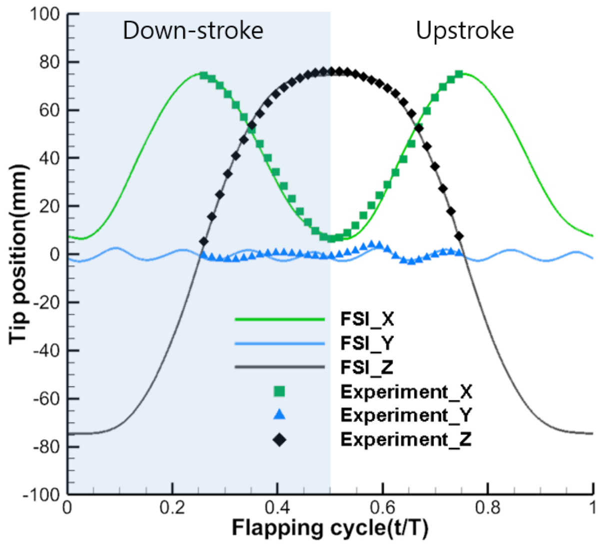


(b) Wing tip position (cambered wing).

Figure 5.9: Validation of the aeroelastic deformations.

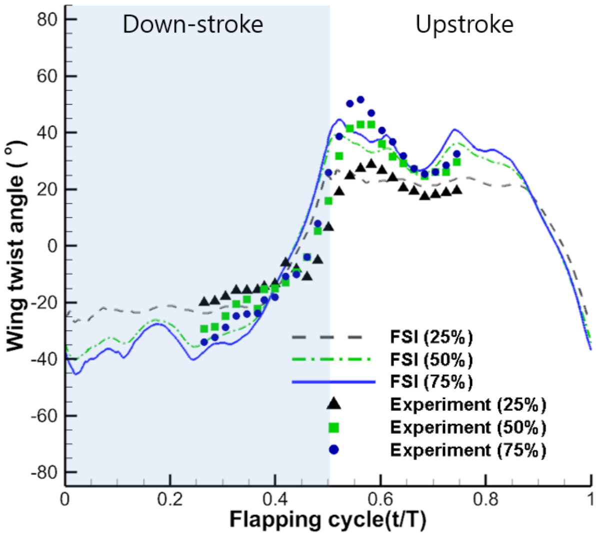


(a) Twist angle (flat wing).

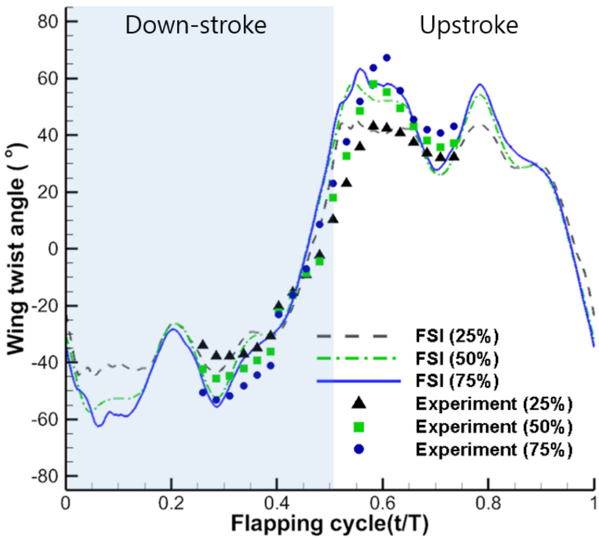


(b) Twist angle (cambered wing).

Figure 5.10: Validation of the aeroelastic deformations.

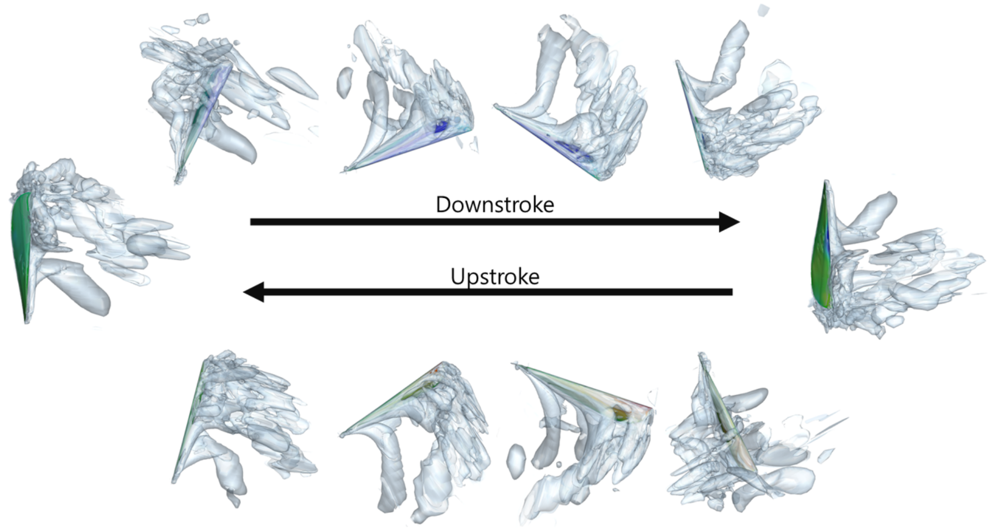


(a) Flat wing.

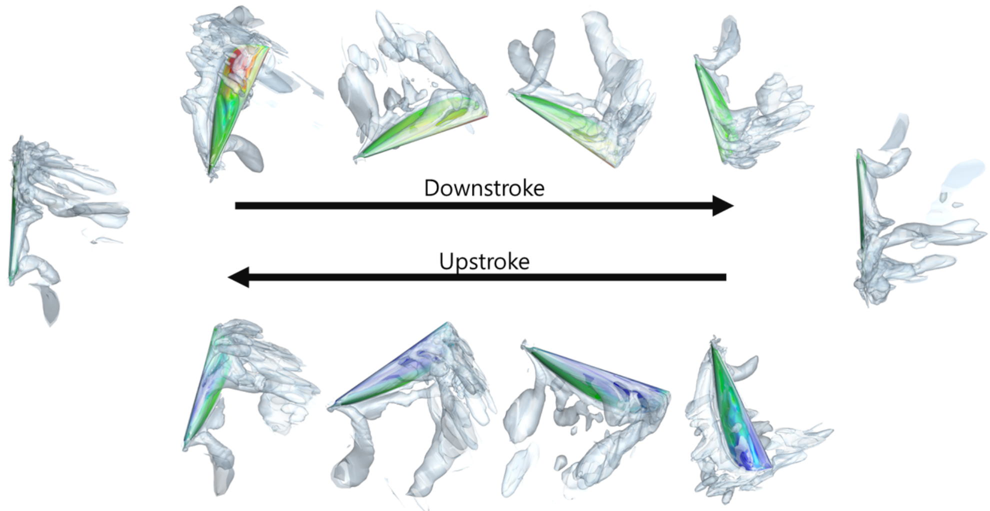


(b) Cambered wing.

Figure 5.11: The aerodynamic characteristics on a flat wing and a cambered wing during one flapping cycle.

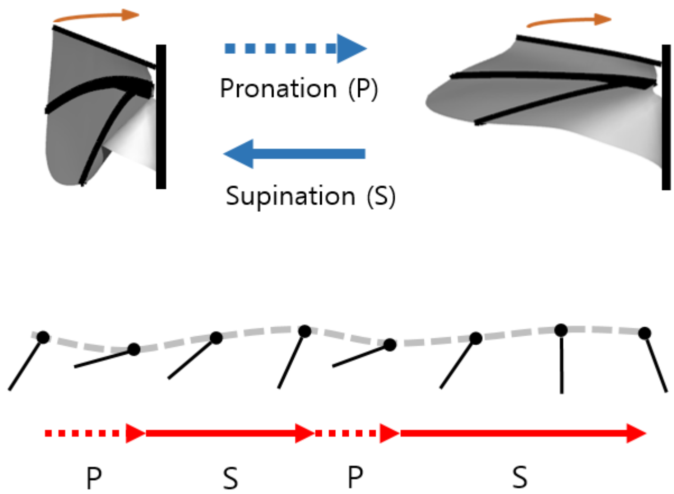


Figure 5.12: Pronation and supination in FW-MAV wing.

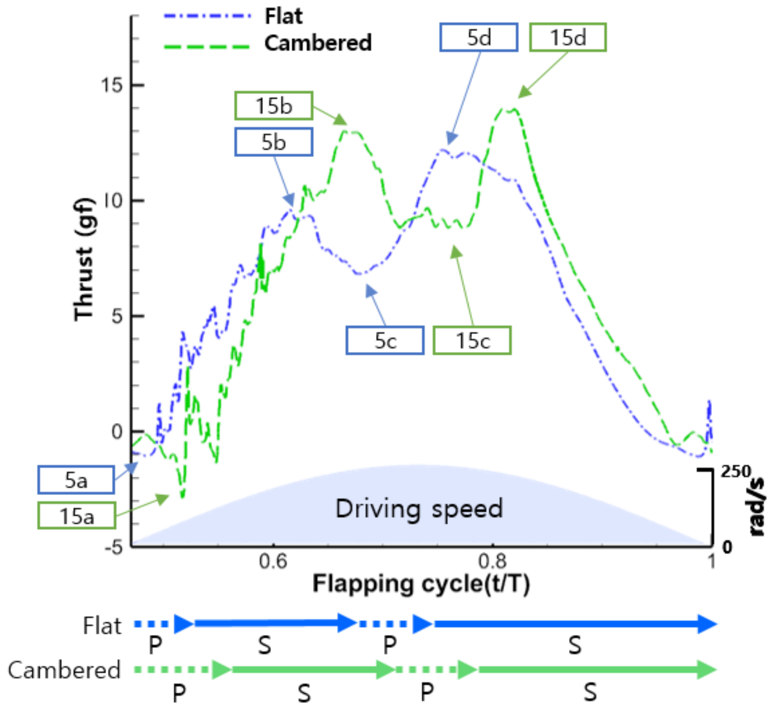


Figure 5.13: Comparison of the flat and cambered wings during upstroke.

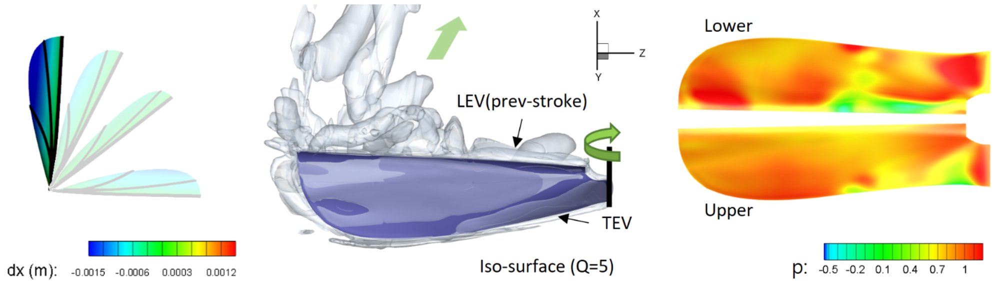


(a) Instant 5a ($t/T = 0.52$).

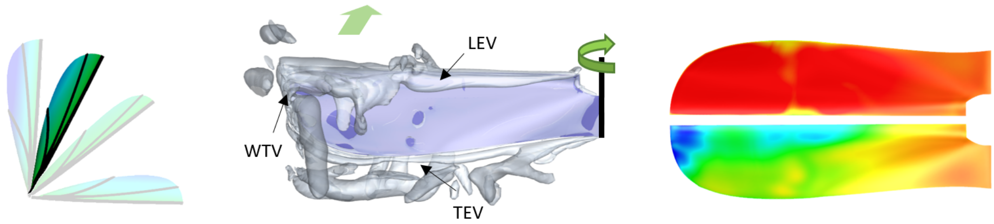


(b) Instant 5b ($t/T = 0.62$).

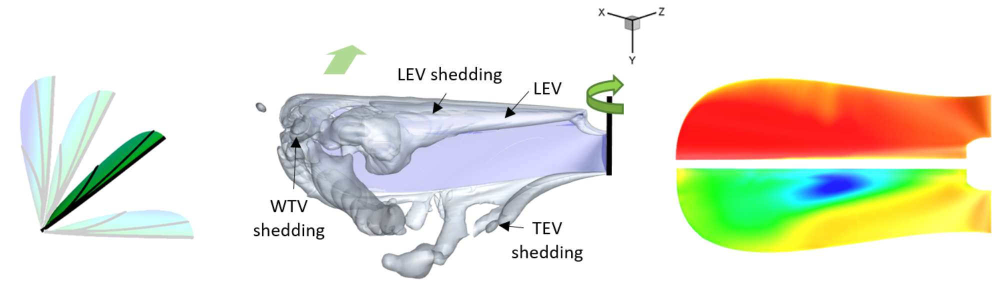


(c) Instant 5c ($t/T = 0.68$).

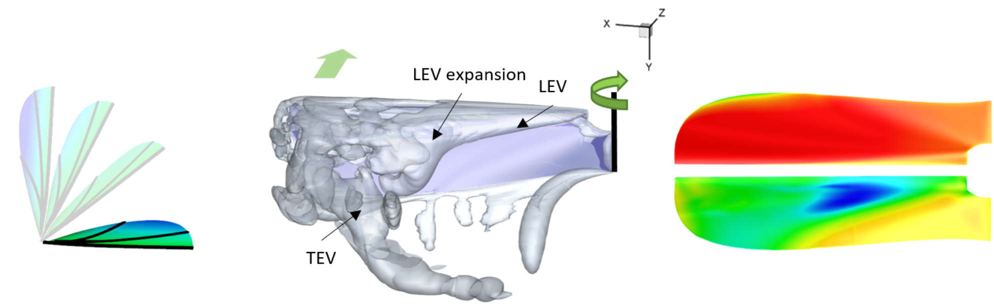


(d) Instant 5d ($t/T = 0.76$).

Figure 5.14: Z-displacement (left), Q-isosurface contour (middle), and pressure contour (right) of the flat wing.

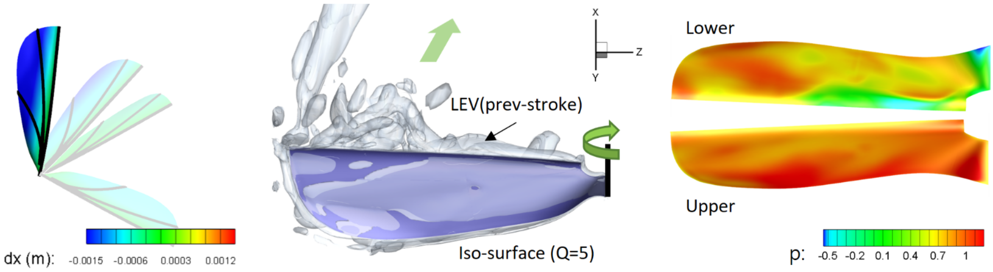


(a) Instant 15a ($t/T = 0.56$).

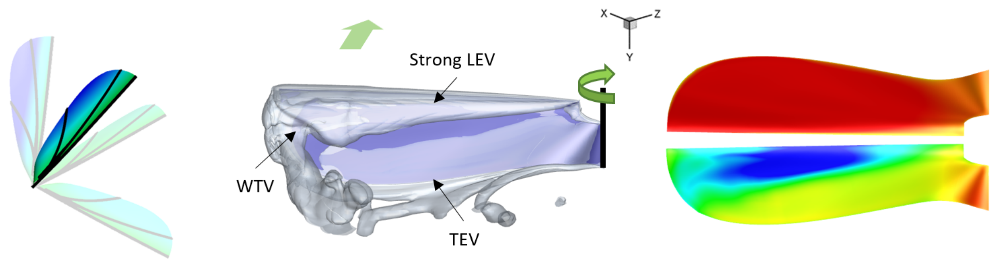


(b) Instant 15b ($t/T = 0.67$).

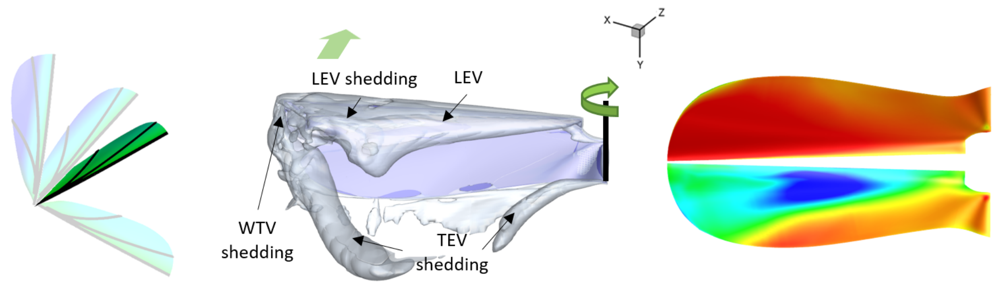


(c) Instant 15b ($t/T = 0.72$).

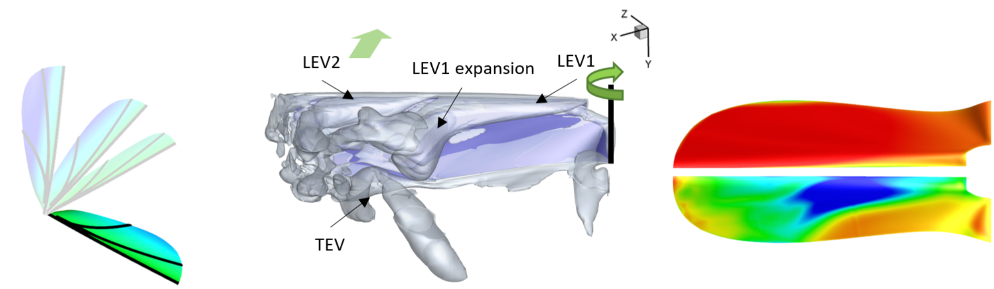


(d) Instant 15d ($t/T = 0.81$).

Figure 5.15: Z-displacement (left), Q-isosurface contour (middle), and pressure contour (right) of the cambered wing.

Figure 5.13 shows the thrust during the upstroke in terms of the twist angle change (pronation/supination) and the driving speed. Two local maxima and two local minima appear in the thrust, and each flow field at the four relevant instants (Instant 5a to 5d, 15a to 15d) is examined. Figures 5.14 and 5.15 show the structural deformation, Q-isosurface, and pressure contours on the upper and lower surfaces for the flat wing (Instant 5a to 5d) and the cambered wing (Instant 15a to 15d), respectively.

At Instant 5a and 15a, the leading-edge vortex (LEV) generated by the previous stoke (downstroke) is attached to the lower surface of the wing, resulting a negative thrust generation. Thrust reduction is relatively smaller in case of the flat wing because the supination of the flat wing develops earlier which facilitates the trailing edge vortex (TEV) on the upper surface (Figs. 5.14a, 5.15a). In addition, due to the elastic deformation of vein by a rapid rotation at the beginning of the stroke, membrane near the wing root significantly oscillates at an amplitude of about $\pm$ 3 $^\circ$ (Figs. 5.10a, 5.10b), causing thrust oscillations at early stroke (Fig. 5.13).

While maintaining supination at Instant 5b and 15b, three types of vortices develop on the upper surface of the wing: the LEV, TEV, and wing tip vortex (WTV). Since supination increases the pressure difference between the upper and lower surfaces, a wide area of vortex attachment develops on the upper surface (Figs. 5.14b, 5.15b). In particular, as the wing is accelerated with the sinusoidal drive motion, the cambered wing yields a wider vortex attachment area with a longer supination (up to 0.71 $t/T$).

Subsequently, the wing starts pronation again, and the pressure difference between the upper and lower surfaces decreases (Instant 5c, Instant 15c). Thus, the attached LEV sheds from the wing tip. However, the location of vortex shedding is not the same because the strength of each LEV is different. For the flat wing, the LEV sheds (Q $<$ 20) at about 63 % of the spanwise location, while, for the cambered wing, it sheds at about 72 % location (Figs. 5.14c, 5.15c).

At Instant 5d and 15d, the LEVs gradually recover its strength by supination. In particular, the second LEV (or LEV2) is clearly developed and stably attached near the wing tip in case of the cambered wing. As a result, the LEV attachment area is widened by about 20 % (Figs. 5.14d, 5.15d).

In summary, the aerodynamic characteristics of the aeroelastic flat wing and aeroelastic cambered wing are compared. It turns out that the wing camber changes the pattern of passive twisting motion (or the pattern of pronation and supination) substantially. As a result, the relevant flow characteristics for thrust generation, such as the vortex generation timing and the vortex attachment area, change remarkably. From the FSI analysis, the experimental observation that the cambered wing produces greater thrust [48, 49, 50, 47] could be explained by comparing the 3-D vortex structures.

## 5.5 Effect of Wing-wing Interaction

From this section, parametric studies on aeroelastic design parameters are analyzed by comparing thrust and propulsive efficiency. The non-dimensional power input, $P_{in}$ of Eq. (5.2), is calculated with the angular velocity and the torque. The propulsive efficiency, $\eta$ of Eq. (5.3), is defined as the ratio of the energy used to the energy input in generating thrust. The results are then obtained by averaging the values of five to seven cycles where the thrust is sufficiently converged so that the thrust difference in each cycle is within 1%.

$$P_{in} = -\int (\boldsymbol{r} \times \boldsymbol{F})\, dV \cdot \boldsymbol{\omega}, \tag{5.2}$$

$$\eta = \frac{\overline{c}_t}{\overline{P}_{in}}. \tag{5.3}$$

An overset technique is used in this section to analyze the wing-wing interaction of a flapping vehicle. In Fig. 5.17, the overset grid technique is applied to the box grid and main grid of the fluid grid system. Overset searches are performed on every real-time step. A symmetric boundary condition is applied to the box grid in order to consider the vortex interaction effect of the wing. In this research, the FW-MAV is manufactured with a pivot distance of at least $2cm$ for stable flapping operation. A comparison is made with five sections with a minimum pivot distance of $2cm$ and a maximum pivot distance of $4cm$ (Fig. 5.17). By changing the pivot distance, there is no noticeable change in thrust or propulsive efficiency. Even, the thrust results are not significantly different from those from a single wing analysis (Fig. 5.18). When the two wings are in contact, as illustrated in Fig. 5.19, the vortex separates completely from the lower surface of the wings. LEV formed immediately after the stroke reverse is relatively small compared to the period when the vortex is at its largest. As a result of its association with sine motion of the present FW-MAV, vortex interaction does not have a significant impact. When stroke reverse occurs, the driving speed is reduced due to this sine motion. As well, the wings are separated by a significant distance. For this reason, wing-wing interaction is relatively insignificant in the present FW-MAV. From this section, the design parameter analysis is performed as a single wing so that it can be performed efficiently.

## 5.6 Effect of Camber Angle

The trend of the thrust and propulsive efficiency is shown in Fig. 5.20. The camber angle varies with an interval of 2.5° from the minimum of 5° to the

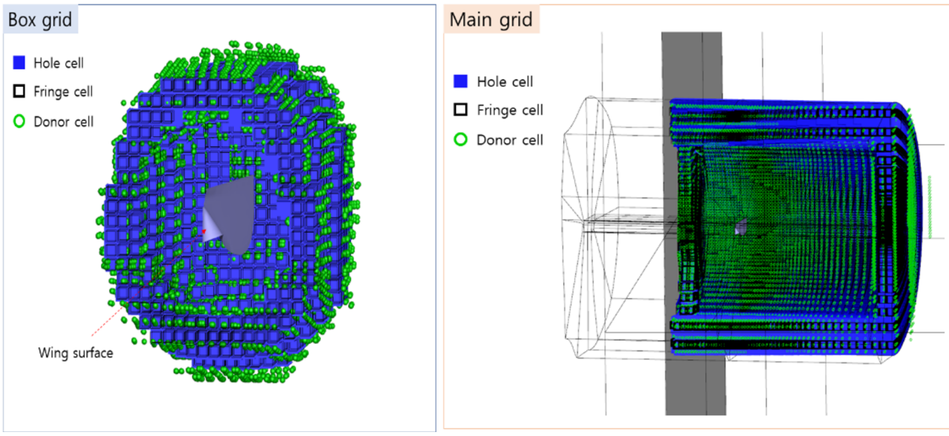


Figure 5.16: Overset grid system of fluid module.

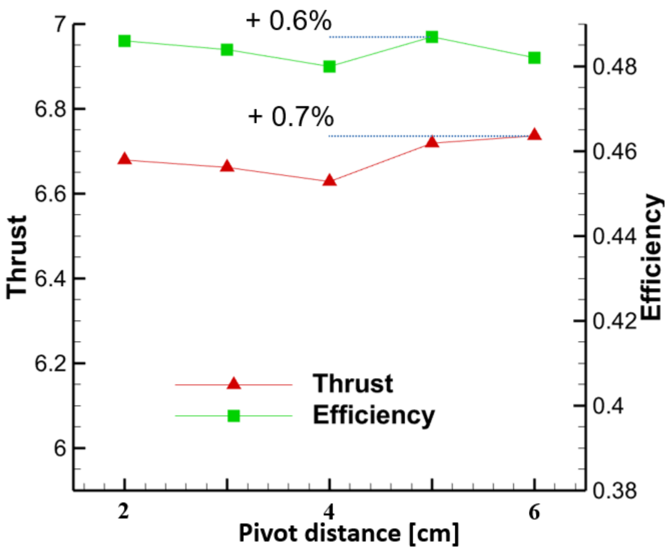


Figure 5.17: Aerodynamic performance according to the pivot length.

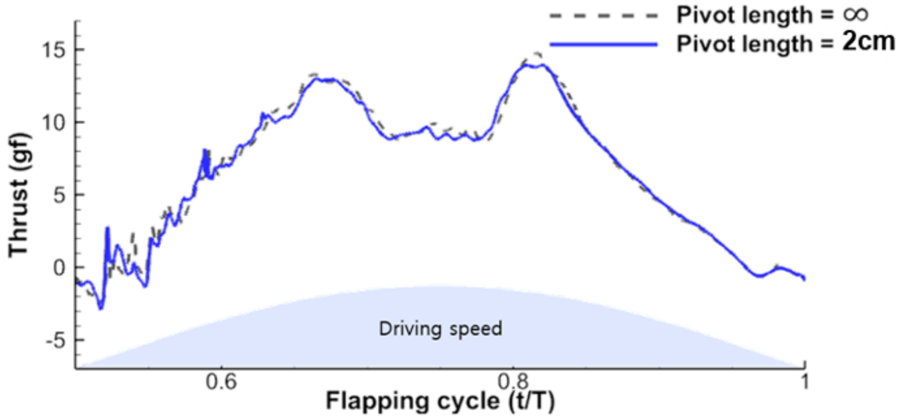


Figure 5.18: Comparing the thrust over time.

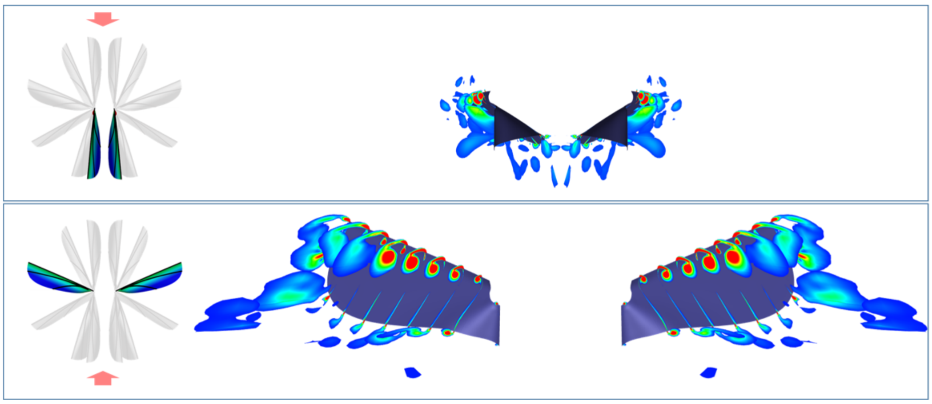

Figure 5.19: The vortex pattern of the wing with pivot length = 2 cm (upper: $t/T = 0$, lower: $t/T = 0.56$).

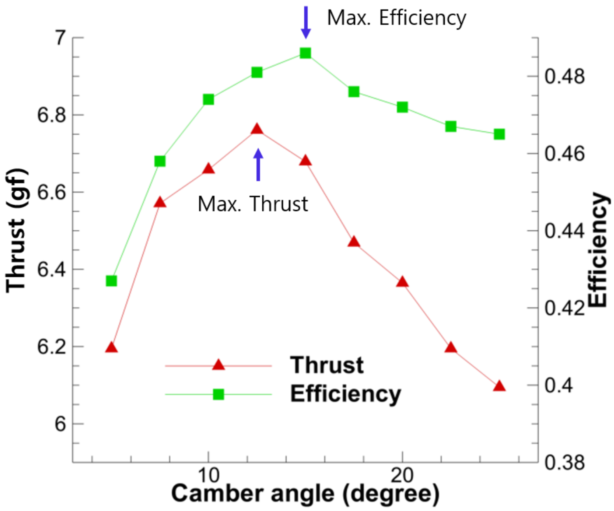


Figure 5.20: Variations of the thrust and propulsive efficiency in terms of camber angle.

maximum of 25°. The largest thrust is shown to occur at a camber angle of 12.5 °, and the highest propulsive efficiency at a camber angle of 15 °. Compared to the case of the flat wing, the thrust and propulsive efficiency is improved by about 9 % and 14 %, respectively.

Aerodynamic characteristics at thee different camber angles (5 °, 12.5 ° for the thust and 15 ° for the propulsive efficiency, and 25 °) are compared to understand why the thrust and propulsive efficiency become climactic at a particular camber angle. Figure 5.22 examines aerodynamic force by dividing a half stroke into four phases.

In the first phase, the smaller the camber angle, the greater the thrust is generated. Figure 5.23 shows the surface pressure distributions at three spanwise locations and the vorticity contour of the 75 % spanwise location of each wing at 0.56 $t/T$. In the case of 5 ° cambered wing, the LEV and the TEV on the upper surface is strongly generated owing to the supination at the early

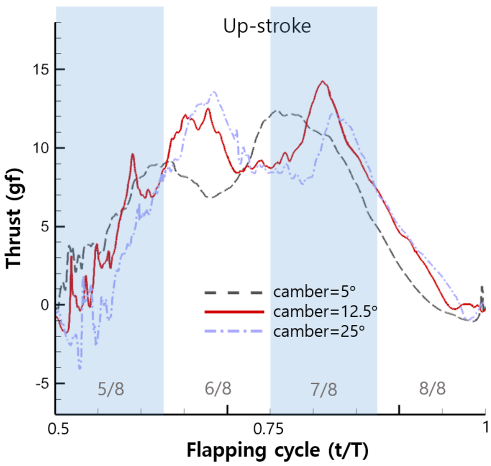


(a) Thrust variation over time.

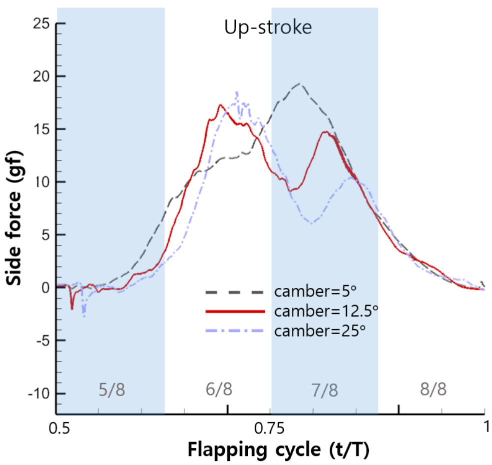


(b) Side force variation over time.

Figure 5.21: Comparison of sectional aerodynamic performance.

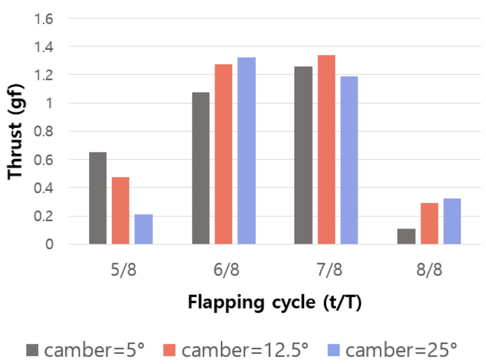


(a) Thrust performance in four phases.

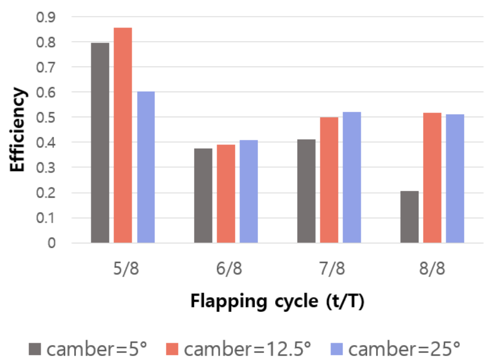


(b) Propulsive efficiency performance in four phases.

Figure 5.22: Comparison of sectional aerodynamic performance.

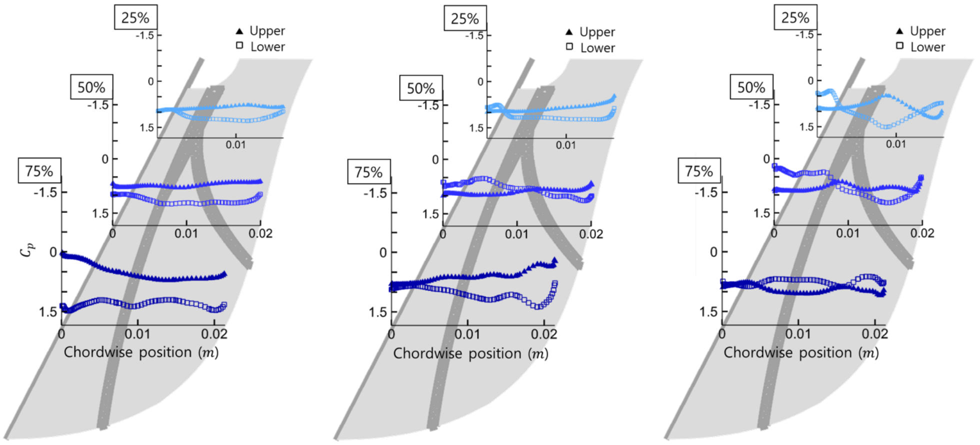


(a) 5 ° cambered wing. (b) 12.5 ° cambered wing. (c) 25 ° cambered wing.

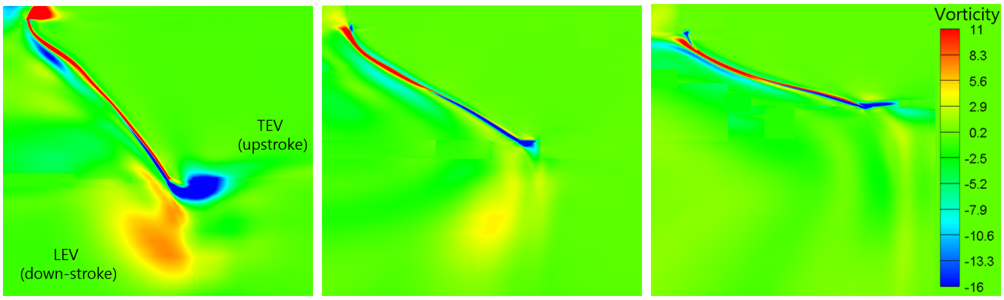


(d) 5 ° cambered wing. (e) 12.5 ° cambered wing. (f) 25 ° cambered wing.

Figure 5.23: Comparison at the middle of the first phase (t/T = 0.56): Chordwise pressure distribution and cross-sectional vorticity contour at 75% spanwise loaction.

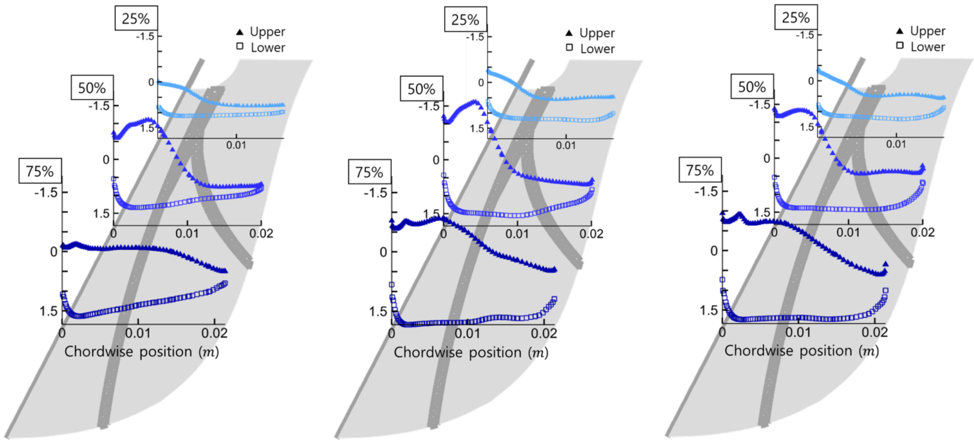


(a) 5 ° cambered wing. (b) 12.5 ° cambered wing. (c) 25 ° cambered wing.

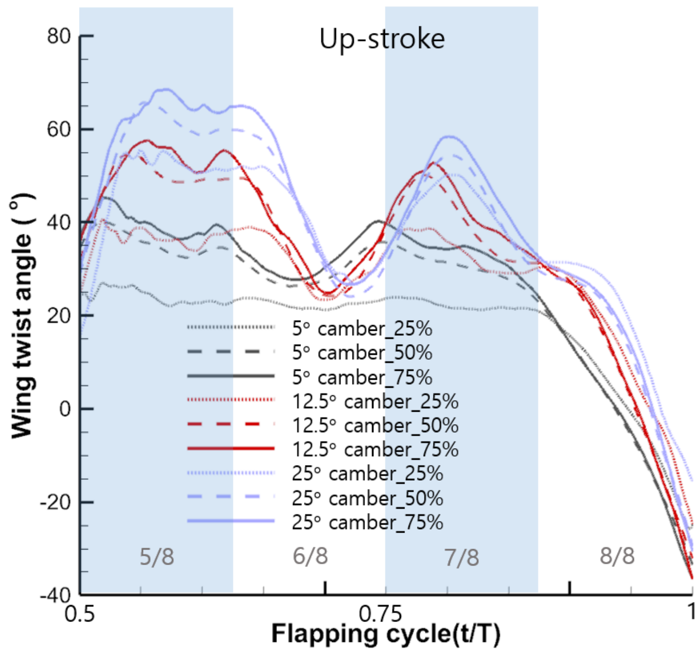


(d) Comparison of the twist angle.

Figure 5.24: Comparison at the middle of the second phase (t/T = 0.69): Chordwise pressure distribution and twist angle during half stroke.

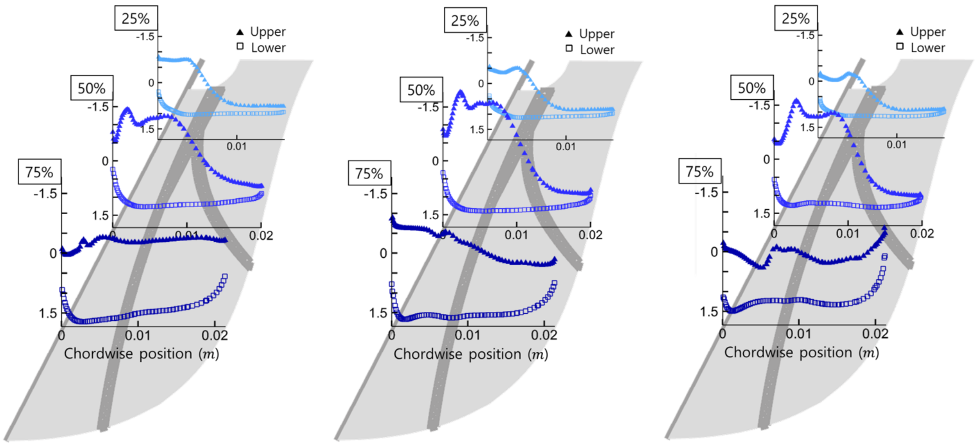


(a) 5 ° cambered wing. (b) 12.5 ° cambered wing. (c) 25 ° cambered wing.

Figure 5.25: Comparison at the middle of the third phase (t/T = 0.81): Chordwise pressure distribution and cross-sectional Q-field.

phase. In particular, the TEV at the early upstroke and the LEV generated in the previous downstroke form a vortex pairing at the trailing edge, leading to higher thrust generation [24]. For this reason, the 5 ° cambered wing yields a low-pressure distribution on the upper surface

In the second phase, however, the larger the camber angle, the greater the thrust is generated. Even though the driving speed is increasing and maximized at the end of this phase, higher camber angle delays pronation and maintains supination. As shown in Fig. 5.24, both 12.5 ° and 25 ° cambered wings produce a large pressure difference due to a large vortex attachment area. Furthermore, as shown in Fig. 5.24d, the supination time is extended up to 0.73 t/T in the 25 ° cambered wing to generate strong LEVs and a larger thrust. As a result, a strong LEV is produced in the case of larger cambered wing.

During the third phase, the LEVs generated at the previous phase expand the attachment area to the maximum, which is affected by the driving speed

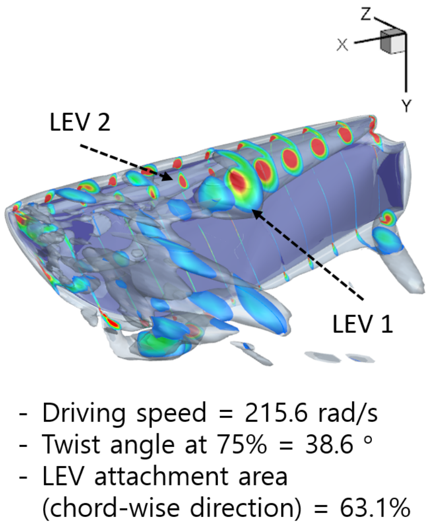


(a) 5 ° cambered wing.

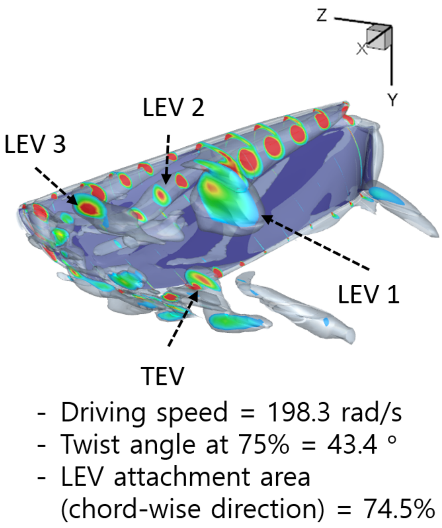


(b) 12.5 ° cambered wing.

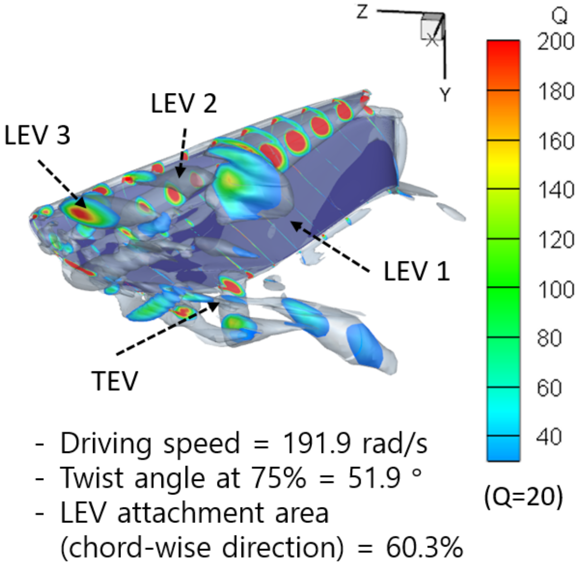


(c) 25 ° cambered wing.

Figure 5.26: Comparison at the middle of the third phase (t/T = 0.81): Chord-wise pressure distribution and cross-sectional Q-field.

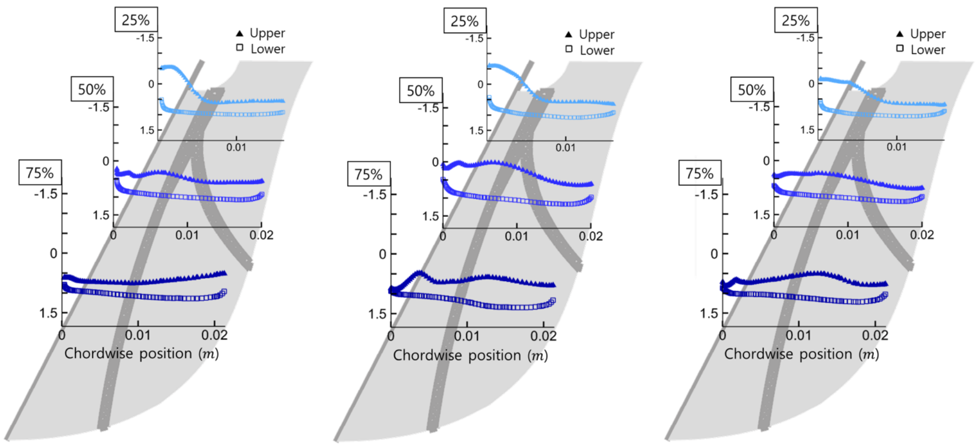


(a) 5 ° cambered wing. (b) 12.5 ° cambered wing. (c) 25 ° cambered wing.

Figure 5.27: Comparison at the middle of the fourth phase (t/T = 0.94): Chordwise pressure distribution.

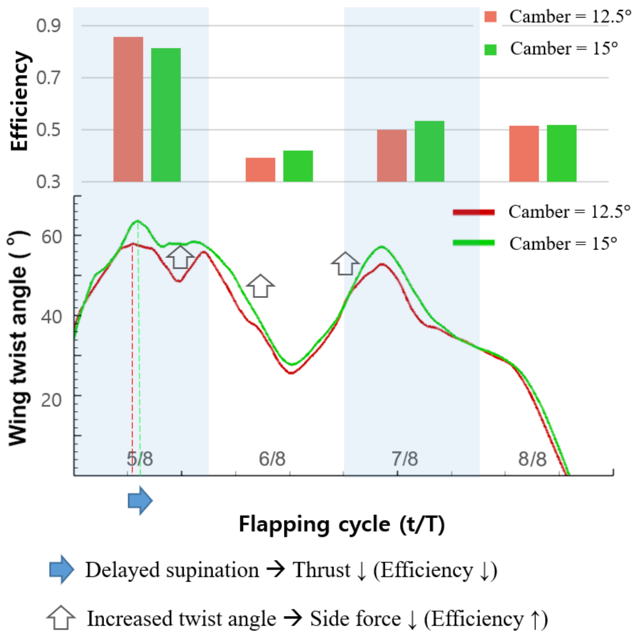


Figure 5.28: Comparison of the twist angle and propulsive efficiency of 15 ° and 7.5 ° cambered wings at 24 Hz.

and the twist angle at each thrust peak. Small camber angle yields a higher driving speed at the thrust peak, which increases the vortex intensity (Fig. 5.26a). On the other hand, large camber angle induces a larger twist angle, which is advantageous to expanding the attached LEVs (Fig. 5.26c). Thus, the vortex attachment area becomes largest at the 12.5 ° cambered wing owing to the higher driving speed and the larger twist angle (Fig. 5.26b). For this reason, the 12.5 ° cambered wing shows the largest pressure difference among the three wings (Fig. 5.26).

In the fourth phase, the larger the camber angle, the greater the thrust is generated again. Since the pressure distribution is more or less the same in the fourth phase (Fig. 5.27), the net force vector induced by the twist angle determines the major difference in thrust generation. For this reason, the 25 ° cambered wing generates the largest twist angle (Fig. 5.24d), resulting in the largest thrust generation (Fig. 5.22a).

The reason why the propulsive efficiency is higher at 15 ° than at 12.5 ° becomes evident by comparing the twist angle (Fig. 5.28). At the beginning of the stroke, supination is further delayed in the 15 ° cambered wing, and thus the propulsive efficiency is slightly lowered by the thrust reduction. In the middle of the stroke, however, the increase in the twist angle causes the net force vector to be more aligned in the thrust direction, which reduces the side force and the power consumption. As a result, the propulsive efficiency imrpoves in the case of the 15 ° cambered wing.

In summary, the largest thrust occurs at 12.5 °, resulting in a 9 % increase in thrust generation, while the highest propulsive efficiency occurs at 15 °, yielding a 14 % increase in propulsive efficiency. The supination timing and the magnitude of the twist angle, which varies with the camber angle, play an important role in determining the vortex attachment area and the net force vector in the

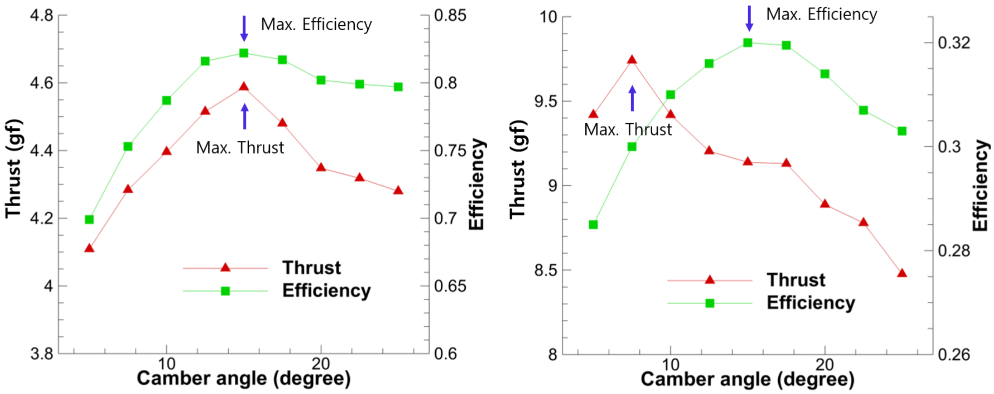


(a) 20 Hz. (b) 28 Hz.

Figure 5.29: Variations of the thrust and the propulsive efficiency at two different frequencies.

thrust direction. Thus, the camber angle significantly affects the aerodynamic performance of FW-MAVs by changing the timing and the magnitude of the passive twisting motion.

### 5.6.1 Effect of Frequency Sweep

To investigate the effect of the flapping frequency on the camber angle, an additional parametric study is performed at the frequencies of 20 Hz and 28 Hz, which is the flapping frequency within the operating range of the FW-MAV (Fig. 5.29). At 20 Hz, both the largest thrust and the highest propulsive efficiency occur at a camber angle of 15 °. On the other hand, at 28 Hz, the largest thrust moves to the camber angle of 7.5 ° while the highest propulsive efficiency still occurs at a camber angle of 15 °.

At the twist angle graph of the 15 ° cambered wing (Fig. 5.30a), as the frequency increases, the pronation and supination timing are delayed and the

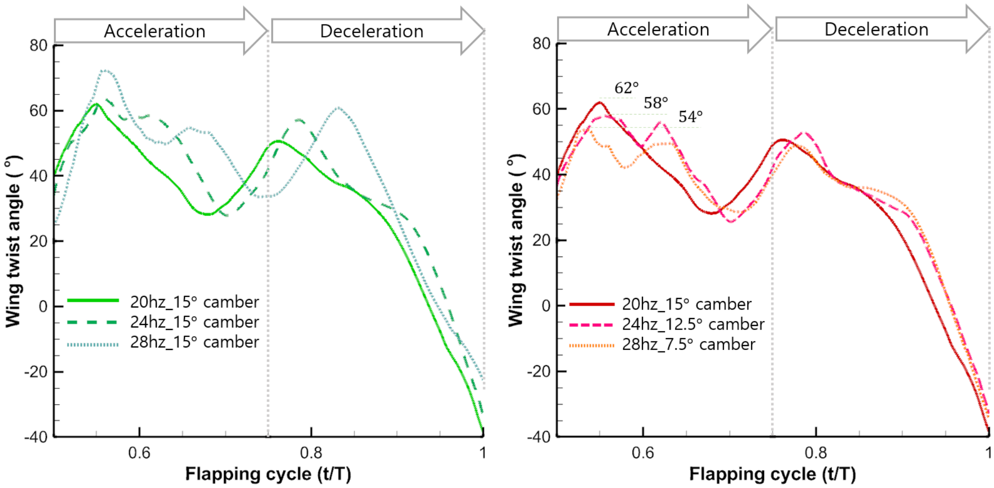


(a) Twist angle change of the 15 ° cambered wing.

(b) Twist angle producing the largest thrust.

Figure 5.30: Comparison of the twist angle in terms of frequency.

twist angle magnitude increases overall, resulting in different aerodynamic performance.

To observe the thrust performance at each frequency, the cambered wing generating the largest thrust (15 ° at 20 Hz, 7.5 ° at 28 Hz) is compared with those of the maximum and minimum camber angles, respectively (Fig. 5.33). As in the case of 24 Hz (Section 5.6), overall aerodynamic trends according to the camber angle are similar during the four phases. However, quantitative difference at a certain phase is sufficient to change the thrust performance (Fig. 5.33).

Comparing the thrust at 20 Hz, there is a noticeable difference in the third phase (Figs. 5.32a, 5.33a). Because of the large twist angle and the start of supination during the high driving speed, the 15 ° cambered wing yields a larger vortex attachment area (Fig. 5.31a, Fig. 5.34). On the other hand, at 28 Hz,

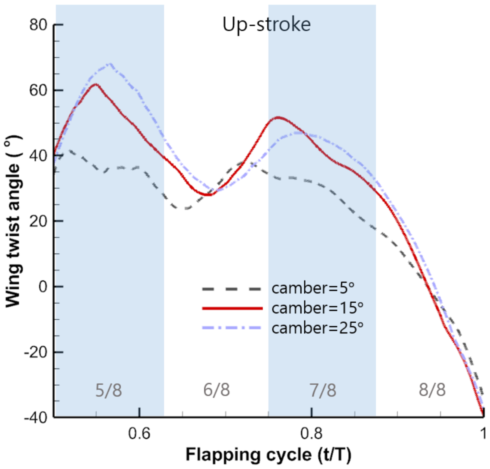


(a) Twist angle at 20 Hz.

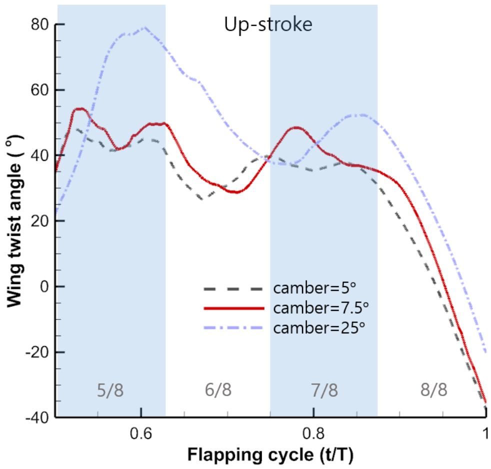


(b) Twist angle at 28 Hz.

Figure 5.31: Comparison of the twist angle in terms of frequency.

change in the behavior of the twist angle in the first phase greatly affects overall thrust performance (Figs. 5.32b, 5.33b). Due to the delayed supination timing in higher frequency, a small camber angle is advantageous to the generation of LEV in the first phase by supination (Fig. 5.31b).

Meanwhile, the cambered wings with the largest thrust at each frequency appear to have a similar pronation and supination timing, but at high frequencies, the wings quickly become tense and the twist angle magnitude is reduced (Fig. 5.30b). Figure 5.35 compares the propulsive efficiency, at 28 Hz, of the two cambered wings that produce the largest thrust and the highest propulsive efficiency. Similar to the case of 24 Hz (Section 5.6), the wing with the highest propulsive efficiency (15 °) has a greater reduction in the power consumption than in the thrust. However, at 28 Hz, since the twist angle amplitude of the wing with the largest thrust (7.5 °) is small, the power consumption is relatively increased and the propulsive efficiency is lowered.

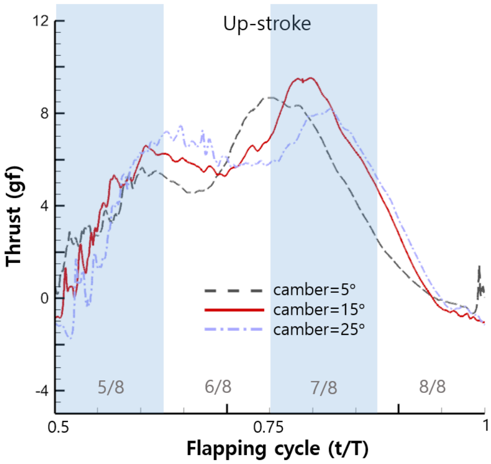


(a) Thrust variation over time at 20 Hz.

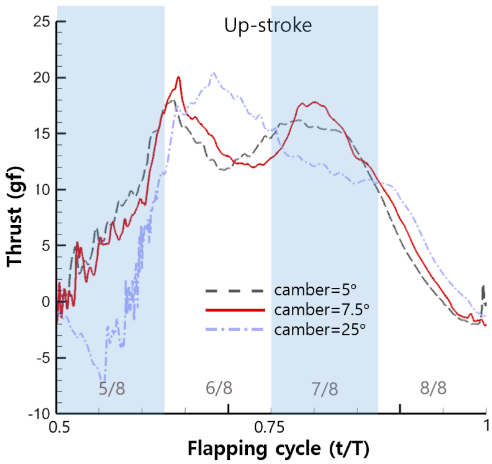


(b) Thrust variation over time at 28 Hz.

Figure 5.32: Comparison of sectional thrust performance.

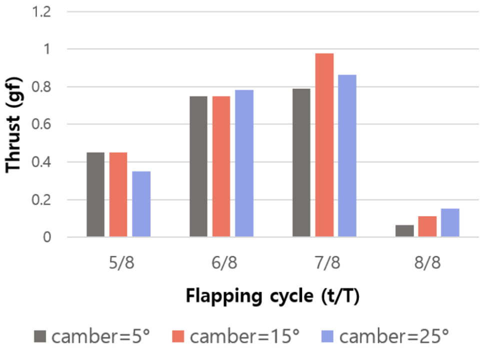


(a) Thrust performance in four phases at 20 Hz.

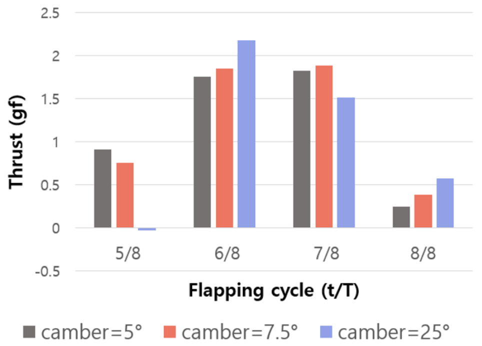


(b) Thrust performance in four phases at 28 Hz.

Figure 5.33: Comparison of sectional thrust performance.

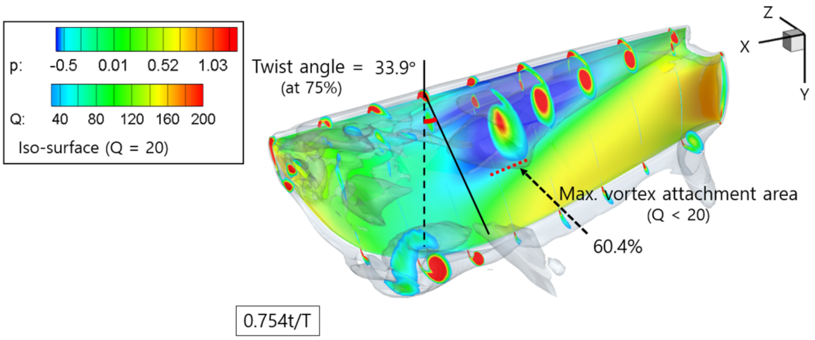


(a) 5 ° cambered wing.

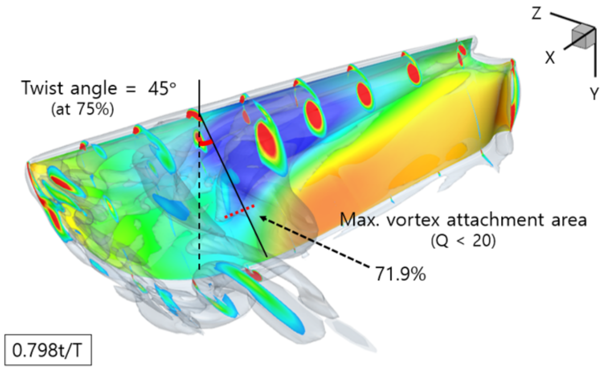


(b) 15 ° cambered wing.

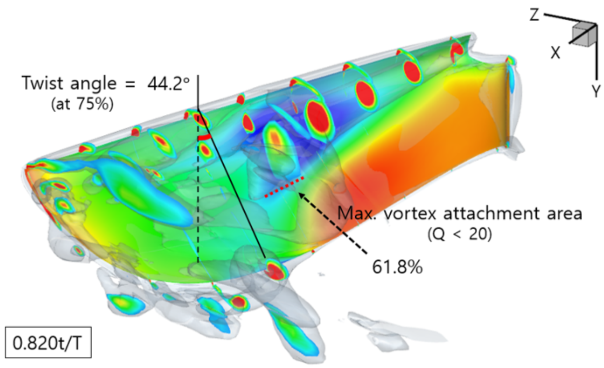


(c) 25 ° cambered wing.

Figure 5.34: Vortex structure of cambered wings at each thrust peak (20 Hz).

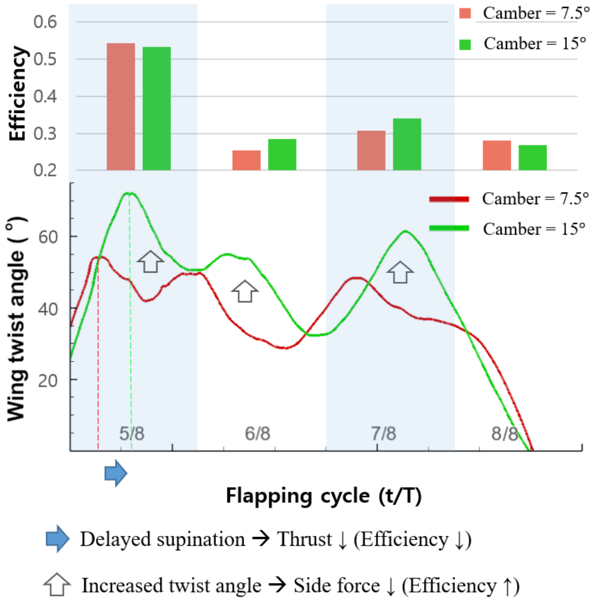


Figure 5.35: Comparison of the twist angle and the propulsive efficiency of 15 ° and 7.5 ° cambered wings at 28 Hz.

In summary, at the other two frequencies (20 Hz and 28 Hz), overall aerodynamic trends according to the camber angle during the four phases are similar to the case of 24 Hz. However, as the aerodynamic effects in a certain phase are emphasized by the frequency change, total thrust performance changes accordingly. As the frequency increases, a small camber angle is beneficial to the generation of larger thrust by strengthening the LEV intensity and widening the LEV attachement area. On the other hand, the cambered wing with the largest thrust (7.5 °) increases the power consumption at the high frequency (28 Hz) due to a small twist angle, and eventually reduces the propulsive efficiency.

Consequently, a similar twist angle trajectory is derived, in which the wing with the highest thrust at each frequency is associated with the largest LEV. In contrast, the camber angle that generates maximum propulsive efficiency comes from a 15 degree camber wing that does not fluctuate additionally in twist angle. This results in an efficient result since the net force vector of the attached LEV is directed in the thrust direction.

## 5.7 Effect of Elastic Modulus

The material characteristics of the wings of FW-MAVs affect aerodynamic performance by changing their flexible trajectory. Most of the veins are made of carbon composite materials to handle very fast flapping frequencies. There are many options for elastic modulus in composite materials, ranging from several tens of GPa to several hundred GPa. This results in a dramatic change in trajectory as a result of their flexibility. Accordingly, a parametric analysis of the vein elastic modulus is conducted in this section.

Table 5.3: Magnification of elastic modulus (E MAG) of central vein

| E MAG | 0.2 | 0.6 | 1 | 1.4 | 1.8 | 2.2 |
|---|---|---|---|---|---|---|
| E [GPa] | 46.6 | 139.8 | 233 | 326.2 | 419.4 | 512.6 |

### 5.7.1 Changes in Central Vein

As a reference, the elastic modulus of the leading-edge and the central vein of the present FW-MAV is taken. According to the magnification, the elastic modulus is calculated from the multiplied value and shown in Table 5.3. On the basis of the changes in elastic modulus of the veins, Fig. 5.36 shows a pattern of thrust and propulsive efficiency. When the elastic modulus is magnified by 1.8, maximum thrust and propulsive efficiency are observed. Figure 5.37 illustrates the thrust and side force over time. Figure 5.37 shows the thrust and side force over time. Comparison of the three points at which the minimum thrust (0.2E), the maximum thrust (1.8E), and the point at which the maximum thrust decreases again after the maximum thrust occurs (2.2E) is made with the baseline wing (1E), as well as the twist angle.

On the macroscopic scale, the first thing to note is that the 0.2E wing has two maximum thrust values ($0.58t/T$, $0.78t/T$), while the other three wings (1E, 1.8E, 2.2E) all have one maximum (Fig. 5.37a). The twist angle trajectory (Fig. 5.38) shows additional pronation and supination. A delayed movement in the previous stroke causes the wing's elasticity to generate vibrations as it rotates rapidly. In the end, the decrease in elastic modulus (0.2E) results in a thrust loss accompanied by detached vortices in the acceleration section (Fig. 5.39). Because of this, the twist angle vibrates in the acceleration section, negatively affecting thrust generation. In the three wings (1E, 1.8E, 2.2E) that

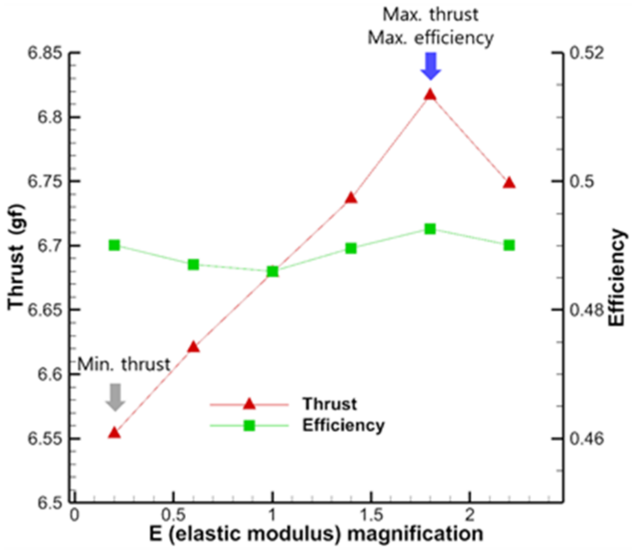


Figure 5.36: Aerodynamic performance according to the elastic modulus of central vein.

do not experience torsional vibrations, pronation and supination occur almost simultaneously. On the other hand, the 1.8E wing has a large vortex attachment area and, thus, generates the largest thrust (Table 5.4). The 1.8E wing generated the maximum thrust at maximum driving speed because it had the largest twist angle. However, when the elastic modulus of the reference wing is lower, the twist angle oscillates. Supination and pronation will be delayed as a result of this change. It resulted in a negative effect on thrust. Although the twist angle oscillated, the wing's overall twist angle increased, confirming the increased propulsive efficiency. Therefore, the 1.8E wing generated 4% more thrust than the minimum case.

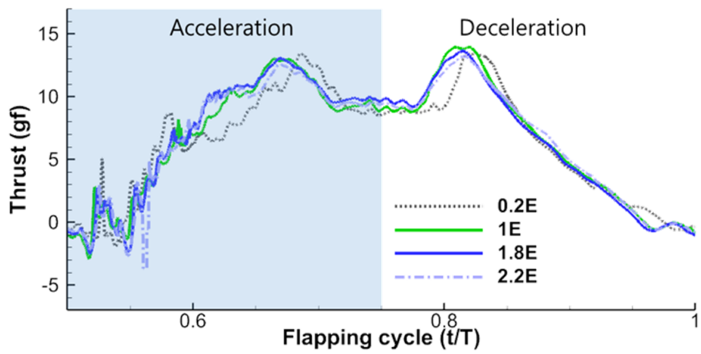


(a) Thrust variation over time.

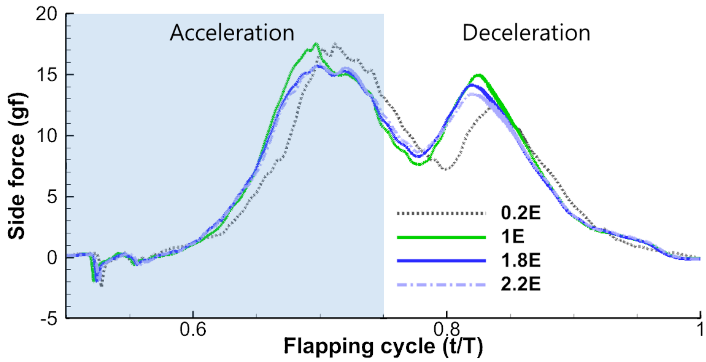


(b) Side force variation over time.

Figure 5.37: Comparison of aerodynamic performance.

Table 5.4: Maximum vortex attachment area ($Q > 20$).

| E MAG | 0.2 | 0.6 | 1 | 1.4 | 1.8 | 2.2 |
|---|---|---|---|---|---|---|
| $t/T$ | 0.825 | 0.816 | 0.809 | 0.815 | 0.815 | 0.816 |
| Chordwise area (%) | 65.5 | 67.2 | 71.1 | 73.1 | 74.8 | 73.3 |

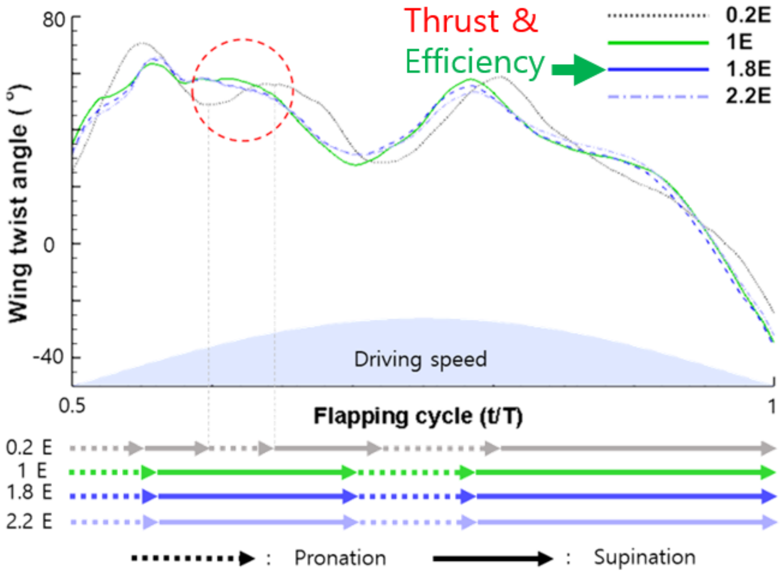


Figure 5.38: Comparison of twist angle.

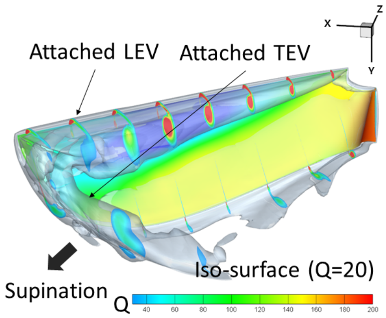


(a) 1E wing (baseline).

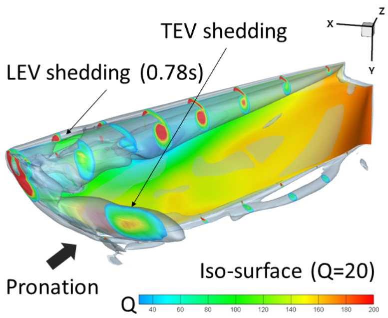


(b) 0.2E wing.

Figure 5.39: Comparison of aerodynamic performance.

### 5.7.2 Changes in Leading-Edge Vein

The change in aerodynamic performance is observed in the wide range of elastic modulus. The aerodynamic performance is compared as the elastic modulus is changed from 0.005 times to 10 times (Table 5.5). According to the change in the elastic modulus of the leading-edge, the thrust and propulsive efficiency patterns are shown in Fig. 5.40. As the elasticitic modulus increased, thrust and propulsive efficiency decreased as compared to the baseline wing. Maximum thrust is revealed by 0.005E magnification, lowest elastic modulus magnification, and maximum propulsive efficiency is revealed by 0.1E magnification. Figure 5.41 shows thrust and side force according to time. In the wing higher than the baseline wing (1E), the elastic deformation of the leading-edge (5E, 10E) hardly occurs, and low thrust and propulsive efficiency occur. The point at which the maximum thrust occurs (0.005E), the point at which the maximum propulsive efficiency occurs (0.1E), and the point at which it decreases again before and after the maximum propulsive efficiency occurs (0.05E, 0.5E) are compared with the baseline wing (1E). In Fig. 5.42, the twist angle behavior of the wing is used to analyze the cause of the problem. According to Table 5.6, the smaller the elastic modulus of the leading-edge, the larger the flapping angle. By generating a stronger vortex at a faster wing tip speed than the drive speed, this generates high thrust. By deforming the leading-edge of the cambered wing, the torsional restraint in the wing is relieved. This leads to a large twist angle as shown in Fig. 5.42. In the wing 0.5E and 0.1E, which are lower than the baseline wing, the magnitude of the twist angle increases. The 0.005E wing, however, creates additional pronation and supination by generating vibration of the twist angle. During wing acceleration, pressure and inertia act oppositely, creating a rather small twist angle. Thus, when the modulus of elas-

Table 5.5: Magnification of elastic modulus (E MAG) of leading-edge vein

| E MAG | 0.005 | 0.01 | 0.05 | 0.1 | 0.5 | 1 | 5 | 10 |
|---|---|---|---|---|---|---|---|---|
| E [GPa] | 0.55 | 1.1 | 5.5 | 11 | 55 | 110 | 550 | 1100 |

Table 5.6: Flapping angle measured at the wing tip.

| E MAG | 0.005 | 0.01 | 0.05 | 0.1 | 0.5 | 1 | 5 | 10 |
|---|---|---|---|---|---|---|---|---|
| Flapping angle [°] | 104 | 102 | 98 | 94 | 86 | 85 | 83 | 82 |

ticity is lower than 1E, flapping angles and twisting angles are generally high. Due to the high tip speed created by a large flapping angle, a large flapping angle generates a strong vortex, improving thrust. By adding a large twist angle, the vortex attachment area is expanded as well as a force vector is formed in the thrust direction, which improves propulsive efficiency. The propulsive efficiency is greatly reduced, however, if a wing has a very low modulus of elasticity. Since the twist angle is small, the timing of the supination is delayed. Ultimately, the 0.1E wing, which had the maximum propulsive efficiency, showed a 15% thrust improvement and a 6% propulsive efficiency improvement. A significant improvement in thrust and propulsive efficiency can be achieved by changing the elastic modulus of the leading-edge and central vein. Therefore, a change in elastic modulus impacts the trajectory of the twist angle of the wing, resulting in an increase in the FW-MAV's aerodynamic performance.

The effect of elastic modulus on aerodynamic performance is confirmed in this section. In view of the wide range of elastic modulus for composites, a parametric study is carried out over a very wide range of elastic modulus. The elastic modulus of the central vein greatly affects twist angle behavior. To

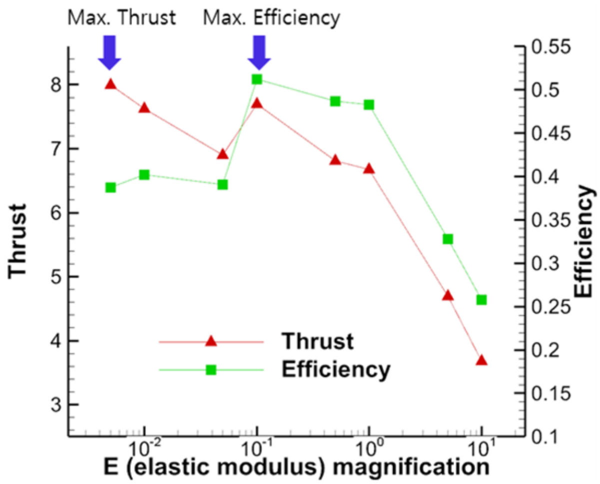


Figure 5.40: Aerodynamic performance according to the elastic modulus of vein.

avoid reducing the amplitude of the twist angle by its fluctuation, it is necessary to have a relatively high modulus of elasticity. Leading-edge vein modulus of elasticity greatly affects flapping angle as well as twist angle. Because of this, a relatively low elastic modulus has a positive effect on LEV strength and LEV attachment. Considering this range of elastic modulus for carbon composites applied to FW-MAVs, leading-edge veins can produce high thrust and efficiency when materials with a low modulus of elasticity are used and middle veins can generate a high modulus of elasticity.

## 5.8 Effect of Structural Dynamic Characteristics on Thickness Change

In the presence of complex geometrical properties and various materials, various structural properties play a very significant role in the aerodynamic characteristics of an anisotropic camber wing. In order to analyze the qualitative tendency of the complex interaction effect of structural properties, a parametric analy-

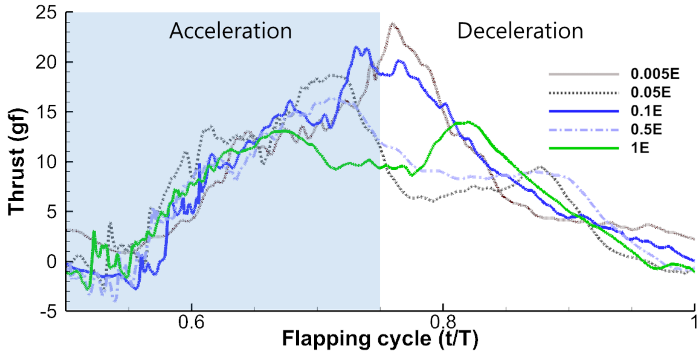


(a) Thrust variation over time.

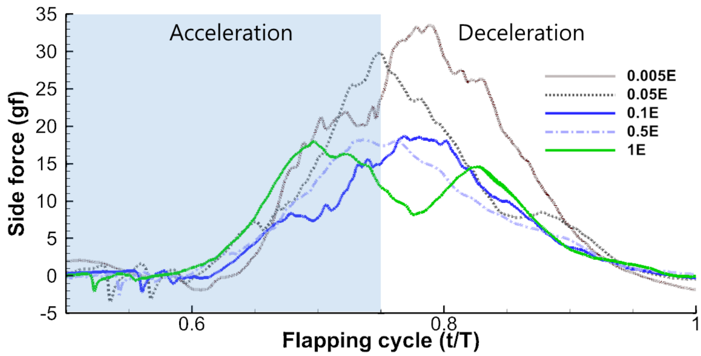


(b) Side force variation over time.

Figure 5.41: Comparison of aerodynamic performance.

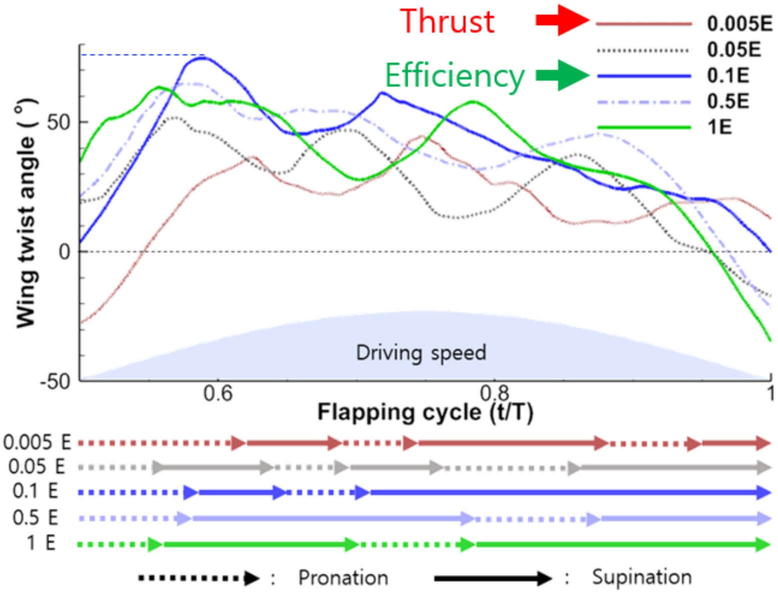


Figure 5.42: Comparison of twist angle.

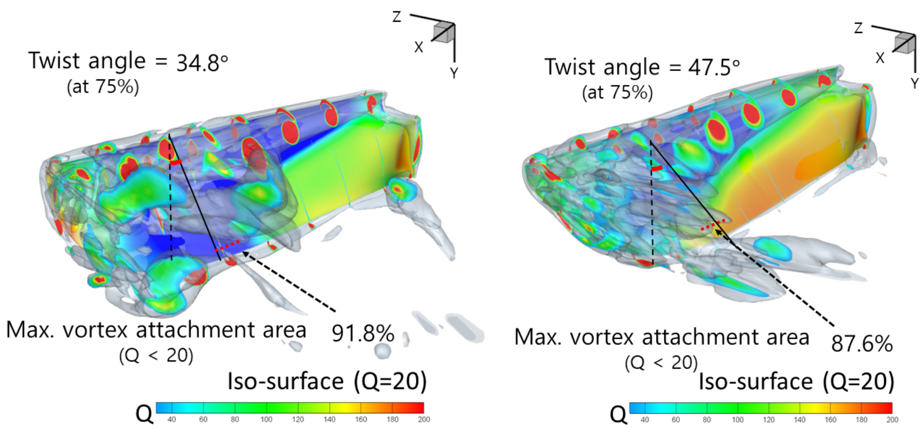


(a) 1E wing (baseline).

(b) 0.2E wing.

Figure 5.43: Comparison of vortex on the wing.

Table 5.7: Magnification of thickness of central vein

| Thickness MAG | 0.5 | 0.75 | 1 | 1.25 | 1.5 |
|---|---|---|---|---|---|
| Thickness [mm] | 0.1250 | 0.1875 | 0.2500 | 0.3125 | 0.3750 |

sis based on structural dynamic characteristics (natural frequency and mode shape along the direction) is conducted to suggest a direction for cambered wing design that results in excellent aerodynamic performance. In this section, parametric analysis is performed by adjusting the thickness of the leading-edge vein and central vein in order to significantly change the structural dynamic characteristics.

### 5.8.1 Changes in Central Vein

To examine structural dynamic characteristics, the thickness of the central vein is changed from 0.5 to 1.5 magnification in comparison to the baseline wing (Table 5.7. Figure 5.44 shows the parametric results of thrust and propulsive efficiency for these thickness changes. Maximum thrust is obtained from the baseline wing, and maximum propulsive efficiency is obtained from the thinnest wing (0.5T).

Considering the changes in the structural dynamic characteristics (natural frequency, mode shape) for the change in central vein thickness, Fig. 5.50a shows the natural frequency in each chordwise and spanwise direction, and Fig. 5.51 shows the mode shape in each direction. The natural frequency of the 2$^{nd}$ bending mode in chordwise and spanwise direction tends to decrease as the central vein thins. In addition, the coupling characteristics of bending and torsion appear dominant (bending-torsion coupling characteristics; torsion variation of mode shape in bending mode or bending variation of mode shape in torsion mode) as the central vein thins.

According to the thinning of the central vein, three major phenomena appear, which have a huge impact on thrust and propulsive efficiency.

1. Inertia reduction delays stroke reversal $\rightarrow$ delayed supination.
2. Reduces natural frequencies of the $2^{\text{nd}}$ bending mode (degradation of bending stiffness) $\rightarrow$ increasing the twist angle.
3. Bending-torsion coupling characteristics are dominant $\rightarrow$ reduced fluctuation increases twist angle amplitude.

First, the inertia of the wing is reduced. This delays supination by delaying stroke reversal, resulting in delayed LEV generation (Fig. 5.45). Secondly, a decrease in natural frequency leads to an increase in twist angle due to degradation of bending stiffness (Fig. 5.45). It has a positive effect on the attachment of wider LEVs. The third result is that as the bending-torsion coupling characteristics become dominant, the amplitude of the twist angle increases as the fluctuation of the twist angle decreases (Fig. 5.45). Thus, as shown in Fig. 5.46, the largest thrust is found at the baseline wing based on the combined characteristics of the first and second features (decreased inertia force and natural frequency). Meanwhile, the third feature (weak bending-torsion coupling characteristics) reduces the fluctuation of twist angle, which leads to the largest propulsive efficiency being generated from the thinnest 0.5T wing (Figs 5.45, 5.46).

### 5.8.2 Changes in Leading-Edge Vein

To examine structural dynamics based on the thickness change of the leading-edge vein, its thickness is changed from 0.75 to 1.5 magnification compared

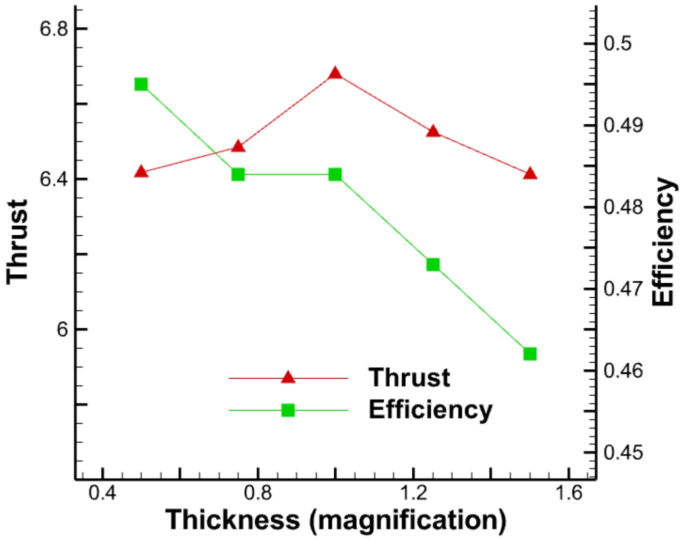


Figure 5.44: Aerodynamic performance according to central vein thickness.

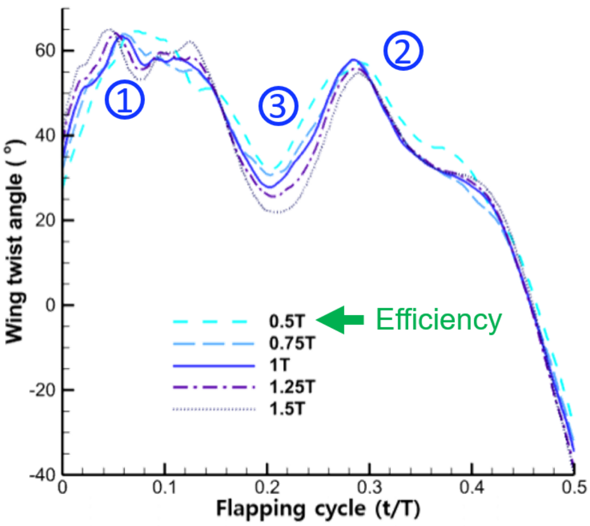


Figure 5.45: Trends in twist angles according to central vein thickness.

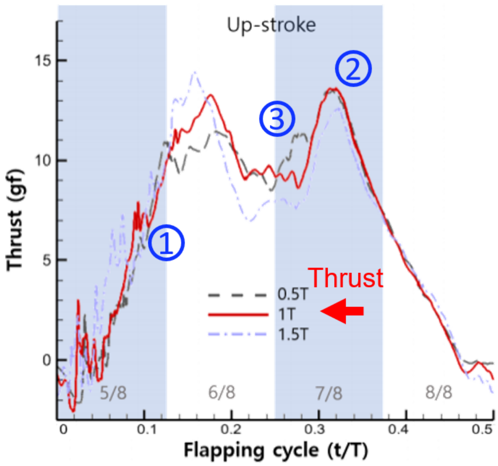


(a) Thrust.

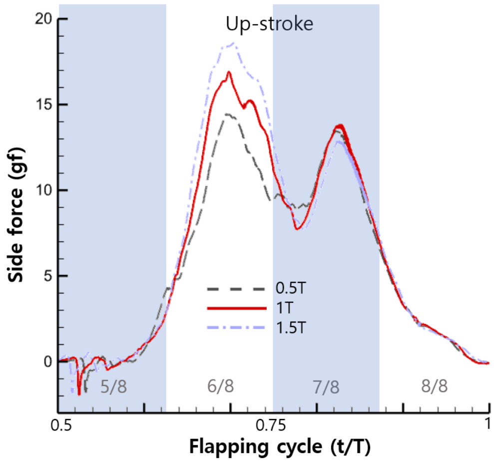


(b) Side force.

Figure 5.46: Comparison of aerodynamic performance.

Table 5.8: Magnification of thickness of leading-edge vein

| Thickness MAG | 0.75 | 1 | 1.25 | 1.5 |
|---|---|---|---|---|
| Thickness [mm] | 0.7125 | 0.9500 | 1.1875 | 1.4250 |

to the baseline wing (Table 5.8). Figure 5.44 shows the parametric results of thrust and propulsive efficiency for these thickness changes. Maximum thrust is obtained from the baseline wing, and maximum propulsive efficiency is obtained from the 1.25T wing.

Considering the changes in the structural dynamic characteristics (natural frequency, mode shape) for the change in leading-edge vein thickness, Fig. 5.50b shows the natural frequency in each chordwise and spanwise direction, and Fig. 5.52 shows the mode shape in each direction. A decrease in natural frequency is observed in all directions as the thickness of the leading-edge vein becomes thinner. This means that the leading-edge vein is crucial to wing stiffness. The bending-torsion coupling characteristics are weak according to the thinning of the leading-edge vein (bending-torsion coupling characteristics; torsion variation of mode shape in bending mode or bending variation of mode shape in torsion mode).

According to the thinning of the leading-edge vein, three major phenomena appear, which have a huge impact on thrust and propulsive efficiency.

1. Inertia reduction delays stroke reversal → delayed supination.

2. Reduces natural frequencies of the 1$^{st}$ & 2$^{nd}$ mode (degradation of bending stiffness) → increasing the flapping angle & the twist angle.

3. Bending-torsion coupling characteristics are not dominant → increasing the twist angle fluctuation.

First, the inertia of the wing is reduced. This delays supination by delaying stroke reversal, resulting in delayed LEV generation (Fig. 5.48). Second, the natural frequencies decrease in all directions, which degrades bending and torsion stiffness. As a result, the flapping angle and twist angle increase. It is eventually possible to form wider and stronger LEV attachments. Third, since the

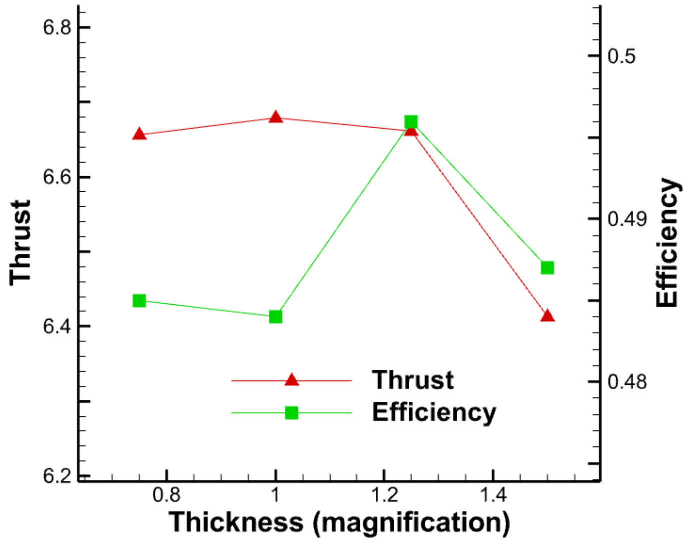


Figure 5.47: Aerodynamic performance according to leading-edge vein thickness.

bending-torsion coupling is not dominant, increasing fluctuations decrease the amplitude of the twist angle (Fig. 5.48). Thus, as shown in Fig. 5.49, the largest thrust is found at the baseline wing based on the combination of the first and second features (inertia and natural frequency reduction in all directions). In contrast, since the third feature (weak bending-torsion coupling characteristics) leads to a fluctuating twist angle, the largest propulsive efficiency is generated by thicker wings (1.25T) with less reduced twist angles and significant thrust (Figs 5.48, 5.49).

After analyzing the changes according to the thickness of the wing veins along with structural dynamics results, it is discovered that the natural frequencies of the leading-edge and central veins had a significant effect on the amplitude of flapping angle and twist angle, respectively. The bending-torsion

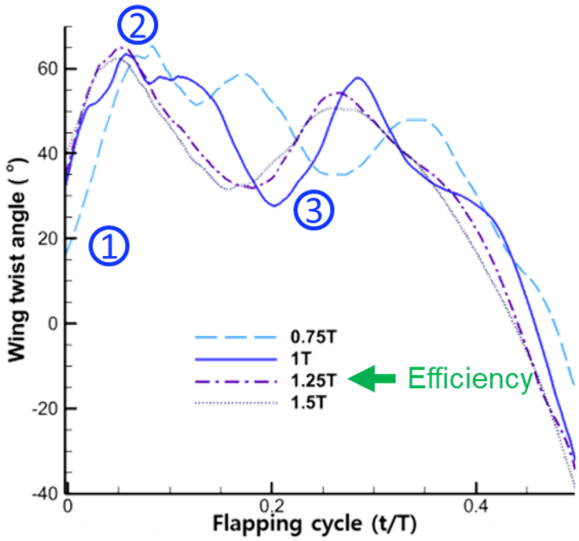


Figure 5.48: Trends in twist angles according to leading-edge vein thickness.

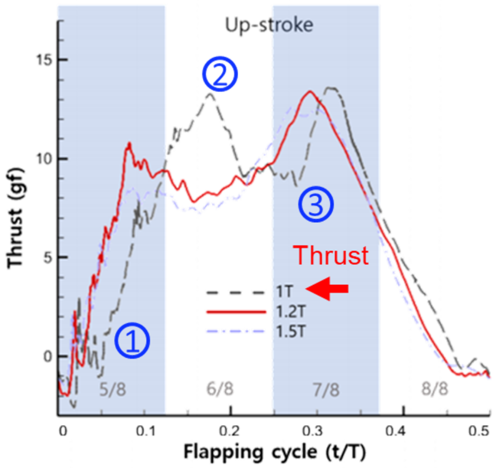


(a) Thrust.

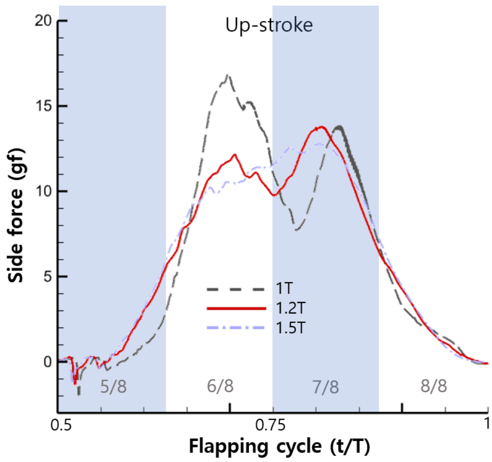


(b) Side force.

Figure 5.49: Comparison of aerodynamic performance.

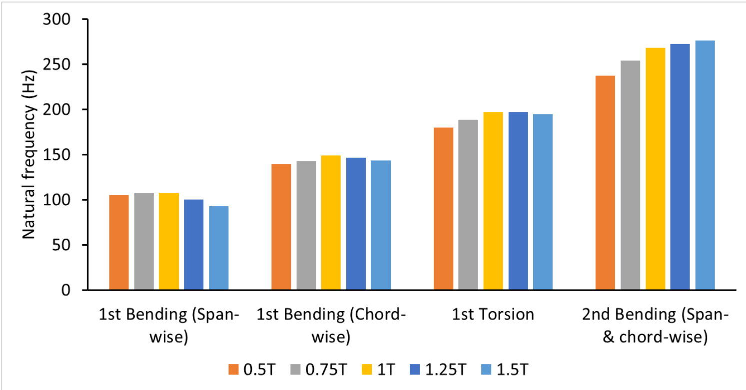


(a) Comparison according to central vein thickness.

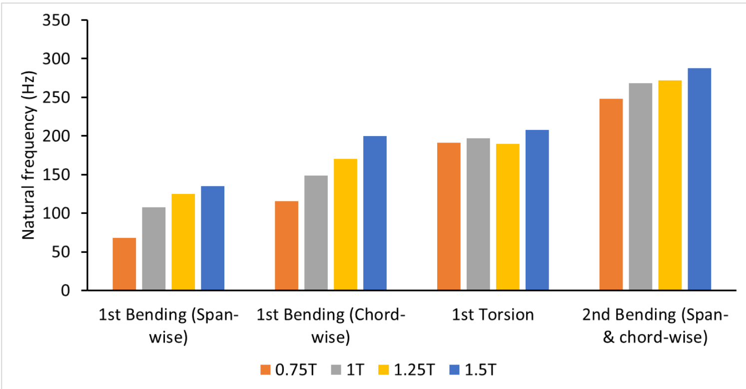


(b) Comparison according to leading-edge vein thickness.

Figure 5.50: Natural frequency according to wing vein thickness.

coupling phenomenon, however, causes a decrease in the fluctuation of the flapping trajectory and produces a more stable LEV. It is therefore important to consider the structural dynamic characteristics of the wing structure when designing a wing with high thrust and high propulsive efficiency.

The effect of changes in structural dynamics on aerodynamic performance is confirmed according to the thickness of each vein. There is a significant effect of the thickness of the central vein on the nature of the 2$^{\text{nd}}$ bending mode's natural

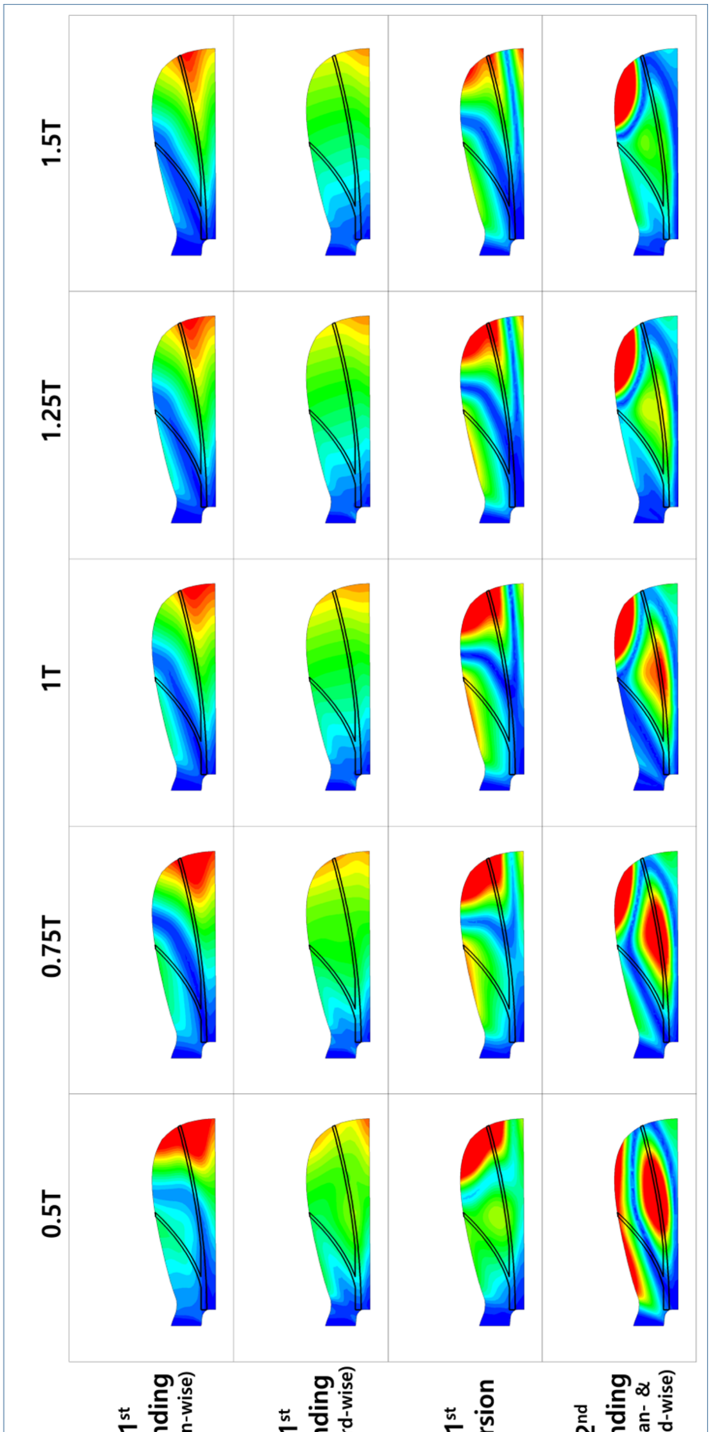


Figure 5.51: Mode shape comparison according to central vein thickness.

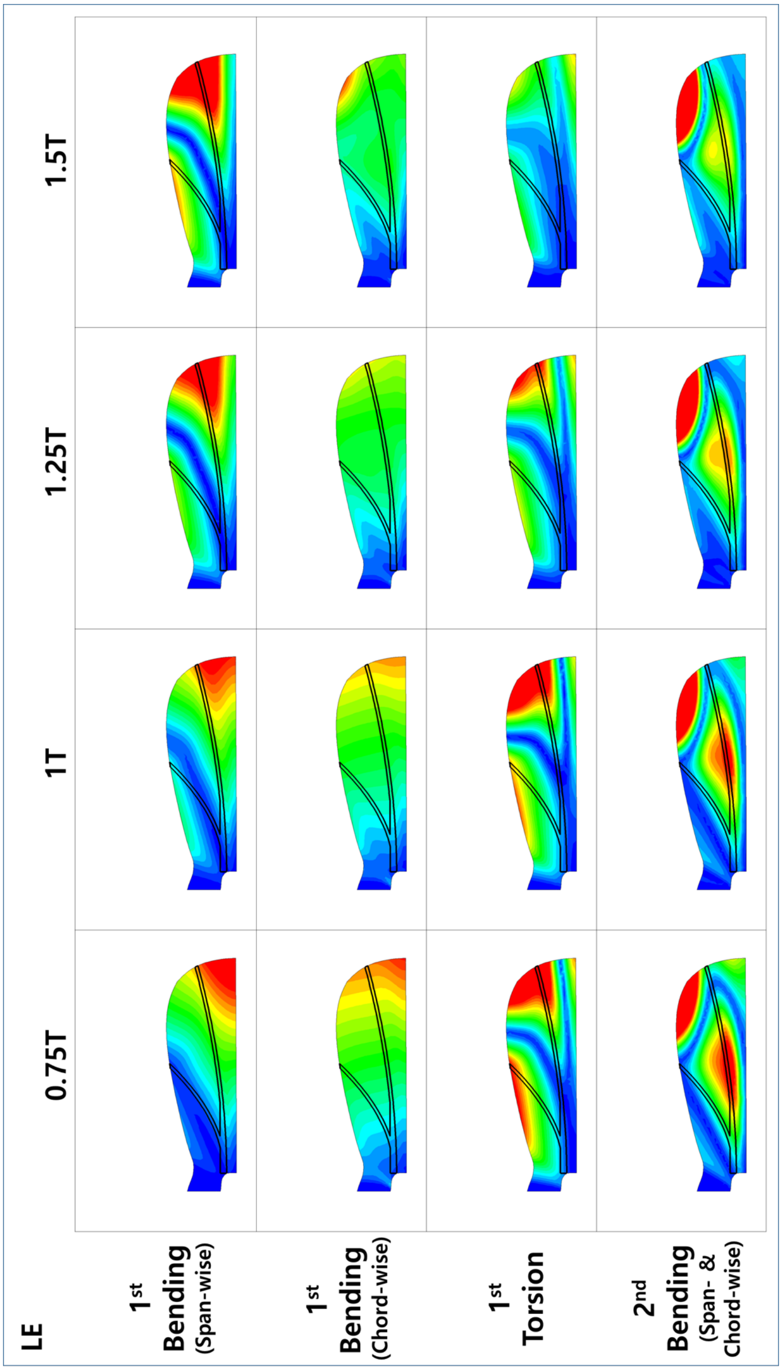


Figure 5.52: Mode shape comparison according to leading-edge vein thickness.

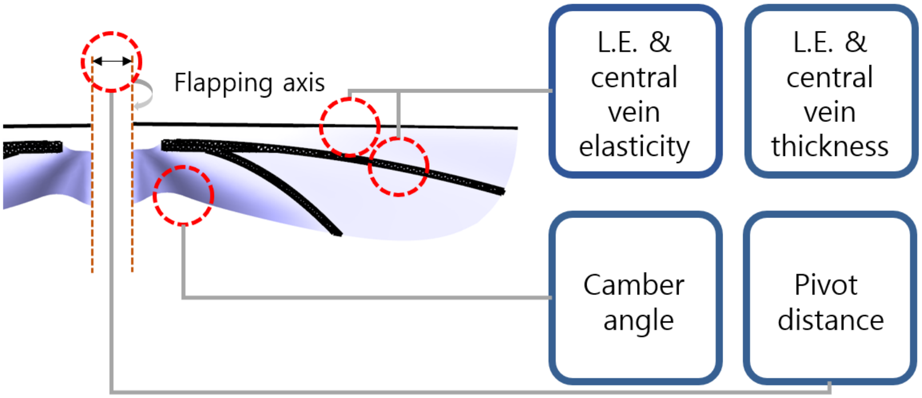


Figure 5.53: Aeroelastic parameters analyzed in this study.

frequency. And as it became thinner, the bending torsion coupling phenomenon appeared more prominently. Meanwhile, the thickness of the leading-edge vein affects both twist angles and flapping angles, since it affects the natural frequency in every direction. Thin leading-edge veins show weaker bending-torsion coupling. Consequently, it is confirmed that bending-torsion coupling has a considerable impact on propulsive efficiency. Also, the decrease in natural frequency is beneficial to thrust performance because it increases the flapping angle and twist angle of the LEV, improving its strength and attachment.

## 5.9 Designed cambered wing

Observations as a result of analyzing the parameters in Fig. 5.53 are summarized below. First, camber angle guidelines based on aerodynamic effects are presented at each operating frequency. Guidelines for elastic modulus are presented for leading-edge veins (carbon composites with low E), and central veins (carbon composites with high E). Propulsive efficiency is improved by the dominant bending-torsion coupling effect. Cambered wings with low natural frequencies can be made more efficient and thrust generating by increasing

Table 5.9: The designed wing to maximize efficiency for each parameter

| Designed wing at normal operating frequency (24 Hz) | |
|---|---|
| Camber angle | 15° |
| E of leading-edge vein | 11 Gpa |
| E of central vein | 419.4 Gpa |

flapping and twist angles. Based on these analysis results, a wing with the parameters generating maximum efficiency is designed (Table 5.9). By comparing it to a flat wing and a 15-degree cambered wing, its aerodynamic performance is assessed. The three wings (Fig. 5.54) are compared in three spanwise sections (25%, 50%, and 75%).

Based on the results of analyzing design parameters in the previous section, the twist angle is analyzed. There are four characteristics of the designed wing that are advantageous for improving aerodynamic performance. Firstly, since the flapping angle is the largest and supination occurs when the wing accelerates most rapidly, it greatly increases the vortex strength. Accordingly, Fig. 5.55a shows a substantial increase in thrust. In addition, the amplitude of the twist angle increased significantly, which is very advantageous for the net force vector being positioned in the thrust direction. Accordingly, as shown in Fisg. 5.55a, 5.55b, the side force is the smallest despite the large thrust generated. As a result, compared to a cambered wing, the twist angle fluctuation is relatively small, preventing LEV separation.

As a result of these features, in the designed wing, thrust is increased by 23.57%, and efficiency is increased by 18.11%, which is a significant improvement in aerodynamic performance (Table 5.10).

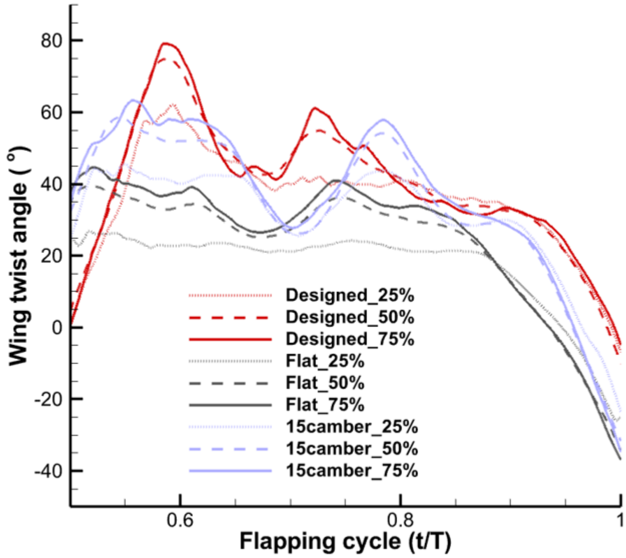


Figure 5.54: Comparison of the twist angle.

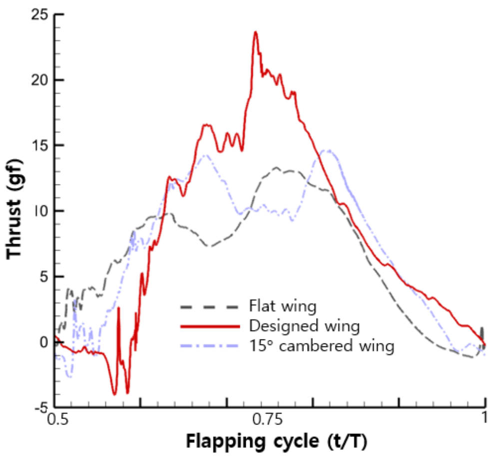


(a) Thrust variation over time.

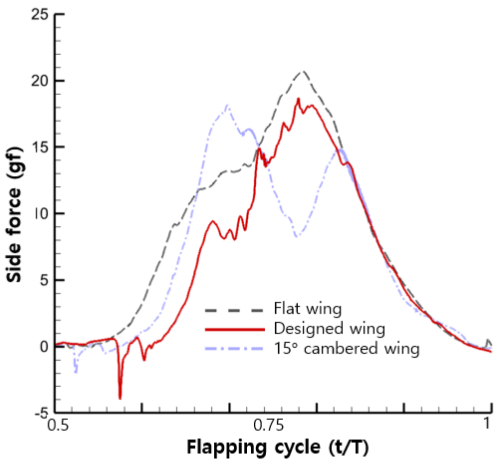


(b) Side force variation over time.

Figure 5.55: Comparison of aerodynamic performance.

Table 5.10: Comparison of averaged thrust and propulsive efficiency.

| Hovering condition | Flat wing | Cambered wing (Camber angle = 15°) | Designed wing |
|---|---|---|---|
| Averaged thrust | 6.195 | 6.679 (+7.81%) | 7.769 (+23.57%) |
| Propulsive efficiency | 0.427 | 0.486 (+13.82%) | 0.515 (+18.11%) |

# Chapter 6

# Concluding Remarks

## 6.1 Summary

This research presents a methodology for analyzing an anisotropic cambered wing composed of different materials, and the aerodynamic performance and design parameters of a FW-MAV's cambered wing are examined in detail. Here are some of these topics briefly summarized.

Fluid-structure interaction analysis programs are developed for two-dimensional and three-dimensional analysis. Through this program, two-dimensional research can simulate passive rotation of a flexible wing, as well as three-dimensional research that can realistically model fluid characteristics and structural properties. FW-MAV's cambered wing is composed of thick veins and thin membranes of different materials, which are installed in a form with a camber angle to maximize flexibility. As the wing shows large deformations and displacements, numerical methods that are capable of accurately simulating fluid-structure phenomena are applied. This developed program combines the validated solvers for each analysis module, and it is validated with experimental and analysis results for anisotropic Zimmerman wings. Cross-validation is also carried out against experimental results obtained in the present study in order to ensure an accurate analysis of cambered wings of FW-MAV. The solver can therefore be used to analyze a broad range of flexible wings including flapping vehicles, due to its ability to realistically reflect fluid, structural, and physical properties.

Torsion springs can be used to implement two-dimensional numerical modeling of the twisting motion of cambered wings. Through the torsional spring coefficient, the amplitude of passive rotation can be controlled. To control the passive rotation pattern of the wing, a parametric study is conducted on the torsional spring coefficient. An appropriate torsional spring coefficient in the cambered wing has a very significant effect on the stable generation of thrust.

Since it is difficult to directly model the torsional spring coefficient of the FW-MAV wing, three-dimensional modeling is conducted. As a result, it realistically simulates the shape and material properties of the wing, as well as the complex shape and the boundary conditions of the wing.

Three-dimensional modeling of the cambered wing includes a fluid-structure interaction analysis that simulates realistically the shape, the material properties, and the boundaries of the wing. A study is conducted on the unsteady vortex structures caused by aeroelastic phenomena around the cambered wings of FW-MAV. Also, the aeroelastic design parameters of the cambered wing are parametrically analyzed to determine if excellent aerodynamic performance can be achieved. Next, three different flapping frequencies in addition to normal operating conditions are studied parametrically. Each flapping frequency produces a different set of camber angles that produce the largest thrust and propulsive efficiency. Based on the stroke phase, their effects on aerodynamic performance are analyzed. Accordingly, the unsteady vortex structure is greatly affected by the timing and magnitude of the passive twisting motion, which are determined by the camber angle at the operating frequency. In addition, the effect of wing veins is examined. A parametric analysis of changes in elastic modulus and thickness is conducted for each leading-edge vein and central vein of the cambered wing. Thus, leading-edges and central veins determine structural mode shapes and natural frequencies, which alter twisting pattern and flapping angle changes. Furthermore, the bending torsion coupling phenomenon reduces the fluctuation in the flapping trajectory and thus contributes to excellent aerodynamic performance. By analyzing the aeroelastic design parameters, the direction of parameter selection to improve the performance of FW-MAV can be presented as follows.

- Unsteady aerodynamic force generation mechanism of FW-MAV's cambered wing is firstly analyzed.
- Camber angle guidelines based on major aerodynamic effects at each operating frequency are presented.
- Elastic modulus guidelines are presented: leading-edge vein (Carbon composite with low E), central vein (Carbon composite with high E).
- Bending-torsion coupling effect: aerodynamic efficiency increases as it becomes more dominant.
- Low natural frequencies: increased flapping and twist angles produce more thrust and are more efficient.

By selecting parameters as suggested in this study, thrust and efficiency are increased by 23.57 and 18.11, respectively, which represents significant improvements in aerodynamic performance (Table 5.10). Thus, it is expected that its design direction will result in excellent aerodynamic performance under various operating conditions.

Consequently, it is feasible to analyze fluid-structure interactions of cambered wings with realistic modeling of complex features in order to develop FW-MAVs on a practical basis. It may be possible to improve the aerodynamic performance of FW-MAVs by analyzing various aeroelastic parameters based on structural dynamic characteristics, even those that are difficult to measure experimentally.

## 6.2 Future Works

On the basis of the research conducted so far, efforts are in progress to improve FW-MAVs' flight performance. The following is a summary of several future works.

- The shape, material properties, and driving motion of a cambered wing can also affect its aeroelastic properties. Aeroelastic analysis including such parameters could improve the performance of FW-MAVs.
- The performance of flapping vehicles can be dramatically improved by a multidisciplinary approach to optimal design combined with a variety of aeroelastic parameters.
- It is possible to extend this study to include structural stress analysis as well as aerodynamic performance. The BTC coupling or natural frequency increase induces stress in the structure, so further studies can be conducted to understand this phenomenon.
- The study can also be extended to other flight conditions besides those presented in the appendix A.

- The fuselage has a negligible effect on aerodynamic performance during a hovering condition. However, in forward flight, the fuselage produces a flow in the spanwise direction that may cause a difference depending on speed. As a result, various flight conditions must be analyzed for the fuselage.

# Appendix A

# Forward flight

To identify the possibility of using FW-MAV in various flight conditions, an analysis is conducted in a forward flight condition (Fig. A.1). A forward flight test of the present FW-MAV confirmed the flight speed and pitch angle to be 30 $m/s$ and 30°), respectively. A comparison of the results of the designed wing, flat wing, and 15°) cambered wing is used to observe the changes in aerodynamic performance in the forward flight condition.

Based on the results of analyzing design parameters in the previous section, the twist angle is analyzed (Fig. A.2). There are four characteristics of the designed wing that are advantageous for improving aerodynamic performance. Firstly, since the flapping angle is the largest and supination occurs when the wing accelerates most rapidly, it greatly increases the vortex strength. Accordingly, Fig. A.3a shows a substantial increase in thrust. In addition, the amplitude of the twist angle increased significantly, which is very advantageous for the net force vector being positioned in the thrust direction. Accordingly, as shown in Figs. A.3a, A.3b, the side force is the smallest despite the large

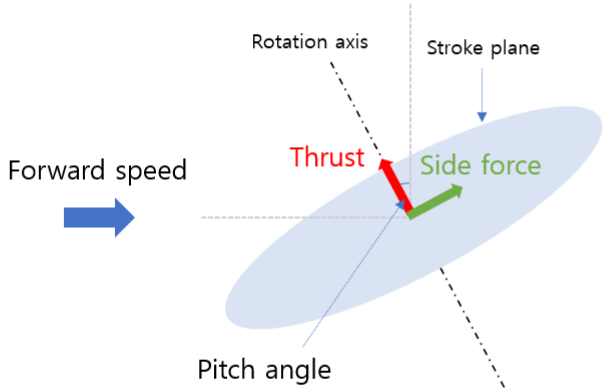


Figure A.1: Coordinate system in fowrard flight.

Table A.1: Comparison of averaged thrust and propulsive efficiency.

| Forward flight (30°, $5m/s$) | Flat wing | Cambered wing (Camber angle: 15°) | Designed wing |
|---|---|---|---|
| Averaged thrust | 5.587 | 5.485 (-1.83%) | 6.096 (+9.28%) |
| Propulsive efficiency | 0.408 | 0.445 (+9.07%) | 0.461 (+11.91%) |

thrust generated. As a result, compared to a cambered wing, the twist angle fluctuation is relatively small, preventing LEV separation.

As a result of these features, in the designed wing, thrust is increased by 9.28%, and efficiency is increased by 11.91% in the forward flight condition, which is a significant improvement in aerodynamic performance (Table A.1).

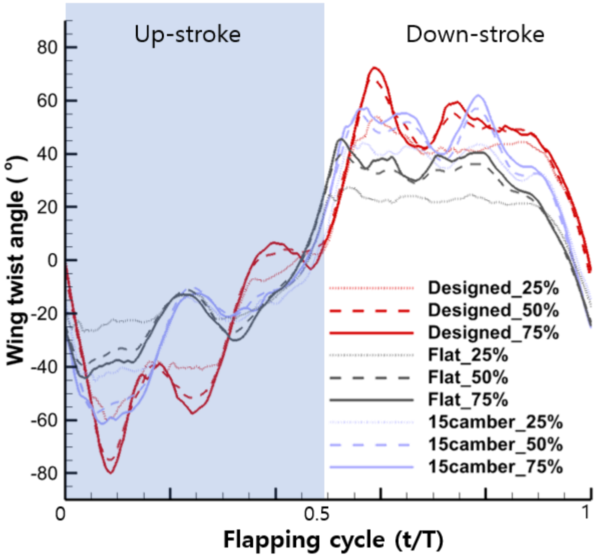


Figure A.2: Comparison of the twist angle.

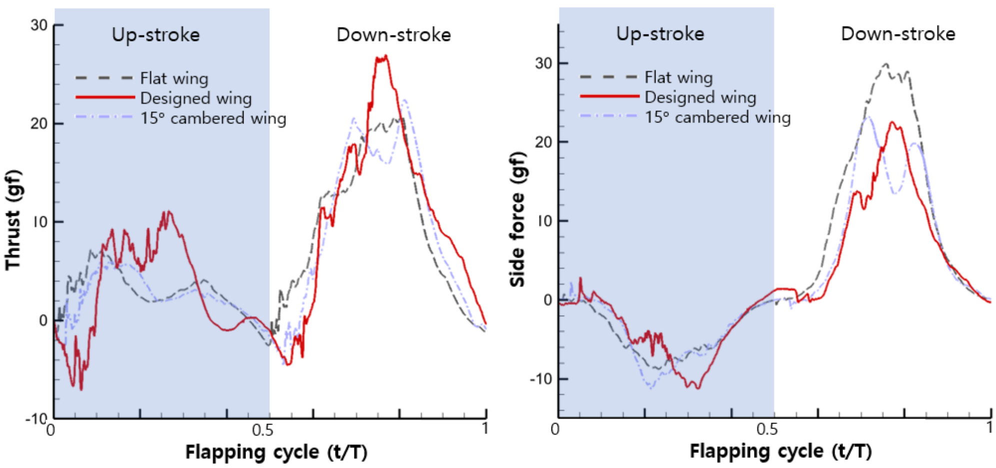


(a) Thrust variation over time.

(b) Side force variation over time.

Figure A.3: Comparison of aerodynamic performance.

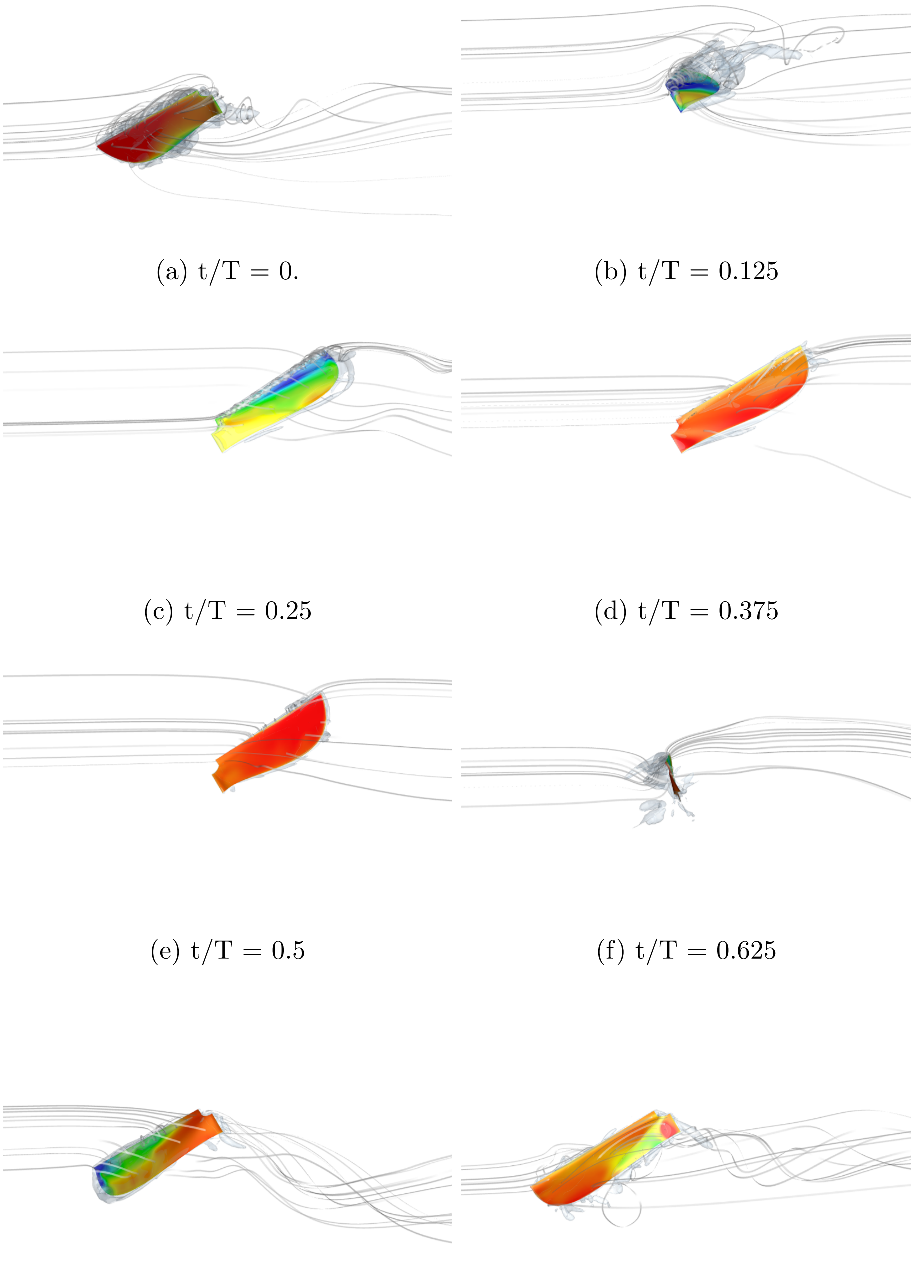

(a) t/T = 0.

(b) t/T = 0.125

(c) t/T = 0.25

(d) t/T = 0.375

(e) t/T = 0.5

(f) t/T = 0.625

(g) t/T = 0.75

(h) t/T = 0.875

Figure A.4: Aerodynamic vortex structure of the flat wing under forward flight conditions during one flapping cycle.

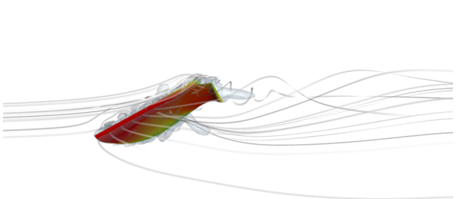

(a) t/T = 0.

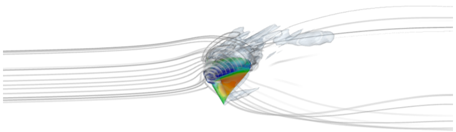

(b) t/T = 0.125

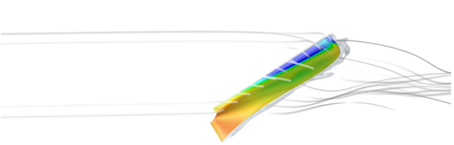

(c) t/T = 0.25

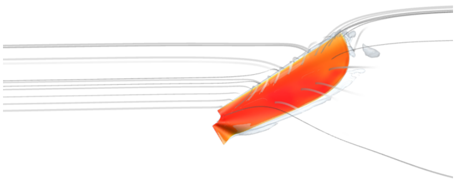

(d) t/T = 0.375

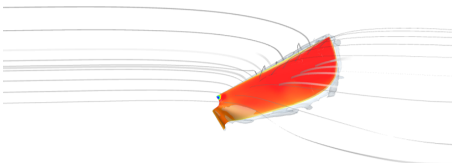

(e) t/T = 0.5

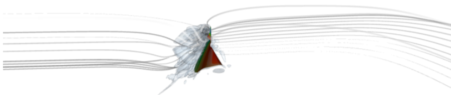

(f) t/T = 0.625

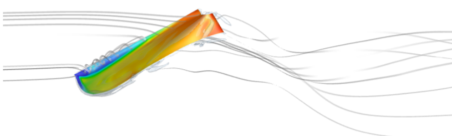

(g) t/T = 0.75

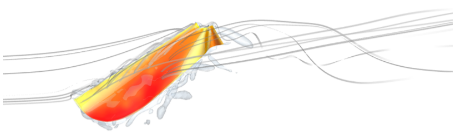

(h) t/T = 0.875

Figure A.5: Aerodynamic vortex structure of the designed wing under forward flight conditions during one flapping cycle.

# Appendix B

# Optimized wings without size constraints

In this section, a comparison is made between the wing analyzed in Chapter 5 (Type 1) and the wing designed to optimize the shape without size constraints (Type 2) through experiments. Through experiments with Lee [51], the wing of Type 2 was designed to optimize the shape without size constraints. The numerical modeling information of Type 2 is as follows: 3.55 million grid points with multi-block grid (fluid), 6335 elements with 3 materials (structure), and 1/20000 $t/T$ (time step). The computed averaged thrust converged after 5 to 7 cycles showed a good agreement with the experimental results: 1.6% error for Type 1 (19.68 $gf$) and 3.6% error for Type 2 (19.27 $gf$), respectively. Figure B.1 compares Type 1 and Type 2 numerical modeling.

Figure B.3 indicates the Q-isosurface, and pressure contours on the wing upper surfaces at three instants (0.20 $t/T$, 0.25 $t/T$, and 0.30 $t/T$), where the major vortices on the wing are strongly formed by high flapping angular velocity. The vortex structures of Type 2 (Figs. B.3a, B.3c, and B.3e) and Type

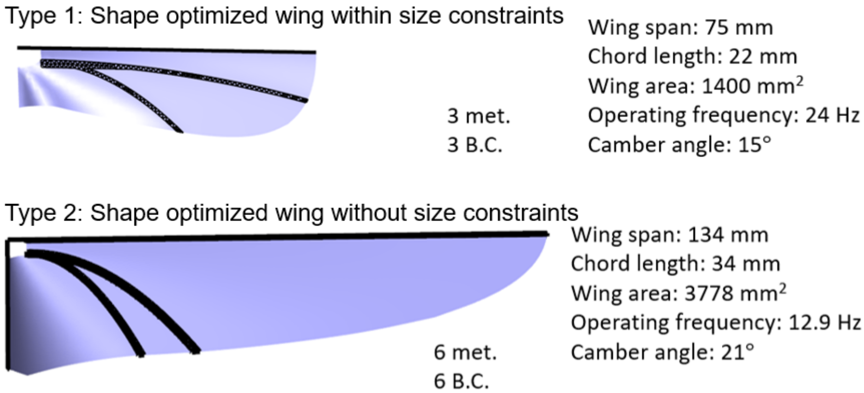


Figure B.1: Comparison of shape-optimized wing modeling with and without size constraint.

1 (figure B.3b, B.3d, and B.3f) show a noticeable difference. Type 1 vortices are strongly formed at the early stroke of the wing, but they shed significantly as pronation occurs (Figs. B.3b and B.3d). However, in Type 2 (Figs. B.3a and B.3c), the LEV and the WTV are stabilized and expanded by continuous supination during the acceleration phase. As the flapping angular velocity slows down, there is a loss of strength in the LEV of Type 1 after 0.3 t/T (Fig. B.3f). Consequently, Shape-optimized wing (Type 2) without size constraints generate a more stable vortex structure to generate the same thrust, resulting in high efficiency.

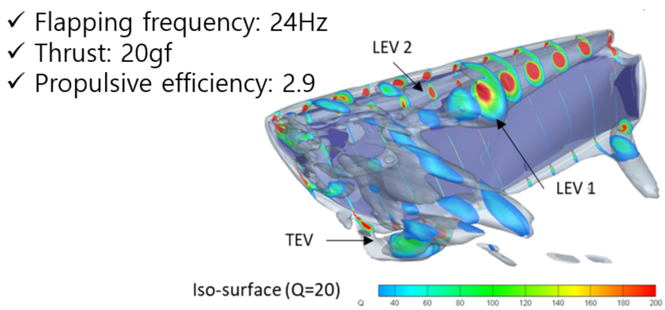


(a) Thrust variation over time.

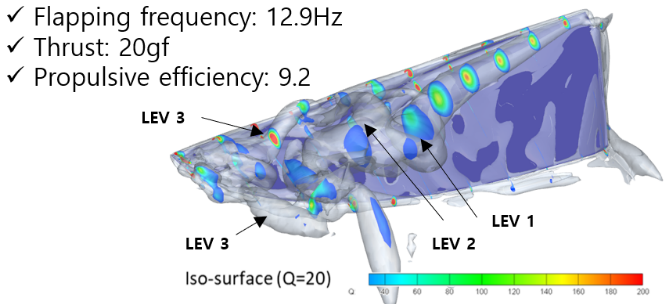


(b) Side force variation over time.

Figure B.2: Comparison of aerodynamic performance.

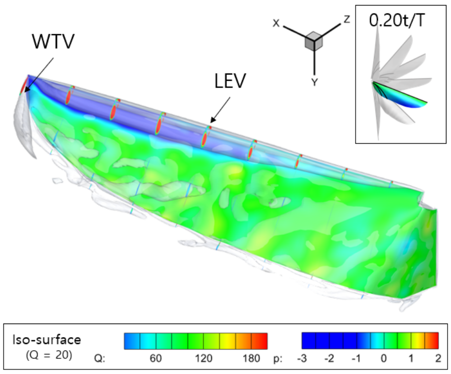


(a) Type 1 at $0.2t/T$.

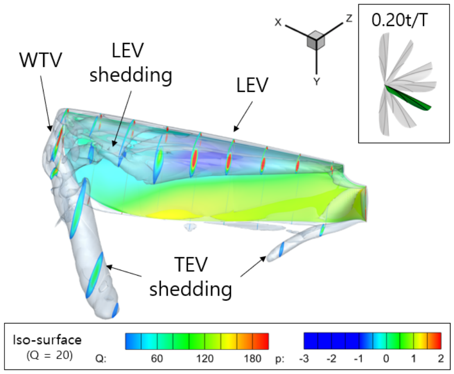


(b) Type 2 at $0.2t/T$.

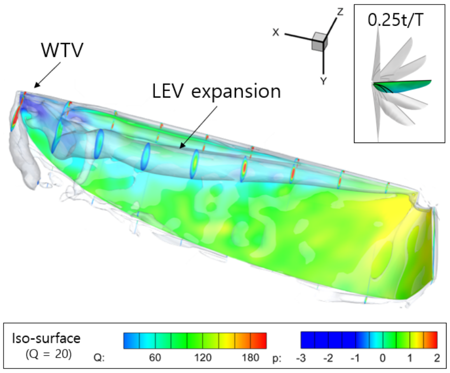


(c) Type 1 at $0.25t/T$.

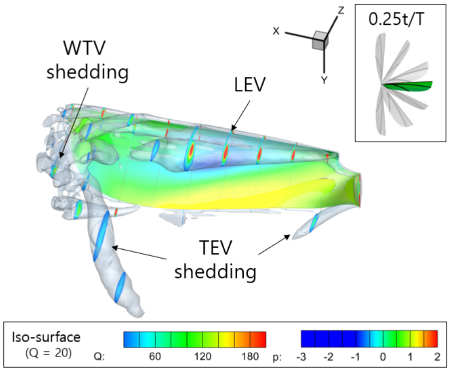


(d) Type 2 at $0.25t/T$.

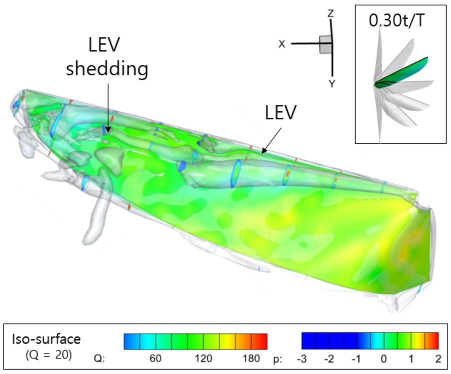


(e) Type 1 at $0.3t/T$.

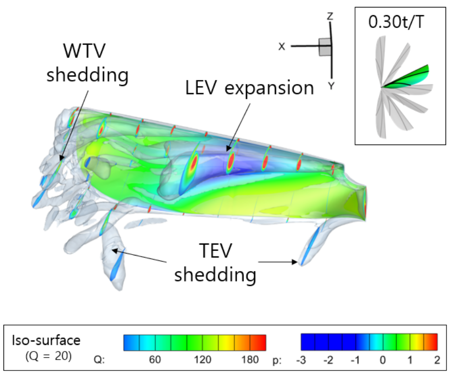


(f) Type 2 at $0.3t/T$.

Figure B.3: Comparison of vortex structures between optimal and baseline wings

# Bibliography


[1] M. Ramasamy, T. E. Lee, and J. G. Leishman, "Flowfield of a rotating-wing micro air vehicle," vol. 44, pp. 1236–1244, American Institute of Aeronautics and Astronautics Inc., 2007.

[2] C. Badrya, B. Govindarajan, J. D. Baeder, A. Harrington, and C. M. Kroninger, "Computational and experimental investigation of a flapping-wing micro air vehicle in hover," *Journal of Aircraft*, vol. 56, pp. 1610–1625, 2019.

[3] V. M. Mwongera, "A review of flapping wing mav modelling," *Int J Aeronautics Aerospace Res*, vol. 2, pp. 27–36, 2015.

[4] D. D. Chin and D. Lentink, "Flapping wing aerodynamics: From insects to vertebrates," 4 2016.

[5] M. K. Salcedo, J. Hoffmann, S. Donoughe, and L. Mahadevan, "Computational analysis of size, shape and structure of insect wings," *Biology Open*, vol. 8, 2019.

[6] F. Zhang, W. Du, and H. Zhang, "A novel bionic-based substructure division method for topology optimization," *Structures*, vol. 29, pp. 937–946, 2 2021.

[7] P. Wu, "Experimental characterization, design, analysis and optimization of flexible flapping wings for micro air vehicles," 2010.

[8] H. Cho, "Development of co-rotational finite elements and application for fluid-structure interaction in biomimetic flexible wing," 2016.

[9] C. Kassiotis, A. Ibrahimbegovic, R. Niekamp, and H. G. Matthies, "Nonlinear fluid-structure interaction problem. part i: Implicit partitioned algorithm, nonlinear stability proof and validation examples," *Computational Mechanics*, vol. 47, pp. 305–323, 2011.

[10] X. Jiao and M. T. Heath, "Common-refinement-based data transfer between non-matching meshes in multiphysics simulations," *International Journal for Numerical Methods in Engineering*, vol. 61, pp. 2402–2427, 12 2004.

[11] H. Jeong, "Two-dimensional fluid-structure interaction of flapping micro aerial vehicles," 2016. 학위논문 (석사)– 서울대학교 대학원 : College of Engineering, Department of Mechanical and Aerospace Engineering, 2018. 8. Chongam Kim.

[12] V. K. Lakshminarayan and C. Farhat, "Nonlinear aeroelastic analysis of highly flexible flapping wings using an ale formulation of embedded boundary method," American Institute of Aeronautics and Astronautics Inc., 2014.

[13] A. Gogulapati, P. P. Friedmann, E. Kheng, and W. Shyy, "Approximate aeroelastic modeling of flapping wings in hover," *AIAA Journal*, vol. 51, pp. 567–583, 3 2013.

[14] J. H. Lee, "Design optimization of wing and non-circular gear based flapping mechanism for biomimetic micro air vehicle," 2021.

[15] C. P. Ellington, "The novel aerodynamics of insect flight applications to micro-air," *The Journal of Experimental Biology*, vol. 202, pp. 3439–3448, 1999.

[16] W. Shyy, M. Berg, and D. Ljungqvist, "Flapping and flexible wings for biological and micro air vehicles," *Progress in Aerospace Sciences*, vol. 35, pp. 455–505, 1999.

[17] C. P. Ellington, C. van den Berg, A. P. Willmott, and A. L. R. Thomas, "Leading-edge vortices in insect flight," *Nature*, vol. 384, pp. 626–630, 1996.

[18] M. H. Dickinson, F.-O. Lehmann, and S. P. Sane, "Wing rotation and the aerodynamic basis of insect flight," *Science*, vol. 284, pp. 1954 LP – 1960, 6 1999.

[19] H. Nagai and K. Isogai, "Effects of flapping wing kinematics on hovering and forward flight aerodynamics," *AIAA Journal*, vol. 49, pp. 1750–1762, 8 2011.

[20] H. Liu and K. Kawachi, "A numerical study of insect flight," 1998.

[21] M. Sun and X. Yu, "Aerodynamic force generation in hovering flight in a tiny insect," *AIAA Journal*, vol. 44, pp. 1532–1540, 7 2006.

[22] R. Ramamurti and W. C. Sandberg, "A three-dimensional computational study of the aerodynamic mechanisms ofinsect flight," *The Journal of Experimental Biology*, vol. 205, pp. 1507–1518, 2002.

[23] J. S. Lee, C. Kim, and K. H. Kim, “Design of flapping airfoil for optimal aerodynamic performance in low-reynolds number flows,” *AIAA Journal*, vol. 44, pp. 1960–1972, 2006.

[24] J. S. Lee, J. H. Kim, and C. Kim, “Numerical study on the unsteady-force-generation mechanism of insect flapping motion,” vol. 46, pp. 1835–1848, 7 2008.

[25] J. H. Kim and C. Kim, “Computational investigation of three-dimensional unsteady flowfield characteristics around insects' flapping flight,” vol. 49, pp. 953–968, 5 2011.

[26] T. Swanson and K. M. Isaac, “Planform and camber effects on the aerodynamics of low-reynolds-number wings,” *Journal of Aircraft*, vol. 47, pp. 613–621, 2010.

[27] R. J. Bomphrey, T. Nakata, N. Phillips, and S. M. Walker, “Smart wing rotation and trailing-edge vortices enable high frequency mosquito flight,” *Nature*, vol. 544, pp. 92–95, 4 2017.

[28] S. Heathcote, Z. Wang, and I. Gursul, “Effect of spanwise flexibility on flapping wing propulsion,” *Journal of Fluids and Structures*, vol. 24, pp. 183–199, 2 2008.

[29] J. Pederzani and H. Haj-Hariri, “Numerical analysis of heaving flexible airfoils in a viscous flow,” *AIAA Journal*, vol. 44, pp. 2773–2779, 11 2006.

[30] M. Olivier, G. Dumas, and J. F. Morissette, “A fluid-structure interaction solver for nano-air-vehicle flapping wings,” 2009.

[31] K. B. Lee, J. H. Kim, and C. Kim, "Aerodynamic effects of structural flexibility in two-dimensional insect flapping flight," *Journal of Aircraft*, vol. 48, pp. 894–909, 2011.

[32] W. Shyy, H. Aono, S. K. Chimakurthi, P. Trizila, C.-K. Kang, C. E. S. Cesnik, and H. Liu, "Recent progress in flapping wing aerodynamics and aeroelasticity," *Progress in Aerospace Sciences*, vol. 46, pp. 284–327, 2010.

[33] W. B. Tay, B. W. van Oudheusden, and H. Bijl, "Numerical simulation of a flapping four-wing micro-aerial vehicle," *Journal of Fluids and Structures*, vol. 55, pp. 237–261, 5 2015.

[34] C. K. Kang, H. Aono, C. E. Cesnik, and W. Shyy, "Effects of flexibility on the aerodynamic performance of flapping wings," *Journal of Fluid Mechanics*, vol. 689, pp. 32–74, 12 2011.

[35] T. Nakata and H. Liu, "A fluid-structure interaction model of insect flight with flexible wings," *Journal of Computational Physics*, vol. 231, pp. 1822–1847, 2012.

[36] A. T. Nguyen and J. H. Han, "Wing flexibility effects on the flight performance of an insect-like flapping-wing micro-air vehicle," *Aerospace Science and Technology*, vol. 79, pp. 468–481, 8 2018.

[37] H. Cho, H. S. Joo, S. J. Shin, and H. Kim, "Elastoplastic and contact analysis based on consistent dynamic formulation of co-rotational planar elements," *International Journal of Solids and Structures*, vol. 121, pp. 103–116, 8 2017.

[38] H. Cho, H. Kim, and S. J. Shin, "Geometrically nonlinear dynamic formulation for three-dimensional co-rotational solid elements," *Computer Methods in Applied Mechanics and Engineering*, vol. 328, pp. 301–320, 1 2018.

[39] C. Farhat and V. K. Lakshminarayan, "An ale formulation of embedded boundary methods for tracking boundary layers in turbulent fluid-structure interaction problems," *Journal of Computational Physics*, vol. 263, pp. 53–70, 4 2014.

[40] H. Cho, D. H. Gong, N. Lee, S. J. Shin, and S. Lee, "Combined co-rotational beam/shell elements for fluid–structure interaction analysis of insect-like flapping wing," *Nonlinear Dynamics*, vol. 97, pp. 203–224, 7 2019.

[41] G. Li, Y. Z. Law, and R. K. Jaiman, "A novel 3d variational aeroelastic framework for flexible multibody dynamics: Application to bat-like flapping dynamics," *Computers and Fluids*, vol. 180, pp. 96–116, 2 2019.

[42] G. C. D. Croon, M. A. Groen, C. D. Wagter, B. Remes, R. Ruijsink, and B. W. V. Oudheusden, "Design, aerodynamics and autonomy of the delfly," *Bioinspiration and Biomimetics*, vol. 7, 6 2012.

[43] K. Y. Ma, P. Chirarattananon, S. B. Fuller, and R. J. Wood, "Controlled flight of a biologically inspired, insect-scale robot," *Science*, vol. 340, pp. 599–603, 2013.

[44] C. Zhang and C. Rossi, "A review of compliant transmission mechanisms for bio-inspired flapping-wing micro air vehicles," 2 2017.

[45] M. Benedict and I. Chopra, "Design, development and flight-testing of a robotic hummingbird," 2015.

[46] H. V. Phan, T. Kang, and H. C. Park, "Design and stable flight of a 21 g insect-like tailless flapping wing micro air vehicle with angular rates feedback control," *Bioinspiration and Biomimetics*, vol. 12, 4 2017.

[47] A. Roshanbin, H. Altartouri, M. Karásek, and A. Preumont, "Colibri: A hovering flapping twin-wing robot," *International Journal of Micro Air Vehicles*, vol. 9, pp. 270–282, 12 2017.

[48] M. W. Simon, L. R. T. Adrian, and G. K. Taylor, "Deformable wing kinematics in the desert locust: how and why do camber, twist and topography vary through the stroke?," *Journal of The Royal Society Interface*, vol. 6, pp. 735–747, 9 2009. doi: 10.1098/rsif.2008.0435.

[49] M. Keennon, K. Klingebiel, H. Won, and A. Andriukov, "Development of the nano hummingbird: A tailless flapping wing micro air vehicle," 2012.

[50] H. V. Phan, Q. T. Truong, T. K. L. Au, and H. C. Park, "Optimal flapping wing for maximum vertical aerodynamic force in hover: Twisted or flat?," *Bioinspiration and Biomimetics*, vol. 11, 7 2016.

[51] J. Lee, S. H. Yoon, and C. Kim, "Experimental surrogate-based design optimization of wing geometry and structure for flapping wing micro air vehicles," *Aerospace Science and Technology*, vol. 123, 4 2022.

[52] S. Yoon, H. Cho, J. Lee, C. Kim, and S. Shin, "Effect of wing deformation by camber angle on aerodynamic performance of flapping micro air vehicles," pp. 1–21, American Institute of Aeronautics and Astronautics Inc, AIAA, 2019.

[53] J. H. Jeon, H. Cho, Y. Kim, J. H. Lee, D. H. Gong, S. J. Shin, and C. Kim, "Design and analysis of the link mechanism for the flapping wing mav using

flexible multi-body dynamic analysis," *International Journal of Micro Air Vehicles*, vol. 9, pp. 253–269, 12 2017.

[54] J. Lee and C. Kim, "Development of a mechanism for flapping wing micro aerial vehicle," pp. 21–22, 2017.

[55] D. Raj Adhikari, "An experimental optimization of flapping wing geometry in the hover," 2018. 학위논문 (석사)– 서울대학교 대학원 : College of Engineering, Department of Mechanical and Aerospace Engineering, 2018. 8. Chongam Kim.

[56] C. W. Hirt, A. A. Amsden, and J. L. Cook, "An arbitrary lagrangian-eulerian computing method for all flow speeds," *Journal of Computational Physics*, vol. 14, pp. 227–253, 1974.

[57] D. J. Mavriplis and Z. Yang, "Construction of the discrete geometric conservation law for high-order time-accurate simulations on dynamic meshes," *Journal of Computational Physics*, vol. 213, pp. 557–573, 4 2006.

[58] A. J. Chorin, "A numerical method for solving incompressible viscous flow problems," *Journal of Computational Physics*, vol. 135, pp. 118–125, 1997.

[59] A. Belov, L. Martinelli, and A. Jameson, "A new implicit algorithm with multigrid for unsteady incompressible flow calculations," American Institute of Aeronautics and Astronautics Inc, AIAA, 1995.

[60] P. L. Roe, "Approximate riemann solvers, parameter vectors, and difference schemes," 1981.

[61] B. V. Leer, "Towards the ultimate conservative difference scheme. v. a second-order sequel to godunov's method," 1979.

[62] H. T. Ahn and Y. Kallinderis, "Strongly coupled flow/structure interactions with a geometrically conservative ale scheme on general hybrid meshes," *Journal of Computational Physics*, vol. 219, pp. 671–696, 12 2006.

[63] S. Yoon and D. Kwak, "Three-dimensional incompressible navier-stokes solver using lower-upper symmetric-gauss-seidel algorithm," *AIAA Journal*, vol. 29, pp. 874–875, 6 1991. doi: 10.2514/3.10671.

[64] J. Young and J. C. Lai, "Oscillation frequency and amplitude effects on the wake of a plunging airfoil," *AIAA Journal*, vol. 42, pp. 2042–2052, 2004.

[65] H. Cho, J. Y. Kwak, S. J. Shin, S. S. Lee, and N. H. Lee, "Flapping-wing fluid-structural interaction analysis using corotational triangular planar structural element," *Journal of Aircraft*, vol. 53, pp. 2265–2276, 2016.

[66] H. Cho, N. Lee, J. Y. Kwak, S. J. Shin, and S. Lee, "Three-dimensional fluid–structure interaction analysis of a flexible flapping wing under the simultaneous pitching and plunging motion," *Nonlinear Dynamics*, vol. 86, pp. 1951–1966, 11 2016.

[67] C. C. Rankin and F. A. Brogan, "An element independent corotational procedure for the treatment of large rotations," *Journal of Pressure Vessel Technology*, vol. 108, pp. 165–174, 5 1986. 10.1115/1.3264765.

[68] C. A. Felippa and B. Haugen, "A unified formulation of small-strain corotational finite elements: I. theory," *Computer Methods in Applied Mechanics and Engineering*, vol. 194, pp. 2285–2335, 6 2005.

[69] J.-M. Battini and C. Pacoste, "Co-rotational beam elements with warping effects in instability problems," *Computer Methods in Applied Mechanics and Engineering*, vol. 191, pp. 1755–1789, 2002.

[70] C. A. Felippa, "A study of optimal membrane triangles with drilling freedoms," *Computer Methods in Applied Mechanics and Engineering*, vol. 192, pp. 2125–2168, 4 2003.

[71] M. A. Crisfield, *Non-Linear Finite Element Analysis of Solids and Structures.* Wiley, advanced t ed., 2000.

[72] M. Arnold and O. Brüls, "Convergence of the generalized-α scheme for constrained mechanical systems," *Multibody System Dynamics*, vol. 18, pp. 185–202, 9 2007.

[73] A. Kumar, S. Mehta, S. Paul, H. S. Gupta, and R. M. Parmar, "Indigenous development of serdes interface for miniaturization," pp. 1–6, 2012.

[74] H. Cho, N. Lee, S. J. Shin, S. Lee, and S. Kim, "Improved computational approach for 3-d realistic insectlike flapping wing using co-rotational finite elements," American Institute of Aeronautics and Astronautics Inc., 2017.

[75] S. K. Chimakurthi, "A computational aeroelasticity framework for analyzing flapping wings," 2009.

[76] J. Alonso and A. Jameson, "Fully-implicit time-marching aeroelastic solutions," American Institute of Aeronautics and Astronautics (AIAA), 1 1994.

[77] D. Shepard, "A two-dimensional interpolation for irregularly-spaced data function," 1968.

[78] A. Beckert and H. Wendland, "Multivariate interpolation for fluid-structure-interaction problems using radial basis functions statische aeroelastik / strömung-struktur-kopplung / mehrfeld problem / multivariate interpolatio-nen / radiale basis funktionen," 2001.

[79] X. Jiao and M. T. Heath, "Overlaying surface meshes, part ii: Topology preservation and feature matching," *International Journal of Computational Geometry*, vol. 14, pp. 403–419, 2004.

[80] X. Jiao and M. T. Heath, "Overlaying surface meshes, part i: Algorithms," *International Journal of Computational Geometry*, vol. 14, pp. 379–402, 2004.

[81] X. Liu, N. Qin, and H. Xia, "Fast dynamic grid deformation based on delaunay graph mapping," *Journal of Computational Physics*, vol. 211, pp. 405–423, 1 2006.

[82] C. Byun and G. P. Guruswamy, "A parallel, multi-block, moving grid method for aeroelastic applications on full aircraft," pp. 570–580, American Institute of Aeronautics and Astronautics Inc, AIAA, 1998.

[83] J. Young and J. C. Lai, "Mechanisms influencing the efficiency of oscillating airfoil propulsion," *AIAA Journal*, vol. 45, pp. 1695–1702, 7 2007.

[84] S. H. Yoon, H. Cho, J. Lee, C. Kim, and S. J. Shin, "Effects of camber angle on aerodynamic performance of flapping-wing micro air vehicle," *Journal of Fluids and Structures*, vol. 97, 8 2020.

[85] S.-H. Yoon, H. Cho, S.-J. Shin, S. Huh, J. Koo, J. Ryu, and C. Kim, "Effect of the leading edge and vein elasticity on aerodynamic performance of flapping-wing micro air vehicles," *Journal of the Korean Society for Aeronautical and Space Sciences*, vol. 49, pp. 185–195, 3 2021.

[86] T. L. Hedrick, "Software techniques for two- and three-dimensional kinematic measurements of biological and biomimetic systems," *Bioinspiration and Biomimetics*, vol. 3, 9 2008.

# 초록

날갯짓 초소형 비행체는 곤충이나 새와 같은 날갯짓 생명체의 비행 특성을 모방하여 개발되고 있다. 날갯짓 비행은 정지 비행이 가능하면서도 민첩한 비행 특징을 가지고 있기 때문에, 다양한 목적의 차세대 초소형 무인항공기로 활용될 수 있어 주목받고 있다.

날갯짓 초소형 비행체의 유연한 날개는 비행 및 공력 성능을 결정짓는 가장 중요한 요소이다. 따라서, 본 연구에서는, 다양한 재질 및 복합적인 형태로 구성된 비등방성 유연 날개의 물리적인 특성들을 사실적으로 모사하여 정밀하게 분석할 수 있는 유체-구조 연성해석 프레임워크를 개발한다. 또한, 유연 날개의 다양한 공력탄성학 설계 파라미터 분석을 통해, 날갯짓 비행체의 공력 성능을 향상시키기 위한 유연 날개의 설계 방안을 제시한다.

본 연구의 3차원 유체-구조 연성해석 프로그램은 날갯짓 초소형 비행체의 복합적인 형상(캠버 각), 다중 재질(시맥 및 박막 등), 경계 조건 등으로 이루어진 비등방성 유연 날개에 대한 유동현상과 구조현상을 사실적으로 모사할 수 있도록 개발되었다. 이는 유동해석, 구조해석, 연성해석 결합 및 정보 전달 모듈 각각에 대하여 정밀도 및 효율성을 고려하여 비교 및 검증을 통해 개발하였으며, 선행 연구의 비행체 뿐만 아니라 실제 날갯짓 비행체와의 교차 검증을 수행하여 매우 정밀한 해석 정확도(추력, 실험오차: 약 1%)를 갖는 것을 확인하였다. 따라서, 고주파수의 매우 유연한 날갯짓에 대하여 공력탄성학 거동과 주변의 비정상 유동 특성을 매우 사실적이고 정밀하게 해석할 수 있다.

유체-구조 연성해석을 기반으로, 캠버 날개에 대한 수동적인 궤적과 구동 속도의 영향에 따른 공력 발생 메커니즘을 분석하여 추력 및 효율 발생에 유리한 궤적 특징을 제시하였다. 또한, 공력탄성학 설계 파라미터(캠버 각, 작동 주파수, 시맥의 재질 특성, 피벗 거리) 분석을 수행하였으며, 구조 동특성(고유진동수, 모드

함수)과 비정상 유동 특성의 관계를 분석하여 비행체의 추력 및 공력 효율 발생에 유리한 비등방성 유연 날개의 설계 가이드라인을 제시하였다. 본 연구에서 제시된 파라미터 선정 방향을 적용하여, 정지비행 기본 비행 조건에서 설계된 날개에서 공력 성능이 획기적으로 향상된 결과를 도출하였다. 전진비행 조건에서도 크게 향상된 공력 성능의 결과를 확인하였으며, 본 연구의 설계 방향은 향후 다양한 운용 조건에서도 우수한 공력 성능을 도출할 수 있을 것으로 기대된다.

결과적으로, 실험 기반으로 개발되어 온 날갯짓 비행체 개발 절차를 수치해석을 활용한 연구로 확장하여 유연 날개의 성능을 크게 향상시킬 수 있었다. 유체-구조 간 긴밀한 상호작용이 발생하는 다양한 공력탄성학 설계 파라미터들에 대한 유체-구조적인 현상을 분석함으로써, 보다 향상된 성능의 날갯짓 비행체 개발에 기여할 수 있다.

**주요어**: 유체-구조 연성해석, 공력탄성학, 전산유체역학, 날갯짓 초소형 비행체, 생체모방, 캠버 날개, 유연 날개

**학번**: 2014-21890